

PDF_{CHEM}: A new fast method to determine ISM properties and infer environmental parameters using probability distributions

Thomas G. Bisbas^{1,2,3*}, Ewine F. van Dishoeck^{4,5}, Chia-Yu Hu^{6,4}, and Andreas Schruba⁴

¹Research Center for Intelligence Computing Platforms, Zhejiang Laboratory, Hangzhou 311100, China

²I. Physikalisches Institut, Universität zu Köln, Zùlpicher Straße 77, Köln, Germany

³Department of Physics, Aristotle University of Thessaloniki, GR-54124 Thessaloniki, Greece

⁴Max-Planck-Institut für Extraterrestrische Physik, Giessenbachstrasse 1, D-85748 Garching, Germany

⁵Leiden Observatory, Leiden University, P.O. Box 9513, NL-2300 RA Leiden, the Netherlands

⁶Department of Astronomy, University of Florida, Gainesville, FL 32611, USA

Accepted XXX. Received YYY; in original form ZZZ

ABSTRACT

Determining the atomic and molecular content of the interstellar medium (ISM) as a function of environmental parameters is of fundamental importance to understand the star-formation process across the epochs. Although there exist various three-dimensional hydro-chemical codes modelling the ISM at different scales and redshifts, they are computationally expensive and inefficient for studies over a large parameter space. Building on our earlier approach, we present PDF_{CHEM}, a novel algorithm that models the cold ISM at moderate and large scales using functions connecting the quantities of the local (effective, 3D) visual extinction, $A_{V,\text{eff}}$, the observed (2D) visual extinction, $A_{V,\text{obs}}$ and the local number density, n_{H} , with probability density functions (PDF) of $A_{V,\text{obs}}$ on cloud scales typically tens-to-hundreds of pc as an input. For any given $A_{V,\text{obs}}$ -PDF, sampled with thousands of clouds, the algorithm instantly computes the average abundances of the most important species (H I , H_2 , C II , C I , CO , OH , OH^+ , H_2O^+ , CH , HCO^+) and performs radiative transfer calculations to estimate the average emission of the most commonly observed lines ($[\text{C II}]$ 158 μm , both $[\text{C I}]$ fine-structure lines and the first five rotational transitions of ^{12}CO). We examine two $A_{V,\text{obs}}$ -PDFs corresponding to a non star-forming and a star-forming ISM region, under a variety of environmental parameters combinations. These cover FUV intensities in the range of $\chi/\chi_0 = 10^{-1} - 10^3$, cosmic-ray ionization rates in the range of $\zeta_{\text{CR}} = 10^{-17} - 10^{-13} \text{ s}^{-1}$ and metallicities in the range of $Z = 0.1 - 2 Z_{\odot}$. PDF_{CHEM} is fast, easy to use, reproduces the PDR quantities of the time-consuming hydrodynamical models and can be used directly with observed data to understand the evolution of the cold ISM chemistry.

Key words: (ISM:) photodissociation region (PDR) – radiative transfer – methods: numerical

1 INTRODUCTION

Star-formation occurs predominantly in the cold ($T_{\text{gas}} \lesssim 30 \text{ K}$) and dense ($n_{\text{H}} \gtrsim 10^4 \text{ cm}^{-3}$) H_2 -rich gas of the interstellar medium (ISM). To understand its evolution throughout cosmic time, knowledge of the molecular mass content of the ISM in galaxies is needed (see [Tacconi et al. 2020](#), for a review). One of the key issues towards this is to determine the distribution of species in large-scale objects, spanning from many parsec to galactic scales, since this can reveal the state of the ISM as well as its potential fraction that leads to star-formation. In addition, there is evidence that the so-called ‘star formation rate’ (SFR), depends on the environmental parameters controlling the distribution of species and the overall thermal balance of the ISM gas. The SFR is a fundamental parameter describing the cyclic process of global star formation and it is observed to vary across cosmic time (see [Madau & Dickinson 2014](#), for a review). It peaks at a redshift of $z \sim 2.5$ marking the galaxy assembly epoch, when the H_2 mass density also peaks ([Genzel et al. 2010](#); [Garratt et al. 2021](#)). It is

also known to be different within our Galaxy when comparing, for instance, the Galactic Centre with the outermost parts (see [Kennicutt & Evans 2012](#), for a review). The higher the SFR, the more energetic the ISM is considered to be. For example, the unattenuated intensity of the FUV radiation field, χ , is frequently assumed to increase with SFR ([Bialy 2020](#)) and the cosmic-ray ionization rate, ζ_{CR} , is also suggested to increase in a similar fashion (e.g. [Papadopoulos 2010](#); [Gaches, Offner, & Bisbas 2019](#)).

Advanced three-dimensional (magneto-)hydrodynamical codes coupled with chemical networks are becoming a powerful way to simulate the dynamics and chemistry of the ISM mimicking the environmental conditions observed in low- and high-redshift galaxies. The inclusion of ISM chemistry in such codes allows to study the atomic-to-molecular transition as well as the different phases of the carbon cycle, defining the so-called photodissociation regions (‘PDRs’; [Tielens & Hollenbach 1985](#); [Hollenbach & Tielens 1999](#); [Röllig et al. 2007](#); [Wolfire, Vallini, & Chevanne 2022](#)). It also allows the construction of synthetic observations (see [Haworth et al. 2018](#), for a review) providing the means to directly compare the simulated clouds with real data.

* E-mail: tbisbas@zhejianglab.com (TGB)

A frequently adopted time-dependent chemical network that allows on-the-fly calculations of abundances of the most important species was implemented by [Glover et al. \(2010\)](#) who significantly improved earlier attempts of [Nelson & Langer \(1997, 1999\)](#). Following a similar approach, the *KROME* package ([Grassi et al. 2014](#)) was developed offering the possibility to study the chemical evolution on a cosmological scale including early Universe. A growing number of projects are focusing on simulating the evolution of the multiphase ISM at kpc scales using time-dependent chemistry. The ‘SILCC’ project ([Walch et al. 2015](#); [Girichidis et al. 2016a](#); [Seifried et al. 2017, 2020a](#)) models small but vertically elongated regions of a galactic disk focusing on studies related to the cycling process of star-formation under different environmental conditions. Hydrochemical simulations of dwarf galaxies have been performed by [Hu et al. \(2016, 2017\)](#) to study the formation of molecular gas in the low-metallicity ISM. [Richings & Schaye \(2016\)](#) modelled isolated galaxies of $10^9 M_\odot$ in total mass at a resolution of $750 M_\odot$ per particle and examined the emission of CII and CO in non-equilibrium (time-dependent) chemistry and with varying metallicity and UV radiation intensities. The ‘Cloud Factory’ project ([Smith et al. 2020](#)) performs high-resolution galaxy-scale simulations and models the ISM in a typical spiral galaxy at a mass resolution of $0.25 M_\odot$ resolving the dynamics and fragmentation of such scales. Recently, [Hu, Sternberg, & van Dishoeck \(2021\)](#) examined the effect on the ISM of varying the metallicity in a kpc galactic region at 0.2 pc resolution with vertical extension such as in the SILCC project, most notably how the atomic-to-molecular transition as well as the carbon-cycle abundances are affected.

To reduce the amount of computations needed when solving the chemistry on-the-fly, alternative approaches have been attempted. These include a large grid of pre-calculated astrochemical simulations which are then tabulated and used during each hydrodynamical timestep. Although this approach may limit the ability to study properly the chemistry in turbulent regions where the gas mixing timescale is comparable to the chemical time needed to reach chemical equilibrium ([Xie et al. 1995](#)), it may well be used to estimate the average abundances and diagnostics in the large-scale ISM. Such a methodology has been adopted in the works of [Wu et al. \(2017\)](#) and [Li et al. \(2018\)](#) using *PYPDR* and *CLOUDY* ([Ferland et al. 2017](#)) pre-calculated grids to study cloud-cloud collisions and whole galactic-disk ISM, respectively. Recently, [Ploeckinger & Schaye \(2020\)](#) performed a great number of PDR calculations (also using *CLOUDY*) which have been tabulated in publicly available datacubes for usage in hydrodynamical simulations for ISM studies from local to high-redshifts. Such a methodology has been also used in steady-state calculations of large and high-resolution three-dimensional clouds on pc-scales (e.g. [Bisbas et al. 2017b](#)).

Other approaches for estimating the abundances of species as well as the emission of atomic and molecular lines at a post-processed stage have been also considered. In this way, [Offner et al. \(2013\)](#) modelled the distribution of abundances of turbulent star-forming clouds using 3D-PDR ([Bisbas et al. 2012](#)). In a follow-up work and combining these results with *RADMC-3D* ([Dullemond et al. 2012](#)), [Offner et al. \(2014\)](#) studied the ability of the $[C\text{I}] \ ^3P_1 \rightarrow ^3P_0$ fine-structure line to trace H_2 gas as an alternative to $^{12}\text{CO } J = 1-0$. Similarly – albeit on a much larger scale – [Gong et al. \(2018, 2020\)](#) examined the behavior of the CO-to- H_2 conversion factor under different ISM environmental conditions, by post-processing *TIGRESS* simulations ([Kim & Ostriker 2017](#)) and using the [Gong et al. \(2017\)](#) simplified network for calculating the hydrogen and carbon chemistry. Recently, [Bisbas et al. \(2021, hereafter B21\)](#) post-processed two distributions of 14^3 pc^3 in volume, which are sub-structures taken from the [Wu](#)

[et al. \(2017\)](#) MHD simulations. Using 3D-PDR they studied the PDR diagnostics covering both the distribution of chemical abundances as well as the line emission of the most important coolants under ten different ISM environmental conditions. These conditions were covering FUV intensities in the range of $\chi/\chi_0 = 1 - 10^3$, cosmic-ray ionization rates in the range of $\zeta_{\text{CR}} = 10^{-17} - 10^{-14} \text{ s}^{-1}$ and metallicities in the range of $Z = 0.1 - 2Z_\odot$.

On the other hand, the observational archive is constantly enriched with ionic, atomic and multi- J transitions of molecular lines, from local clouds to galaxies in the distant Universe (e.g. [Beuther et al. 2014](#); [Mashian et al. 2015](#); [Herrera-Camus et al. 2018](#); [Bigiel et al. 2020](#); [Henríquez-Brocal et al. 2022](#)). If we are to compare the ability and efficiency of the aforementioned numerical approaches to model the multiphase ISM under various environmental conditions, with the wealth of observational datacubes taken from *Herschel*, *SOFIA*, *ALMA*, *JVLA*, and other space and ground-based telescopes, we will observe a disproportional enrichment of the latter. This is because the high computational demand of simulations does not always allow the study of a large range of various three-dimensional density distributions embedded in different ISM conditions to model a particular object. As a natural consequence, limitations are adopted in which i) the complexity of the density distribution is reduced to one-dimensional uniform-density slab representatives, ii) the chemistry is treated with minimal heating and cooling processes, and iii) the radiative transfer calculations are simplified, lacking of chemistry. Such limitations may lead to degenerate solutions in determining the ISM environmental conditions from observations, all the more since the non-linear nature of chemistry combined with the great number of free parameters defining such an environment (i.e. intensity of FUV radiation, cosmic-ray ionization rate, metallicity, shock heating, X-ray intensity etc.) frames a higher-dimensional problem requiring an in-depth exploration.

The structure of the ISM is observed to be very complex and far from uniform. Revealing its three-dimensional structure is a difficult-to-impossible task. Instead, it is often represented by a characteristic distribution of visual extinctions, the so-called A_V -PDF. The quantity A_V represents the visual extinction which correlates with the total H-nucleus column density, N_H , with a conversion factor that depends on the assumed grain size distribution (e.g. [Weingartner & Draine 2001](#); [Rachford et al. 2009](#)). In this work, the relation $A_V = N_H \cdot 6.3 \times 10^{-22} \text{ mag}$ is used ([Röllig et al. 2007](#)). Such distributions of A_V have been studied in local systems (e.g. [Goodman et al. 2009](#); [Kainulainen et al. 2009](#); [Froebrich & Rowles 2010](#); [Abreu-Vicente et al. 2015](#); [Schneider et al. 2016](#); [Ma et al. 2022](#)), but are difficult to determine in the extragalactic context due to resolution limitations (see, however [Leroy et al. 2016](#); [Sawada, Koda, & Hasegawa 2018](#), for such attempts). They provide an opportunity to use them to mimic the complexity of the ISM structure and calculate their atomic and molecular mass content with much simpler PDR models.

All the above have motivated our earlier efforts discussed in [Bisbas et al. \(2019, hereafter Paper I\)](#) in which a new, fast method for calculating the atomic and molecular content of cold ISM regions has been presented. Contrary to the standard way of using (non-) uniform density distributions as inputs, the new method considers user-specified entire column-density probability distributions (A_V -PDFs) to parametrize the ISM at large scales, linking them with a grid of pre-calculated one-dimensional PDR calculations of uniform-density distributions under different ISM environmental parameters. Here, we continue the above efforts by exploring in more detail the connection of A_V -PDFs with the PDR models and by performing radiative transfer to calculate the emission of cooling lines from

these distributions. In particular, we present PDF_{CHEM}¹, a new fast numerical method that is able to compute the PDR chemistry of large-scale inhomogeneous ISM regions using probability distributions of physical parameters as an input within seconds.

As will be discussed in detail later, PDF_{CHEM} should be treated as an attempt to overcome the high computational cost needed by detailed three-dimensional hydrochemical simulations. As such, it should be considered as a machinery to understand the *trends* in estimating the atomic and molecular gas content of large-scale ISM regions and to constrain the ISM environmental parameters which may be used for further in-depth investigations. The results presented here may vary if different initial conditions in the PDR calculations are used or if PDR simulations using other astrochemical codes are applied, e.g. the KOSMA- τ code (Störzer, Stutzki, & Sternberg 1996; Röllig & Ossenkopf-Okada 2022), the MEUDON code (Le Petit et al. 2006), the CLOUDY code (Ferland et al. 1998) and others. The latter can be further understood given the very non-linear nature of PDR chemistry that occurs (see e.g. the code comparison and benchmarking of Röllig et al. 2007). Limitations and approximations in the present approach include assumptions regarding the structure of the FUV radiation field, the neglect of a diffuse component of radiation, as well as the assumption that the cosmic-ray ionization and the metallicity are everywhere constant for the given A_V -PDF. Section 3.8 is dedicated to stress the importance of the above issues, paving the way for the development of future PDF_{CHEM} versions.

This paper is organized as follows. Section 2 defines the ‘effective’ and ‘observed’ visual extinctions used in this work. Section 3 describes how the PDF_{CHEM} algorithm operates using the aforementioned effective and observed A_V , compares to previous works and full hydro models and discusses the limitations of the method. Section 4 is a preamble to application results and describes the oxygen and carbon chemistry as well as the line ratios used in our application results. Section 5 presents results for two hypothetical A_V -PDFs considered corresponding to a non-star-forming and a star-forming ISM distribution. In Section 6 we discuss the use of PDF_{CHEM} in high-redshift galaxies. We conclude in Section 7.

2 EFFECTIVE AND OBSERVED VISUAL EXTINCTIONS

Consider a three-dimensional cloud consisting of a number of computational cells. Each cell has a total H-nucleus number density of n_H . From each cell there are N_ℓ directions emanating uniformly and distributed over the 4π celestial sphere, along which the local column density (and hence the visual extinction) is calculated. Throughout this work, we distinguish between two different A_V quantities: the ‘effective’ (or ‘shielding’ or ‘local’ or ‘3D’) visual extinction denoted as $A_{V,\text{eff}}$, and the ‘observed’ (or ‘2D’) visual extinction denoted as $A_{V,\text{obs}}$.

The $A_{V,\text{eff}}$ represents the local visual extinction of a computational element consisting of the density distribution (see the left schematic of Fig. 1). Under the assumption that the diffuse FUV component is negligible and that the radiation is always perpendicular to the surface, it is given by the expression (Glover et al. 2010; Offner et al. 2013):

$$A_{V,\text{eff}} = -\frac{1}{\gamma} \ln \left(\frac{1}{N_\ell} \sum_{i=1}^{N_\ell} e^{-\gamma A_{V,i}} \right), \quad (1)$$

where $\gamma = 2.5$ is the dust attenuation factor (Bergin et al. 2004; van

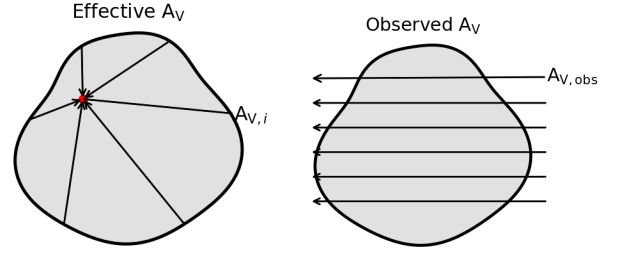


Figure 1. Schematic illustrating the differences between the effective (left) and the observed (right) visual extinctions in a hypothetical cloud. In the left case, the effective A_V is calculated as the average visual extinction of all $A_{V,i}$ that a cell (red dot) locally has (see Eqn. 1) and along which the FUV radiation attenuates. This $A_{V,\text{eff}}$ determines its PDR chemistry. In the right case, the $A_{V,\text{obs}}$ is the visual extinction that a hypothetical observer measures as placed in the right hand side of the cloud.

Dishoeck, Jonkheid, & van Hemert 2006), and $A_{V,i}$ is the visual extinction along each different direction on the celestial sphere centered on the computational element. In the 3D-PDR code (see §3.2), these directions are controlled by the HEALPIX package (Górski et al. 2005) in the ℓ level of refinement. The above value of γ refers to the dust shielding on CO, however our results will not be affected if a different γ factor for H₂ or C is adopted (e.g. a $\gamma = 3.02$ as in Röllig et al. 2007). Along each of the aforementioned $A_{V,i}$ visual extinctions, the FUV radiation field is attenuated as well as the self-shielding of H₂ and CO molecules is computed (see Bisbas et al. 2012, for details). Consequently, the PDR chemistry of the given computational cell giving its abundances of species, gas and dust temperatures as well as level populations of coolants and their corresponding local emissivities, are all connected with this average, effective, visual extinction.

On the other hand, the $A_{V,\text{obs}}$ represents the visual extinction along the line-of-sight of an external observer (see the right schematic of Fig. 1). This is the actual column density that the various observations refer to via extinction mapping out of which the corresponding probability distributions (A_V -PDFs) are constructed. While the line emission is a result of the local PDR chemistry as described above, the optical depth seen by the observer is connected with this, ‘observed’ visual extinction.

Hence, a connection between $A_{V,\text{obs}}$ and $A_{V,\text{eff}}$ is needed to convert the observed column densities to the corresponding effective ones and thus connect them with the local PDR chemistry. In particular, both aforementioned A_V quantities are connected with the total H-nucleus number density. The “ $A_{V,\text{eff}} - n_H$ relation” connects the $A_{V,\text{eff}}$ with the local n_H (see §3.3). The “ $A_{V,\text{obs}} - n_H$ relation” connects the $A_{V,\text{obs}}$ with the average, mass-weighted number density $\langle n_H \rangle$ along the line of sight (see §3.4). In addition, the two A_V quantities are mutually connected via the “ $\langle A_{V,\text{eff}} \rangle - A_{V,\text{obs}}$ relation” where $\langle A_{V,\text{eff}} \rangle$ is, like before, the average mass-weighted effective visual extinction (see §3.5). For simplicity, in this work it is assumed that the total H-nucleus number density, $\langle n_H \rangle \equiv n_H$ and that the effective visual extinction, $\langle A_{V,\text{eff}} \rangle \equiv A_{V,\text{eff}}$. It is noted here that the latter two assumptions do not imply a uniform density slab. Instead, these assumptions connect the $A_{V,\text{eff}}$ with the local n_H as if the spread around the mean is negligible, i.e. a one-to-one correlation. Although the scatter can be large especially for low densities, it is these mean values that our approach adopts. As described below, this correlation leads to a one-dimensional variable density distribution (see Appendix A) covering densities in the range of $n_H = 10^{-1} - 10^6 \text{ cm}^{-3}$. Such a one-dimensional distribution was

¹ <https://github.com/tbisbas/PDFchem>

also constructed by [Hu, Sternberg, & van Dishoeck \(2021\)](#) which reproduced the PDR abundances of their three-dimensional hydrodynamical models.

3 THE PDFCHEM ALGORITHM

3.1 Overview of the method

The PDFCHEM algorithm follows the methodology described in [Paper I](#) in which a set of pre-run PDR thermochemical calculations is used to compute the average abundances of species on cloud scales spanning tens-to-hundreds of pc. This methodology is extended here to compute the average antenna temperatures and to provide estimates for the most commonly used line ratios by solving the radiative transfer equation accordingly. The equation:

$$f_{\text{sp}} = \frac{\sum_{i=1}^q N_i(\text{sp}) \times \text{PDF}(A_{\text{V},i}) \Delta A_{\text{V},i}}{\sum_{i=1}^q N_i(\text{H, tot}) \times \text{PDF}(A_{\text{V},i}) \Delta A_{\text{V},i}} \quad (2)$$

was introduced in [Paper I](#) to calculate the average column-integrated fractional abundance, f_{sp} , of a species ('sp'). In the above, q represents the resolution in which the A_{V} -PDF relation is divided to and N_i is the column density multiplied by the frequency $\text{PDF}(A_{\text{V},i}) \Delta A_{\text{V},i}$. In practice, the required resolution is such that the PDF can be sampled with a few thousand clouds at different $A_{\text{V,obs}}$. Using the above equation, estimates of the average gas temperature are also considered in this work.

Contrary to the use of several uniform-density slabs in [Paper I](#), the PDR database in this work is constructed using a single slab with a density distribution as described below. This distribution is interacting with a large set of ISM environmental parameter combinations (§3.2) building the database of pre-run PDR simulations. The density distribution (hereafter 'variable density slab') is constructed from the empirical $A_{\text{V,eff}} - n_{\text{H}}$ relation (§3.3 and Appendix A). With the above in mind, the following steps take place.

- (i) The user inputs an $A_{\text{V,obs}}$ -PDF distribution representing the observed/simulated object.
- (ii) For each of the given $A_{\text{V,obs}}$ values, PDFCHEM finds the most probable n_{H} number density (§3.4).
- (iii) The above n_{H} corresponds to an effective position, r , in the density distribution of the variable slab and thus to an $A_{\text{V,eff}}$. In turn, the column densities of species and the antenna temperatures of emission lines (radiative transfer) are calculated from the edge of the slab until the effective location r .
- (iv) Steps (ii) and (iii) are repeated for every $A_{\text{V,obs}}$, followed by application of Eqn.(2) to estimate the final weighted-average PDR quantities (abundances of species, line emission and gas temperatures).

The above steps are performed for all different combinations of ISM environmental parameters considered (§3.2). Here, a major assumption is that the overall ISM structure, as presented by the $A_{\text{V,obs}}$ -PDF distribution, is not affected by different parameters (see also §3.8). Eventually, contour-maps are constructed showing the response of the above PDR quantities under the ISM combinations. In this work, these contour-maps examine the atomic-to-molecular transition, the abundances of the carbon cycle and other important species, the average gas temperature and the most frequently used cooling line ratios for all possible pairs of cosmic-ray ionization rate and FUV intensity considered at constant metallicity, Z .

3.2 Photodissociation region chemistry

We use the publicly available code 3D-PDR² ([Bisbas et al. 2012](#)) which treats the astrochemistry of PDRs by balancing various heating and cooling processes as a function of column density. Once the code reaches equilibrium in which the total heating and total cooling are equal to within a user-defined tolerance parameter, it outputs the gas and dust temperature profile, the abundances of species, the level populations of the coolants as well as the various heating and cooling functions versus the column depth. We adopt the modifications and updates presented in [Paper I](#) which include the suprathermal formation of CO via CH^+ ([Federman et al. 1996](#); [Visser et al. 2009](#)).

In this CO formation path, as Alfvénic waves enter the cloud and dissipate as a function of depth, they cause non-thermal motions between ions and neutrals. This effect allows the reaction $\text{C}^+ + \text{H}_2 \rightarrow \text{CH}^+ + \text{H}$ to overcome its energy barrier and thus form CH^+ which in turn reacts with O enhancing the CO abundance ([Federman et al. 1996](#); [Visser et al. 2009](#)). The above reaction increases the CO abundance at low columns of H_2 and is in better agreement with observations ([Rachford et al. 2002](#); [Sheffer et al. 2008](#)). We assume that the above route of CO formation occurs until $A_{\text{V}} = 0.7$ mag from which point onward it ceases to be important. Recently, [Hu, Sternberg, & van Dishoeck \(2021\)](#) found that time-dependency of H_2 formation plays an equally important and independent role with the suprathermal formation route of CO which can also explain the aforementioned observations. Interestingly, [Sun & Du \(2022\)](#) found that in one-dimensional PDR simulations of collapsing clouds that have purely atomic hydrogen as initial chemical composition, the $\text{H} + \text{O} \rightarrow \text{OH}$ reaction is accelerated and CO may form through the OH channel ([Bisbas et al. 2017a](#)). This also increases CO abundances at low column densities where H_2 is not the dominant hydrogen phase. These reactions are included in our network.

As in [Paper I](#), a chemical network of 33 species and 330 reactions is used which is a subset of the UMIST2012 ([McElroy et al. 2013](#)) network. Unless stated otherwise in the tests performed below, Table 1 shows the initial gas-phase elemental abundances of species used here, assuming a gas-to-dust ratio of 100. The column density of dust grains is taken to scale linearly with the metallicity, Z (e.g. [Leroy et al. 2011](#); [Herrera-Camus et al. 2012](#); [Feldmann et al. 2012](#), for values down to $Z = 0.1 Z_{\odot}$), thus the visual extinction, A_{V} , also scales linearly with Z .

A variety of different combinations of ISM environmental parameters between the incident FUV radiation field, χ/χ_0 (normalized to the spectral shape of [Draine 1978](#)), the cosmic-ray ionization rate, ζ_{CR} and the metallicity, Z , is used in this work. In particular, we consider 40 different FUV intensities in the range of $\chi/\chi_0 = 10^{-1} - 10^3$ logarithmically spaced. The FUV intensity is attenuated as a function of depth along the line of sight ([Bisbas et al. 2012](#)). We also consider 40 different cosmic-ray ionization rates in the range of $\zeta_{\text{CR}} = 10^{-17} - 10^{-13} \text{ s}^{-1}$ per H_2 logarithmically spaced. This parameter is kept constant throughout the cloud (c.f. [Gaches, Offner, & Bisbas 2019](#)). These combinations of χ and ζ_{CR} make a grid of 1,600 simulations for a constant metallicity. We also consider four different metallicities ($Z/Z_{\odot} = 0.1, 0.5, 1, 2$), thus making a total of 6,400 PDR simulations. All these simulations use a single density distribution (the variable density slab) resulting from the $A_{\text{V,eff}} - n_{\text{H}}$ relation which covers a density range between $n_{\text{H}} = 10^{-1} - 10^6 \text{ cm}^{-3}$. It is further assumed that the slope of the variable density slab does not change as a function of metallicity (c.f. [Hu, Sternberg, & van](#)

² <https://uclchem.github.io/3dpdr.html>

Table 1. Initial gas-phase abundance of species used for the grid of PDR simulations. The gas-to-dust ratio is assumed to be 100.

Element	Abundance	Reference
H	4.00×10^{-1}	–
H ₂	3.00×10^{-1}	–
He	1.00×10^{-1}	–
C ⁺	1.40×10^{-4}	Cardelli et al. (1996)
O	2.80×10^{-4}	Cartledge et al. (2004)

(Dishoeck 2021). The construction of this slab is discussed below and in Appendix A. The described set of PDR calculations constitutes the pre-run thermochemical database of the algorithm.

3.3 The $A_{V,\text{eff}} - n_{\text{H}}$ relation and the variable density slab

In Paper I, a relation between the $A_{V,\text{eff}}$ and the local number density, n_{H} , was presented which gives the most probable value of the effective visual extinction for a given n_{H} . It results from a collection of four different simulations (from pc to kpc scales, Glover et al. 2010; Van Loo et al. 2013; Safraneck-Shrader et al. 2017; Seifried et al. 2017; Hu, Sternberg, & van Dishoeck 2021). The best-fit equation describing it is

$$A_{V,\text{eff}}(n_{\text{H}}) = 0.05 \exp \left\{ 1.6 \left(\frac{n_{\text{H}}}{[\text{cm}^{-3}]} \right)^{0.12} \right\} [\text{mag}]. \quad (3)$$

The upper panel of Fig. 2 shows Eqn. 3 in black solid line, along with the results from the aforementioned simulations for comparison. In addition, the $A_{V,\text{eff}} - n_{\text{H}}$ relation for the two three-dimensional MHD clouds studied in B21 and post-processed with 3D-PDR, are plotted in blue (the ‘Dense’ cloud) and in orange (the ‘Diffuse’ cloud) solid lines while the corresponding shaded region is the 1σ standard deviation in the B21 models. These two relations are calculated using $N_{\ell} = 12$ HEALPIX rays (Górski et al. 2005) (see Eqn. 1).

Following the $A_{V,\text{eff}} - n_{\text{H}}$ relation described in Eqn. 3, the one-dimensional variable density distribution is constructed which will be used to compute the grid of astrochemical simulations for the various ISM parameters (see Appendix A). Contrary to the standard way of building a grid of uniform density one-dimensional slabs and calculating the astrochemical properties under different ISM environmental parameters (e.g. as described in Paper I), throughout the present work the variable density distribution resulting from the $A_{V,\text{eff}} - n_{\text{H}}$ relation -and only this- will be used.

3.4 The $A_{V,\text{obs}} - \langle n_{\text{H}} \rangle$ relation

While $A_{V,\text{eff}}$ is the local visual extinction in the three-dimensional density distribution, the projected (observed) visual extinction is derived from the column density of the gas that is along the line-of-sight of the observer. We connect this observed visual extinction, $A_{V,\text{obs}}$, with the projected number density which is the average density along the line-of-sight. The latter is calculated from the three-dimensional distributions following the mass-weighted relation

$$\langle n_{\text{H}} \rangle = \frac{\int n_{\text{H}} m_{\text{cell}} dr}{\int m_{\text{cell}} dr}, \quad (4)$$

where m_{cell} is the mass of the computational grid cell.

The middle panel of Fig. 2 shows the $A_{V,\text{obs}} - \langle n_{\text{H}} \rangle$ correlation. Both modeled clouds of B21 are in excellent agreement with each

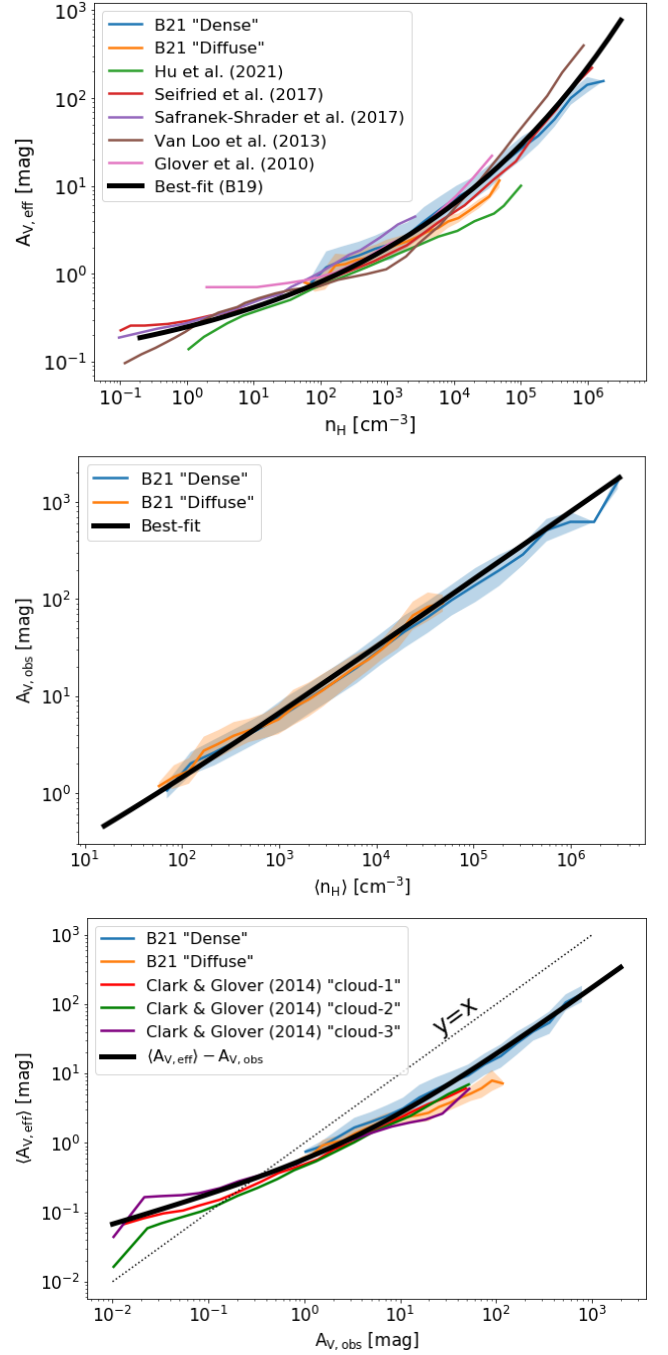


Figure 2. *Top panel:* The $A_{V,\text{eff}} - n_{\text{H}}$ relation for the ‘Dense’ (blue solid line) and ‘Diffuse’ (orange solid line) clouds presented in B21. Results from the studies of Glover et al. (2010); Van Loo et al. (2013); Safraneck-Shrader et al. (2017); Seifried et al. (2017); Hu, Sternberg, & van Dishoeck (2021) are also plotted for comparison. The $A_{V,\text{eff}}$ best-fit in solid black line corresponds to Eqn. 3. *Middle panel:* The $A_{V,\text{obs}} - \langle n_{\text{H}} \rangle$ relation as calculated for the B21 clouds. The black solid line corresponds to Eqn. 5. *Bottom panel:* The $\langle A_{V,\text{eff}} \rangle - A_{V,\text{obs}}$ relation calculated for these clouds in black solid line. The red, green and purple coloured lines correspond to the mean values of three molecular clouds simulated in Clark & Glover (2014). The dotted line in this panel corresponds to the 1-1 relation ($y = x$) to guide the eye. In all panels the shaded regions correspond to 1σ deviation in the B21 simulations.

other albeit that the ‘Dense’ cloud contains densities up to two orders of magnitude higher than the ‘Diffuse’ cloud. The resultant correlation is parametrized with the relation

$$A_{V,\text{obs}} = 0.06 \left(\frac{\langle n_H \rangle}{[\text{cm}^{-3}]} \right)^{0.69} [\text{mag}], \quad (5)$$

and is illustrated in black solid line in the aforementioned panel. Unlike with the $A_{V,\text{eff}}-n_H$ relation, the $A_{V,\text{obs}}-\langle n_H \rangle$ one appears to be a simple power-law, at least to the extent explored in the present work. Following the method for the variable density profile using the $A_{V,\text{eff}}-n_H$ relation, the corresponding one derived from the $A_{V,\text{obs}}-\langle n_H \rangle$ is also obtained (see Appendix A).

3.5 The $\langle A_{V,\text{eff}} \rangle - A_{V,\text{obs}}$ relation

Considering the previous $A_{V,\text{eff}}-n_H$ and $A_{V,\text{obs}}-\langle n_H \rangle$ relationships, the $\langle A_{V,\text{eff}} \rangle - A_{V,\text{obs}}$ can be readily extracted. In particular, the combination of Eqns. 3 and 5 results in:

$$\langle A_{V,\text{eff}} \rangle = 0.05 \exp \left\{ 2.6 \left(\frac{A_{V,\text{obs}}}{[\text{mag}]} \right)^{0.17} \right\}. \quad (6)$$

It is interesting, however, to explore how the latter relation compares with results from hydrodynamical simulations. Such an $\langle A_{V,\text{eff}} \rangle - A_{V,\text{obs}}$ relationship was discussed in Clark & Glover (2014) while studying the star formation rate of three different molecular clouds³. The results of those calculations are illustrated with red, green and purple coloured lines in the bottom panel of Fig. 2, which cover a range of $A_{V,\text{obs}} \sim 10^{-2} - 50$ mag. The black solid line represents Eqn. 6.

To correlate the $A_{V,\text{eff}}$ and $A_{V,\text{obs}}$ from the 3D hydrodynamical clouds of B21, we account for the mass-weighted $A_{V,\text{eff}}$ calculated as

$$\langle A_{V,\text{eff}} \rangle = \frac{\int A_{V,\text{eff}} m_{\text{cell}} dr}{\int m_{\text{cell}} dr}. \quad (7)$$

As with the previous cases, the resulting correlation is illustrated in blue and orange solid lines in the bottom panel of Fig. 2. While both ‘Dense’ and ‘Diffuse’ clouds are more massive and compact from those modeled by Clark & Glover (2014), they cover a range of $A_{V,\text{obs}} \sim 10^0 - 8 \times 10^2$ mag. As can be seen in the bottom panel of Fig. 2, Eqn. 6 is in agreement with both suites of Clark & Glover (2014) and B21 hydrodynamical clouds.

In classical PDR studies, it is frequently assumed that $A_{V,\text{eff}} \equiv A_{V,\text{obs}}$. This case is plotted with dotted lines in the bottom panel of Fig. 2. As can be seen, for $A_{V,\text{obs}} > 1$ mag, the $A_{V,\text{obs}}$ is larger than $A_{V,\text{eff}}$ and the difference becomes substantial, thus a connection of the two visual extinctions, such as Eqn. 6, must be adopted for a proper explanation of the observed clouds.

3.6 Line emission

To calculate the emission of each cooling line as seen by the observer for a given transition $i \rightarrow j$, the equation of radiative transfer

$$\frac{dI_\nu}{dz} = -\alpha_\nu I_\nu + \alpha_\nu S_\nu, \quad (8)$$

must be solved along the line-of-sight of the observer (z -axis). The line emission is calculated using the level populations outputted

by 3D-PDR, after thermal balance has been reached. In a given $A_{V,\text{obs}}$ -PDF, this equation is solved for all $A_{V,\text{obs}}$, following the relations discussed in §3.3-3.5. In the above equation,

$$\alpha_\nu = \frac{c^2 n_i A_{ij}}{8\pi \nu_0^2} \left(\frac{n_j g_i}{n_i g_j} - 1 \right) \phi_\nu, \quad (9)$$

is the absorption coefficient and

$$S_\nu = \frac{2h\nu_0^3}{c^2} \frac{n_i g_j}{n_j g_i - n_i g_j}, \quad (10)$$

is the source function at frequency ν . In the above, A_{ij} is the Einstein A coefficient, n_i and n_j are the level populations, g_i and g_j the corresponding statistical weights and ϕ_ν is the line profile. During the thermal balance iterations, 3D-PDR calculates the level populations of the cooling lines adopting the Large Velocity Gradient (LVG; Sobolev 1960) escape probability approach in which the thermal line width is much smaller than the line width due to the significant line-of-sight velocity change in each direction. Then a photon at frequency ν_{ij} escapes from the modelled cloud without interacting with its surrounding ISM gas with a probability:

$$\beta_{ij} = \frac{1 - e^{-\tau_{ij}}}{\tau_{ij}}, \quad (11)$$

where τ_{ij} is the optical depth for the corresponding frequency.

The line profile, ϕ_ν , for a non-moving gas along the line-of-sight of the observer is given by the expression:

$$\phi_\nu = \frac{1}{\sqrt{2\pi\sigma_\nu^2}}, \quad (12)$$

where σ_ν is the dispersion (which is one half of the Doppler width) defined as

$$\sigma_\nu = \frac{\nu_{ij}}{c} \sqrt{\frac{k_B T_{\text{gas}}}{m_{\text{mol}}} + \frac{v_{\text{turb}}^2}{2}}. \quad (13)$$

In the above, T_{gas} is the local gas temperature, m_{mol} is the molecular weight of the emitting coolant and v_{turb} is the root-mean-square velocity dispersion due to microturbulence, which will be treated as a constant (and taken to be $v_{\text{turb}} = 1 \text{ km s}^{-1}$ unless otherwise stated) in the present work.

The radiative transfer Eqn. (8) is then numerically solved following the methodology of Bisbas et al. (2017b) (see also B21 for an update to include treatment of dust opacity which is also used here). Once solved, the intensity I_ν is converted to the antenna temperature using the relation

$$T_A = \frac{c^2 I_\nu}{2k_B \nu_{ij}^2} [\text{K}], \quad (14)$$

and by multiplying the above quantity with the linewidth, the velocity integrated emission, W [K km s^{-1}], is obtained. Note that the radiative transfer scheme presented above and used in PDFCHEM has been benchmarked against RADEX (van der Tak et al. 2007) with the results presented in Appendix B.

To calculate the average antenna temperature from a given distribution of $A_{V,\text{obs}}$, we apply a modified version of Eqn 2 in the form

$$f(T_A) = \frac{\sum_{i=1}^q T_{A,i} \times \text{PDF}(A_{V,i}) \Delta A_{V,i}}{\sum_{i=1}^q \text{PDF}(A_{V,i}) \Delta A_{V,i}}. \quad (15)$$

Similarly, the average values of optical depths (discussed in Appendices D and E) are calculated.

³ We denote as ‘cloud-1’ the ‘n100_m1250’, as ‘cloud-2’ the ‘n26_m10000’, and as ‘cloud-3’ the ‘n264_m10000’ simulations of Clark & Glover (2014).

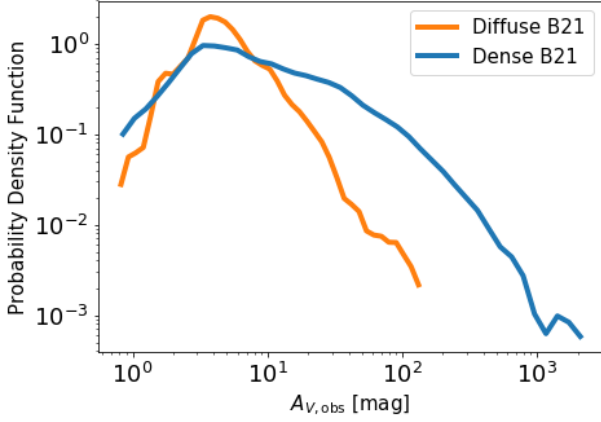


Figure 3. The $A_{V,\text{obs}}$ -PDF relations for the ‘Diffuse’ (orange line) and the ‘Dense’ (blue line) clouds of the 3D MHD simulation by B21.

3.7 Comparison with the B21 hydro models

To benchmark and validate PDF_{CHEM} in using the one-dimensional variable density slab discussed above instead of a large grid of uniform density slabs, we compare it with the results of B21 who studied two different three-dimensional MHD distributions of the same size (14 pc) and post-processed with 3D-PDR.

Figure 3 shows the $A_{V,\text{obs}}$ -PDFs of the two MHD clouds. Both functions peak at ~ 4 mag (mode of the PDF; see Paper I), however the ‘Dense’ PDF has a larger width than the PDF of the ‘Diffuse’ cloud and therefore higher values of $A_{V,\text{obs}}$ are considered. Using these two probability functions, we shall estimate the average values of the abundances of species and ratios of emission lines.

We compare the results for the abundances under different ISM environmental parameters as well as for the radiative transfer calculations, using PDF_{CHEM}. Following the chemistry adopted in B21, we switch off the suprathermal formation of CO via CH^+ for this comparison. We also consider a microturbulent velocity of $v_{\text{turb}} = 2 \text{ km s}^{-1}$.

Figure 4 shows a comparison between the ‘Diffuse’ cloud of B21 (shaded regions representing 1σ standard deviation around the mean) and results obtained using the variable density slab (solid lines). The ISM environmental conditions considered are $\zeta_{\text{CR}} = 10^{-16} \text{ s}^{-1}$, $\chi/\chi_0 = 10$ FUV intensity and $Z = 1 Z_{\odot}$ metallicity, which correspond to the fiducial ISM parameters of B21. The gray region corresponds to the H_I-to-H₂ region which satisfies the abundance difference condition of $|x(\text{H I}) - 2x(\text{H}_2)| < 10^{-3}$. Solid lines correspond to the results of the one-dimensional simulation. We compare the abundances of CII, CI and CO, the gas temperature and the level population number density of the aforementioned species for the ground level as a function of the total number density, n_{H} . The latter two quantities are particularly important for the radiative transfer calculations. As can be seen, in all cases the variable density slab reproduces very well the computationally expensive three-dimensional models. After experimenting, this agreement is true for all ISM environmental parameters explored in B21 ($\zeta_{\text{CR}} = 10^{-17} - 10^{-14} \text{ s}^{-1}$, $\chi/\chi_0 = 1 - 10^3$ and $Z = 0.1 - 2 Z_{\odot}$).

Figure 5 shows the comparison between the abundances of H I, H₂ (top row) and the carbon cycle (bottom row) as calculated from the 3D MHD simulations of B21 versus those calculated using PDF_{CHEM} and after applying it to the entire $A_{V,\text{obs}}$ -PDFs of the two clouds. For the ‘Diffuse’ cloud comparison (left column), we use the cosmic-ray ionization rate as the free parameter while keeping the FUV intensity fixed at $\chi/\chi_0 = 10$ and at solar metallicity. For the ‘Dense’ cloud

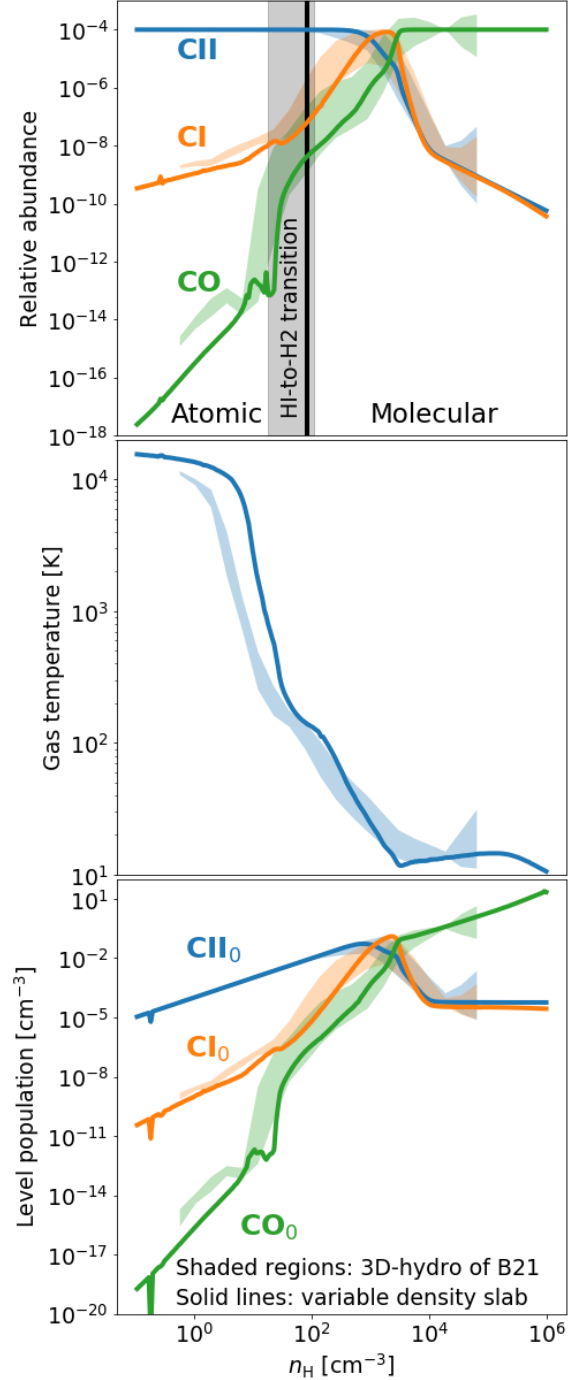


Figure 4. Comparison between a three-dimensional MHD simulation with PDR post-processing (shaded regions representing 1σ standard deviation) and a PDR calculation using the variable density slab (solid lines). The three-dimensional results are taken from B21 (‘Diffuse’ cloud) for ISM conditions corresponding to $\zeta_{\text{CR}} = 10^{-16} \text{ s}^{-1}$, $\chi/\chi_0 = 10$ and $Z = 1 Z_{\odot}$. The top panel compares the abundances of CII (blue), CI (orange) and CO (green) as a function of the local number density, n_{H} . The gray region shows the H_I-to-H₂ transition in the three-dimensional simulation and it corresponds to the condition $|x(\text{H I}) - 2x(\text{H}_2)| < 10^{-3}$, while the black solid line is the aforementioned transition in the one-dimensional simulation. The middle panel shows the gas-temperature as a function of n_{H} . The bottom panel shows the level population number density of CII, CI and CO in the ground level. The agreement is seen to be very good.

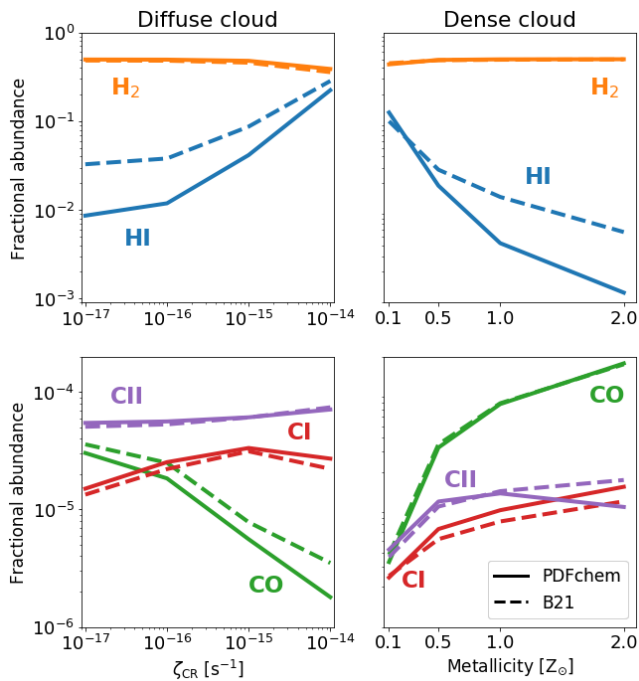


Figure 5. Comparison with B21 MHD simulations. Left column shows the ‘Diffuse cloud’ comparison with the cosmic-ray ionization rate as the free parameter. Right column shows the ‘Dense cloud’ comparison with the metallicity as the free parameter. Top row shows the atomic-to-molecular transition and bottom row the carbon cycle. Solid lines show the results using PDFCHEM and dashed lines those of B21. As can be seen, the results are in a broad agreement.

(right column) we use the metallicity as the free parameter while keeping the cosmic-ray ionization rate fixed at $\zeta_{\text{CR}} = 10^{-16} \text{ s}^{-1}$ and using the aforementioned FUV intensity. As can be seen, we obtain good agreement between PDFCHEM and the 3D MHD simulations. In particular, the ‘Diffuse’ cloud remains always molecular and CII-dominated for any $\zeta_{\text{CR}} = 10^{-17} - 10^{-14} \text{ s}^{-1}$. The ‘Dense’ cloud also remains molecular but CO-dominated for any value of $Z = 0.1 - 2 Z_{\odot}$.

It is interesting also to explore the comparison how PDFCHEM compares with the 3D MHD of B21 runs for the radiative transfer calculations. Figure 6 shows CO spectral line energy distributions (SLEDs) for the ‘Diffuse’ cloud (top row) normalized to the $J = 1-0$ transition and the atomic carbon line ratio ($[\text{C I}](1-0)/[\text{C I}](2-1)$) for the ‘Dense’ cloud (bottom row). From left-to-right, we consider ζ_{CR} , the FUV intensity and the metallicity as the free parameter, respectively. In terms of the trends, we find excellent agreement in all cases and for both clouds. The PDFCHEM and the 3D simulation only differ for higher J -transitions and for enhanced ζ_{CR} values. Such differences may appear in extreme environments due to the sensitive dependence of the high- J CO emission on the local gas temperature and density.

Finally, it is interesting to compare the computational cost between the two approaches. We find that, on top of an already expensive MHD simulation, the demanding three-dimensional density distributions require more than three orders of magnitude longer time to iterate over thermal balance and reach equilibrium, than the corresponding one-dimensional variable density distribution of Appendix A. The small errors between the two approaches and the very high difference in computational time, makes PDFCHEM an attractive new alternative to the complicated three-dimensional simulations for a quick exploration of how the different ISM environmental parameters may

affect the PDR properties of given column density distributions. By assuming different PDF cases, it is also possible to skip the expensive hydrodynamical calculations and understand the behaviour of the atomic and molecular mass content under any combination of ISM environmental parameters.

3.8 Limitations and applicability of PDFCHEM

In order for PDFCHEM to be applicable for the input column density distribution, the assumption that the ISM environmental parameters are *symmetrical compared to the size of the modelled system* must be obeyed. This means that all environmental parameters shall either be treated in a radial manner (e.g. an isotropic FUV radiation field⁴) or assumed to be constant everywhere in the distribution (e.g. cosmic-ray energy densities, metallicity).

Contributions to the diffuse FUV radiation field can arise from scattering of photons due to dust grains which can affect the penetration of FUV along a column (e.g. Flannery, Roberge, & Rybicki 1980; Le Petit et al. 2006; Röllig et al. 2013). In particular, Goicoechea & Le Boulbot (2007) showed that the PDR properties may change even more if a dust growth model along a column is assumed. However, earlier work by van Dishoeck & Dalgarno (1984) showed that the photodissociation lifetime of OH varies by a factor of $\lesssim 2$ for $A_V \gtrsim 1$ mag between a forward scattering model and an isotropic one. For both CI and CO, it is expected that the effect would be smaller since H₂ self-shielding dominates over dust shielding. Although photon scattering is an important FUV component for a more accurate PDR treatment, the presented results are not expected to significantly change.

The diffuse component of radiation field can also arise from internal sources located mainly in the high density medium. For instance, feedback from massive stars such as HII-regions (e.g. Hu et al. 2017; Olivier et al. 2021) and supernova (SN) explosions (e.g. Walch et al. 2015; Hopkins et al. 2018), can significantly affect the distribution of the FUV radiation field and thus alter its isotropic assumption. SNe can further release large amounts of charged particles in the ISM changing its density distribution (Girichidis et al. 2016b) and increasing significantly ζ_{CR} . The latter is supported by observations suggesting an approximately ten percent conversion of the SN explosion energy to cosmic-ray energy (Morlino & Caprioli 2012; Helder et al. 2013). On-going star-formation and in particular cluster formation can also increase locally the FUV radiation field (see reviews by Krumholz, McKee, & Bland-Hawthorn 2019; Rosen et al. 2020). The cosmic-ray ionization rate may also change and largely vary in case protostellar objects are present (Gaches, Offner, & Bisbas 2019). While such effects can co-exist in $A_{V,\text{obs}}$ -PDFs of kpc-scale structures, it is assumed that their contribution to the global ISM environmental parameters is small. To take such local variations into account, one can in principle also adopt an FUV-PDF or a ζ_{CR} -PDF (see also Paper I).

Furthermore, a constant ζ_{CR} with depth into the density distribution has been considered everywhere in this work. However the low-energy component of cosmic-rays, which is responsible for the ignition of chemical reactions at high column densities, do attenuate as a result of Coulomb interactions and ionizations (Padovani, Galli, & Glassgold 2009). A treatment of cosmic-ray attenuation as a function of depth should be accounted for using a more realistic

⁴ Throughout this work, the isotropic radiation field is treated as a radial field without taking into account the contribution from the diffuse component due to scattering.

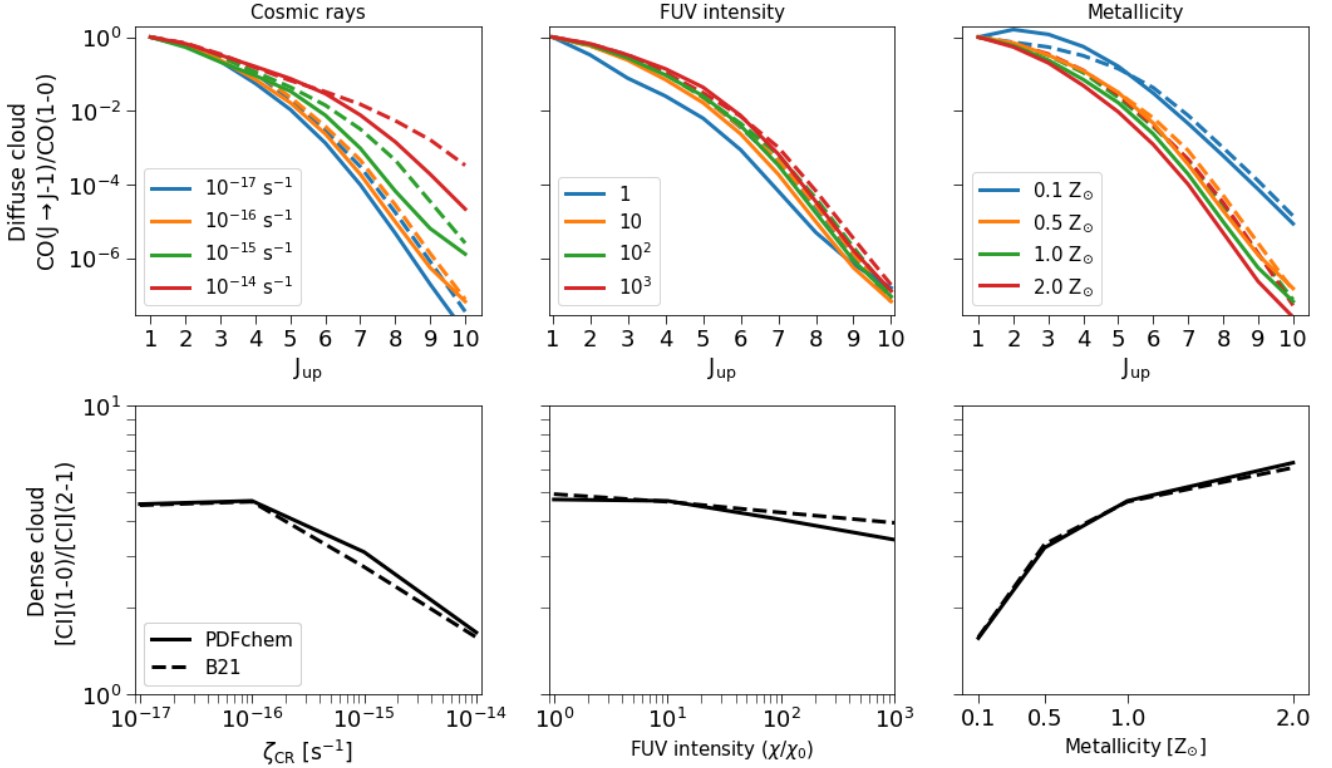


Figure 6. Comparison with the radiative transfer results of the 3D MHD models of B21. Top row shows the CO SLEDs for the ‘Diffuse’ cloud, normalized to the $J = 1-0$ transition. Bottom row shows the emission ratio for the atomic carbon lines ($[C\text{I}](1-0)/[C\text{I}](2-1)$). Columns from left to right show the results for each different free parameter considered (cosmic-ray ionization rate, FUV intensity, metallicity). Solid lines show results using PDFCHEM and dashed lines the B21 results. As can be seen, we achieve very good agreement with the 3D results which dramatically decreases the computational cost in examining PDRs of complex structures.

approach. It is noted, however, that recent three-dimensional simulations of Milky-Way clouds by Gaches, Bisbas, & Bialy (2022) indicate that the constant ζ_{CR} assumption may introduce only small relative errors to the global results for PDR tracers as opposed to a cosmic ray attenuated model. Similarly, a constant metallicity as well as a constant dust-to-gas ratio (which is linearly related to Z) has been considered in this work. In general, this assumption holds well for regions with extents up to kpc-scales, although metallicity gradients showing a decrease of Z as a function of the galactocentric radius have been observed (e.g. Wolfire et al. 2003).

The chemistry in all PDR simulations has been evolved up to a chemical time of 10 Myr, at which point 3D-PDR assumes that equilibrium has been reached (Bisbas et al. 2012). This is a reasonable time duration for the species we examine (see Holdship & Viti 2022, for a discussion). However, time-dependency plays an important role in the H_2 formation particularly at low metallicities, as shown in hydrodynamical simulations by Hu, Sternberg, & van Dishoeck (2021). The steady-state assumption we adopt in this work may overestimate the H_2 abundance at low metallicities and in column-density distributions corresponding to a diffuse ISM region.

In addition, we have assumed that the $A_{\text{V,eff}} - n_{\text{H}}$ relation -and thus the distribution of the variable density slab- remain the same under all ISM environmental parameters explored and that the spread in $A_{\text{V,eff}}$ values for a constant n_{H} is negligible. The hydrodynamical models of Hu, Sternberg, & van Dishoeck (2021) show that the effective column density may have a slightly different dependence on n_{H} for different metallicities. This in turn will impact the PDR chemistry and thus the final results. Thus for a more accurate modelling, a

function relating the input $A_{\text{V,eff}} - n_{\text{H}}$ dependence with the various combinations of ISM environmental parameters need to be taken into account (see also Ploeckinger & Schaye 2020).

Finally, X-rays and shocks have not been considered in our PDR calculations. X-rays can affect the chemistry at high column densities through the production of secondary electrons (similarly to the way cosmic-rays do) which have kinetic energies high enough to cause ionizations of molecules and atoms (Maloney, Hollenbach, & Tielens 1996; Meijerink & Spaans 2005; Meijerink, Spaans, & Israel 2007; Mackey et al. 2019). Shocks can also provide copious amounts of energy in the gas, which can in turn activate reactions with high energy barriers (Meijerink et al. 2011; James et al. 2020) such as the production of OH through the reaction of O and H_2 . Shocks are present in cloud-cloud collisions, in protostellar outflows, but also in galactic scale outflows. However, each of the aforementioned free parameters adds more complexity in the presented algorithm and dramatically increases the total number of PDR simulations needed for this treatment. Shocks do not dominate the ISM emission on large scales, except in case of mergers and AGN outflows (e.g. Meijerink et al. 2013; Bellocchi et al. 2020). Further developments of our algorithm may relax these constraints and allow to explore the trends as a function of these additional ISM parameters.

4 CHEMISTRY RESULTS: BACKGROUND

Before proceeding with presenting the results of our applications in the next Section (§5), it is sensible to provide a short introduction

to the chemical abundances and the line ratios that will be explored. In particular, for each of the $A_{V,obs}$ -PDFs considered, the response of the atomic-to-molecular transition, the abundances of the carbon cycle (discussed in Section 2 of [Paper I](#)), the abundances of OH, OH⁺, H₂O⁺, CH, HCO⁺ and the average (density-weighted) gas temperature will be studied under different combinations of ISM environmental parameters. By performing radiative transfer, the response of the most frequently used line ratios of the carbon cycle will be also studied. These include the atomic carbon line ratio ([C I](2-1)/[C I](1-0)), the first five rotational transitions of CO normalized to CO(1-0), and the line ratios of [C I](2-1)/CO(7-6), [C I](1-0)/CO(4-3), [C I](1-0)/CO(1-0), [C II]/[C I](1-0) and [C II]/CO(1-0).

4.1 Oxygen and carbon chemistry

The molecule of OH can be formed through the reaction of O with H₂ or through the reaction of H₂O⁺ with H₂ followed by dissociative recombination with electrons of the produced H₃O⁺ ([Bialy & Sternberg 2015](#)). It can be also formed via the destruction of H₂O molecule with He⁺ or H⁺ as reactants, both sensitive to the ζ_{CR} rate ([Meijerink et al. 2011](#); [Bisbas, Papadopoulos, & Viti 2015](#)). The latter routes are favoured in low-temperature regions. OH is an important molecule for the study of the ISM, as in regions permeated by high ζ_{CR} values it can lead to the formation of CO ([Bisbas et al. 2017b](#)). Its line emission has been also suggested to trace the “CO-dark” ([van Dishoeck 1992](#)) molecular gas ([Allen, Hogg, & Engelke 2015](#); [Li et al. 2018](#); [Tang et al. 2021](#)).

Cosmic-rays initiate the production of H₃⁺ which in turn reacts with O forming OH⁺. This formation route of OH⁺ via proton transfer is mostly met in molecular regions where the gas temperature is low and the abundance of H₂ is high enough. In addition, cosmic rays reacting with H followed by the reaction with O enable the formation of O⁺. H abstraction of the latter via its reaction with H₂ results in OH⁺ ([Hollenbach et al. 2012](#); [Bialy & Sternberg 2015](#); [Bialy et al. 2019](#)). At low column densities, OH⁺ may also be formed via photoionization of OH, as well as through the reaction H⁺+OH→OH⁺+H ([Meijerink et al. 2011](#)). The abundance and thus the line emission of OH⁺ is known to be very sensitive to the value of cosmic-ray ionization rate and it is thus frequently used to constrain ζ_{CR} ([Hollenbach et al. 2012](#); [Indriolo et al. 2015](#)). The chemistry of H₂O⁺ follows tightly that of OH and OH⁺ species. H₂O⁺ depends sensitively on the ζ_{CR} value and it is also used as a tracer to constrain it ([Hollenbach et al. 2012](#); [Indriolo et al. 2015](#); [Gerin, Neufeld, & Goicoechea 2016](#); [Neufeld & Wolfire 2017](#)).

The CH molecule has different formation routes depending on the density of the gas ([Black & Dalgarno 1973](#)). At low gas densities and thus low visual extinctions, CH is formed via dissociative recombination of CH₂⁺, with the latter produced by radiative association of C⁺+H₂ (e.g. [Gredel, van Dishoeck, & Black 1993](#)). CH₂⁺ then reacts with H₂ to produce CH₃⁺. Both CH₂⁺ and CH₃⁺ products can lead to the formation of CH via dissociative recombination. At higher gas densities and thus higher visual extinctions the reaction of CH₂ with H produces CH and H₂. The observational work of [Sheffer et al. \(2008\)](#) indicates that CH traces the H₂ that exists in the diffuse ISM. In the first extragalactic observational study of CH, [Rangwala et al. \(2014\)](#) have used the CH/CO ratio to infer to the presence of X-rays in NGC 1068, and it is therefore an interesting molecule to study.

The HCO⁺ ion forms through the reaction of H₃⁺ with CO. For this reaction to occur, the gas needs to be UV shielded -so for CO to form- and cosmic-rays must be present to ignite the formation paths leading to H₃⁺. On the other hand, the destruction of HCO⁺ occurs via reactions with H₂O and OH, as well as with recombination

with electrons leading to the formation of CO. HCO⁺ is considered to be a dense gas tracer (e.g. [Knudsen et al. 2007](#); [Zhang et al. 2014](#)). It is also frequently used in tandem with HCN due to the small difference in rest frequencies of their line emission, to infer to the star-formation efficiency, the dense gas properties or the X-ray contribution (e.g. [Shimajiri et al. 2017](#); [Galametz et al. 2020](#); [Wolfire, Vallini, & Chevance 2022](#)).

4.2 Line ratios

Line ratios are frequently used as a diagnostic to infer the molecular gas content and to constrain the ISM environmental parameters. In this work, we focus on the most commonly used ratios between [C II] 158μm, the two [C I] fine-structure lines and the first five CO transitions.

The atomic carbon line ratio ([C I](2-1)/[C I](1-0), with rest frequencies of 809.34 and 492.16 GHz, respectively) is considered to constrain the average gas temperature ([Stutzki et al. 1997](#); [Schneider et al. 2003](#); [Weiß et al. 2003](#); [Papadopoulos, Thi, & Viti 2004](#); [Valentino et al. 2020](#)) and it appears to be generally sub-thermally excited in the extragalactic context ([Papadopoulos, Dunne, & Maddox 2022](#)). It has been used also to construct a distribution function of thermal pressures of ISM gas that best represents the Cold Neutral Medium of our Galaxy ([Jenkins & Tripp 2011](#)). The atomic carbon line ratio is of particular interest for the upcoming CCAT-prime telescope as its available frequency range will favor observations of this line ratio especially in our Galaxy.

The very small (~2.7 GHz) frequency difference of [C I](2-1) and CO(7-6) allows to obtain these two lines simultaneously, thus their ratio is frequently explored, all the more since ALMA is able to capture it at high-redshift. In a similar fashion [C I](1-0) and CO(4-3) can be observed simultaneously with ALMA for high-redshift systems and thus their ratio is also frequently used as a diagnostic of the molecular gas. [C I](1-0) and CO(1-0) are major coolants of the dense star-forming gas. CO(1-0) is known to trace the total molecular mass (see [Bolatto, Wolfire, & Leroy 2013a](#), for a review) while higher- J transitions are useful diagnostics for the warmer molecular gas. [C I](1-0) is also found to be an excellent alternative H₂-gas tracer ([Papadopoulos, Thi, & Viti 2004](#); [Offner et al. 2014](#); [Lo et al. 2014](#); [Bisbas, Papadopoulos, & Viti 2015](#) and [B21](#)).

The spectral line energy distribution of CO is a key diagnostic for the overall ISM properties ([Papadopoulos et al. 2010b](#); [Mashian et al. 2015](#); [Rosenberg et al. 2015](#); [Valentino et al. 2020](#)), including its dynamical state ([Narayanan & Krumholz 2014](#)). Heating processes such as cosmic-rays, X-rays and turbulence can provide strong volumetric heating and thus increase the gas temperature at column densities where the FUV radiation may be severely attenuated. This results in elevated SLEDs ([Bradford et al. 2003](#); [Papadopoulos et al. 2012](#); [Pensabene et al. 2021](#); [Esposito et al. 2022](#)), thus making CO ratios of mid- J /(1-0) and above of particular importance. When combined with the total FIR emission, CO SLEDs can further be used to constrain the contribution of photoelectric heating and thus quantify the above volumetric heating processes ([Harrington et al. 2021](#)). In this paper, we examine CO SLEDs up to $J = 5 - 4$.

Finally, it is interesting to explore the [C II]/CO(1-0) and the [C II]/[C I](1-0) line ratios. In regards to the first one, earlier observations by [Stacey et al. \(1991, 2010\)](#); [Hailey-Dunsheath et al. \(2010\)](#) have found that the [C II]/CO(1-0) ratio is approximately $1 - 4 \times 10^3$ times higher in starburst than in quiescent galaxies. More recent work by [Accurso et al. \(2017b\)](#); [Madden et al. \(2020\)](#) have used that line ratio to infer the CO-dark gas and thus provide a higher estimate of the molecular mass content in galaxies. As we will see below, both

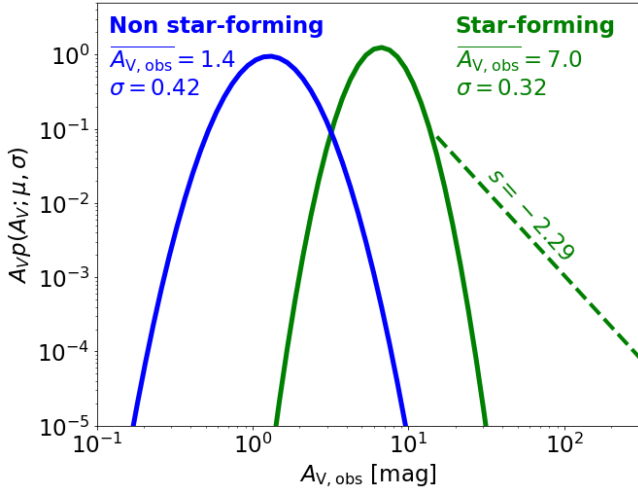


Figure 7. The two $A_{V,\text{obs}}$ -PDFs considered here. The left one (blue solid line) represents a quiescent, non-star-forming distribution. It has a log-normal (LN) distribution with $A_{V,\text{obs}} = 1.4$ mag and $\sigma = 0.42$. The right one (green lines) represents a star-forming distribution. It has a log-normal distribution with $A_{V,\text{obs}} = 7.0$ mag and $\sigma = 0.32$. For $A_{V,\text{obs}} > 14$ mag it has a power-law tail (PL) with slope $s = -2.29$.

$[\text{CII}]/\text{CO}(1-0)$ and $[\text{CII}]/[\text{CI}](1-0)$ ratios show a similar behaviour for the ISM environmental parameters considered in this work, with $[\text{CII}]/[\text{CI}](1-0)$ having a stronger correlation with the FUV intensity than with the cosmic-ray ionization rate (see also Pensabene et al. 2021, for the corresponding ratio with $[\text{CI}](2-1)$).

5 APPLICATIONS

Our approach is applied to two different sets of $A_{V,\text{obs}}$ distributions. These PDFs are illustrated in Fig. 7. The first one (blue colour) corresponds to a quiescent “non-star-forming” column density distribution. It has a simple log-normal (LN) shape peaking at $A_{V,\text{obs}} = 1.4$ mag with $\sigma = 0.42$. The second one (green colour) corresponds to a “star-forming” column density distribution. It contains both an LN shape peaking at $A_{V,\text{obs}} = 7.0$ mag with $\sigma = 0.32$, as well as a power-law tail (PL; green dashed line) with slope $s = -2.29$ for $A_V \gtrsim 14$ mag and up to ~ 500 mag. In a recent study analysing 120 Milky Way clouds, Ma et al. (2022) identified that $\sim 72\%$ of their sample are LN distributions and $\sim 18\%$ LN+PL distributions, while the rest $\sim 10\%$ has an unclear shape. Such PDFs as the aforementioned ones have been frequently observed locally (see Spilker, Kainulainen, & Orkisz 2021, for a such a collection in the Milky Way). For example, the selected $A_{V,\text{obs}}$ -PDF of the non-star-forming region is reminiscent to Lupus-V (Kainulainen et al. 2009) and the one of the star-forming PDF to Cygnus-X (Schneider et al. 2016). In the extragalactic context, PAWS⁵ observations (Hughes et al. 2013) of the CO $J = 1 - 0$ line in the inner $\sim 11 \times 7$ kpc region of M51 found⁶ a lognormal distribution with $A_{V,\text{obs}} \sim 3.25$ mag and $\sigma = 0.44$.

⁵ Plateau de Bure Arcsecond Whirlpool Survey.

⁶ Hughes et al. (2013) convert the CO observations to a Σ_{H_2} using the standard $X_{\text{CO}} = 2 \times 10^{20} \text{ cm}^{-2} \text{ K}^{-1} \text{ km}^{-1} \text{ s}$ conversion factor and a 1.36 helium contribution. We convert Σ_{H_2} to an $A_{V,\text{obs}}$ using the $6.3 \times 10^{-22} \text{ mag cm}^2$ constant and the aforementioned helium contribution.

This extragalactic $A_{V,\text{obs}}$ -PDF lies in-between the above ‘non-star-forming’ and ‘star-forming’ distributions.

5.1 Non star-forming ISM distribution

5.1.1 Abundances, gas temperatures and line ratios

Figure 8 shows the results for the non star-forming ISM distribution for the case of $Z = 1 Z_\odot$ in metallicity. The x-axis of all panels plots the $\log_{10} \zeta_{\text{CR}}$ value, the y-axis the $\log_{10} \chi/\chi_0$ strength of the FUV intensity and all contours are in the \log_{10} space.

Panel (a) plots the $\text{H I}/2\text{H}_2$ abundance ratio and the red solid line corresponds to the H I -to- H_2 transition at which the former ratio is equal to one. The distribution is molecular for any ζ_{CR} and χ/χ_0 pair that lies underneath the red solid line. As can be seen, this $A_{V,\text{obs}}$ -PDF remains molecular for a range of cosmic-rays covering up to moderate ionization rates ($\zeta_{\text{CR}} \lesssim 10^{-15} \text{ s}^{-1}$) and FUV intensities ($\chi/\chi_0 \lesssim 10$). For all other combinations of ζ_{CR} and χ/χ_0 the gas becomes atomic. It is interesting to note that when $\zeta_{\text{CR}} > 10^{-15} \text{ s}^{-1}$, H_2 is destroyed at approximately equal amounts due to the reactions with H_2O^+ and OH^+ (produced by cosmic-rays) as well as by the direct reaction with cosmic-rays producing H_2^+ . The aforementioned reactions dominate even in the absence of FUV radiation and thus the medium at such ζ_{CR} is always atomic. The red solid line is overplotted in all panels of Fig. 8 to guide the eye as to when the medium becomes molecular.

Panels (b-d) show the abundances of the carbon cycle (CII , C I and CO , respectively). For this distribution, the contours of CII and C I appear to be approximately horizontal under all ζ_{CR} values, indicating that they depend primarily on the intensity of FUV radiation. Similarly the abundance of CO , although lower than the abundances of CII and C I at all times, show a dependence on the FUV radiation in conditions appropriate for the existence of molecular gas (underneath the red solid line). In the atomic part, the abundance of CO is -as expected- very low but does show a dependence on ζ_{CR} as we will discuss in more detail in the star-forming ISM case (§5.2).

Panel (e) shows the density-weighted gas temperature. In the molecular region it varies from $20 \lesssim T_{\text{gas}} \lesssim 100 \text{ K}$ whereas otherwise it can reach values as high as $\sim 10^3 \text{ K}$ for $\chi/\chi_0 > 10^2$. The average gas temperature, here, depends primarily on the strength of the FUV radiation rather than on the value of ζ_{CR} .

Panel (f) illustrates the abundance of OH . For conditions favouring the existence of molecular gas, the abundance of OH is $10^{-8} - 10^{-6}$ depending on the ζ_{CR} -FUV intensity combination. In particular, OH peaks for $\chi/\chi_0 \lesssim 1$ and for $10^{-16} \lesssim \zeta_{\text{CR}} \lesssim 10^{-15} \text{ s}^{-1}$. Here, OH forms mainly through dissociative recombination of H_3O^+ . In panels (g) and (h), the abundances of OH^+ and H_2O^+ are illustrated. Their response in varying ζ_{CR} and χ/χ_0 is very similar. Under molecular conditions, they both increase only as a function of ζ_{CR} . Their peak is found to occur for atomic conditions and in particular for $\chi/\chi_0 \sim 30$ and $\zeta_{\text{CR}} \sim 3 \times 10^{-15} \text{ s}^{-1}$. For these values, OH^+ forms via the reaction of H_2 with O^+ , and H_2O^+ forms via the reaction of H_2 with OH^+ .

Panel (i) shows contours for the CH abundance. The abundance of this species increases for low ζ_{CR} and/or χ/χ_0 peaking for molecular conditions and with both cosmic-rays and FUV intensities minimized. Under these conditions CH is found to be the result both of CH_2 reacting with H and through dissociative recombination of CH_3^+ . In panel (j), the abundance of HCO^+ is plotted. The dependence of this species on ζ_{CR} and χ/χ_0 is reminiscent to the CO abundance described above. HCO^+ peaks for moderate values of ζ_{CR} and low FUV intensities and is formed via CO^+ reacting with H_2 .

Non star-forming ISM

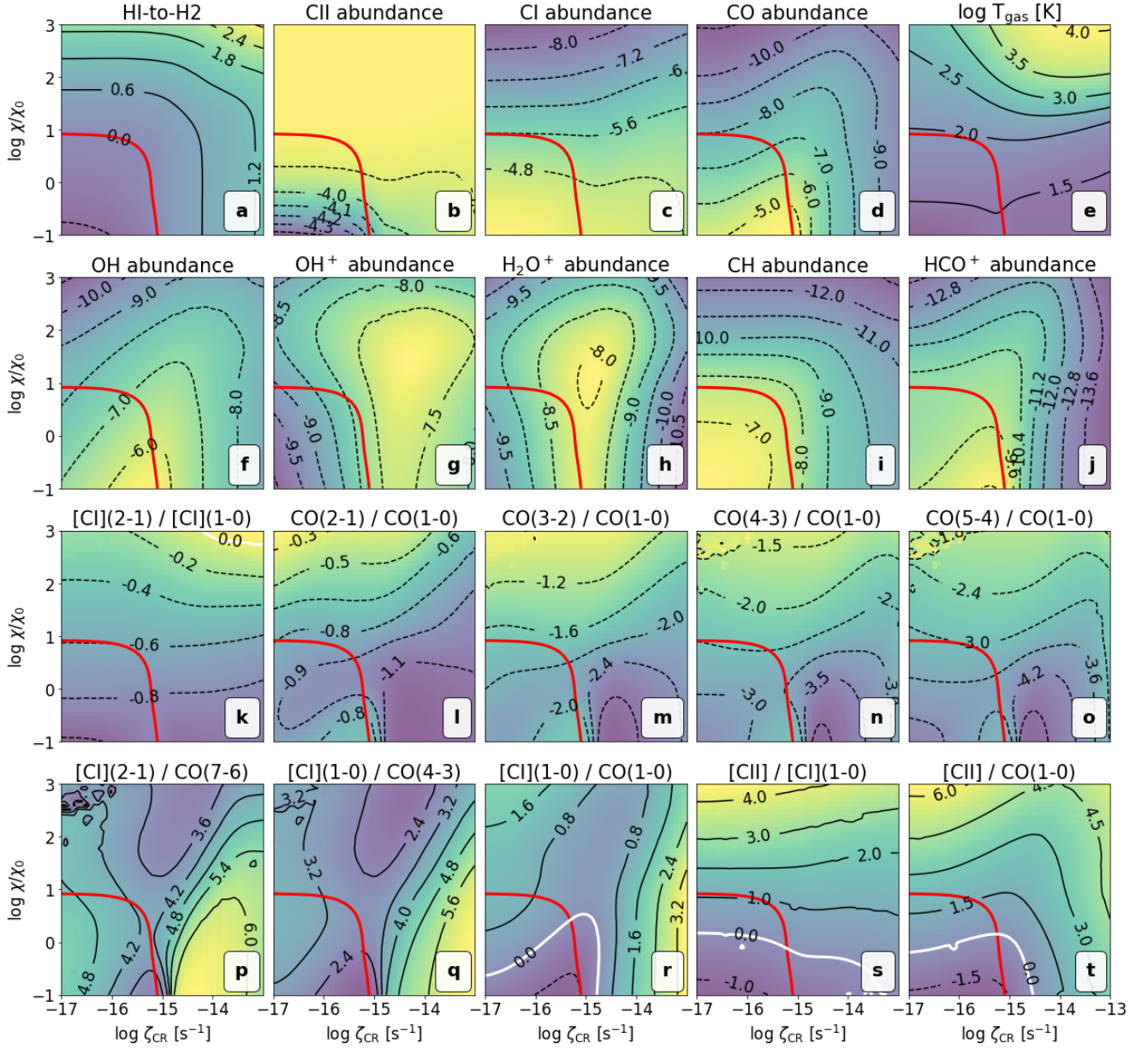


Figure 8. Results for the non-star-forming distribution at $Z = 1 Z_{\odot}$. In all panels, x-axis is the cosmic-ray ionization rate in the range of $\zeta_{\text{CR}} = 10^{-17} - 10^{-13} \text{ s}^{-1}$, and y-axis is the FUV intensity in the range of $\chi/\chi_0 = 10^{-1} - 10^3$. All axes and contours shown are in common logarithmic space (\log_{10}). Top row from left-to-right: the H I-to-H₂ transition where the condition $\text{H I} = 2\text{H}_2$ is marked in red solid line. This line is overplotted in all panels. The gas is molecular for ζ_{CR} and χ/χ_0 pairs smaller than those corresponding to the red line while it is atomic otherwise. The abundances of C II, C I and CO are shown in panels (b-d). Panel (e) shows the response of the average (density-weighted) gas temperature. The second row (left-to-right) shows the abundances of OH, OH⁺, H₂O⁺, CH and HCO⁺. The last two rows show brightness temperature ratios of various emission lines. Whenever shown, the white solid line marks the condition when the brightness temperatures of the two lines in the ratio are equal. Panel (k) shows the line ratio of [C I](2-1)/[C I](1-0). The rest of panels in this row illustrate a two-dimensional SLED normalized to CO $J = 1 - 0$, for $J = 2 - 1$ to $5 - 4$. Bottom row from left-to-right: ratios of [C I](2-1)/CO(7-6), [C I](1-0)/CO(4-3), [C I](1-0)/CO(1-0), [C II]/[C I](1-0) and [C II]/CO(1-0).

The bottom two rows show the results for the line ratios. In particular in panel (k), the atomic carbon line ratio ([C I](2-1)/[C I](1-0)) is plotted. Under all combinations of ζ_{CR} and χ/χ_0 explored, this line ratio depends strongly on the FUV intensity and is nearly independent of the cosmic-ray ionization rate. It can thus be used as a tracer for the value of χ/χ_0 for a column density distribution similar to the non-star-forming case. It appears that when the two environ-

mental parameters explored are maximized, the antenna temperature of [C I](2-1) becomes stronger than [C I](1-0). However, for such extreme conditions the gas is heavily atomic with the carbon to be mainly in the ionized phase; thus the emission of both [C I] lines may not be detectable.

In panels (l-o), a two-dimensional CO SLED is illustrated. Focusing on the ratios for molecular conditions, it can be seen that all

Non star-forming ISM

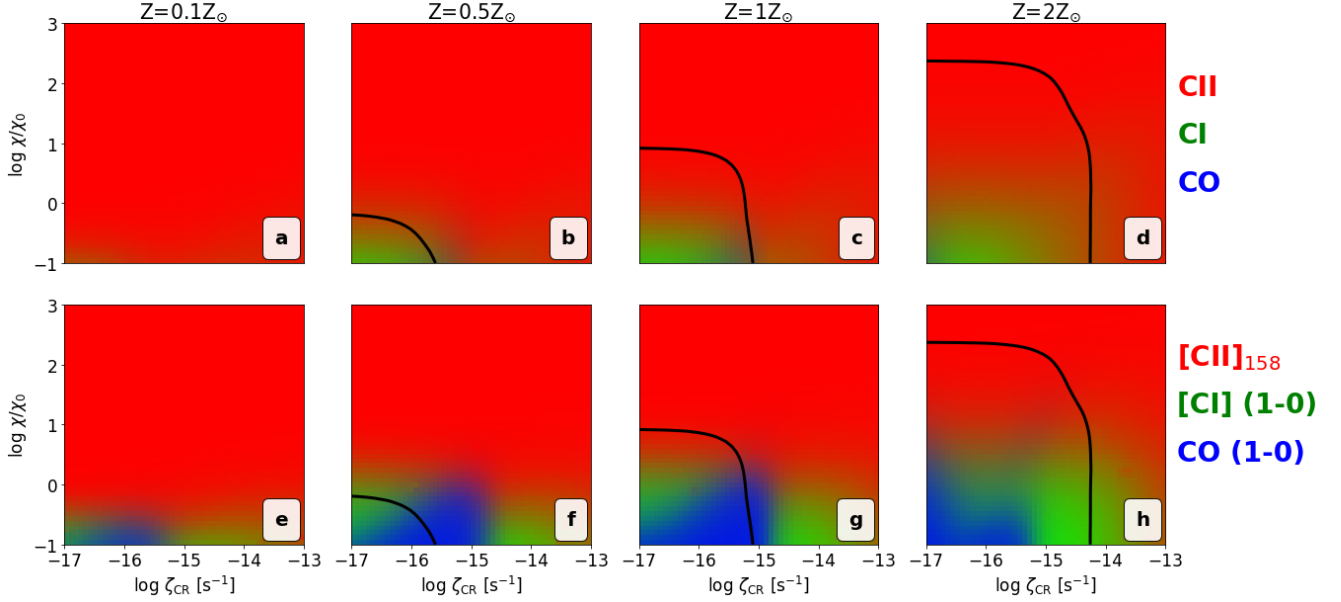


Figure 9. Maps showing which carbon phase dominates for all combinations of the ISM environmental parameters considered. The x -axis is the cosmic-ray ionization rate and the y -axis is the FUV intensity. These maps are calculated for the non-star-forming $A_{V,obs}$ -PDF. The top row shows which carbon phase dominates in terms of the abundance while the bottom row shows the same but in terms of the brightness temperature. The solid black line shows the H I-to-H₂ transition, below which the distribution is molecular, otherwise it becomes atomic. Red colour is for C II and the [C II] 158 μ m line, green colour for the C I abundance and the [C I](1-0) 609 μ m line, and blue colour for the CO abundance and the CO(1-0) line. Each column corresponds to different metallicity ($Z = 0.1, 0.5, 1$ and $2 Z_{\odot}$, from left-to-right). As can be seen, the fact that a particular carbon phase dominates in terms of the abundance, does not always mean that it will also have the brightest emission, since gas temperature and optical depth effects need to be accounted for.

$(J \rightarrow J-1)/(1-0)$ ratios obtain their highest value for low FUV intensities ($\chi/\chi_0 \lesssim 1$) and moderate-to-low cosmic-ray ionization rates ($10^{-16} \lesssim \zeta_{CR} \lesssim 10^{-15} \text{ s}^{-1}$). For these conditions and the particular $A_{V,obs}$ -PDF, the CO abundance obtains its highest value while the average gas temperature is ~ 30 K, leading to an elevated antenna temperature of the mid- J lines when compared to the rest of ISM conditions. This trend can be better seen and understood in the star-forming $A_{V,obs}$ -PDF case which is explained in more detail in §5.2.1.

Finally, in the fourth row, five of the most frequently used ratios are shown. As before, the focus here will be for the conditions leading to molecular gas. Panel (p) shows the [C I](2-1)/CO(7-6) ratio which indicates a much brighter [C I](2-1) antenna temperature than CO(7-6). This ratio is $\sim 6 \times 10^4$ for low ζ_{CR} but decreases to $\sim 4 \times 10^3$ for $\zeta_{CR} \sim 10^{-15} \text{ s}^{-1}$, since cosmic-rays can elevate the gas temperature at high column densities increasing the CO(7-6) line emission. Similarly, the [C I](1-0)/CO(4-3) ratio shown in panel (q), also indicates a $\sim 10^2 - 10^3$ times brighter [C I](1-0) antenna temperature. Such high ratios are estimated because high- J CO are brightly emitted only from the high-end of $A_{V,obs}$ -PDF and are thus overall very weak.

The [C I](1-0)/CO(1-0) ratio shown in panel (r) is of particular interest. The white solid line marks the case when the antenna temperatures of these two emission lines are the same. The dependence of this ratio on the ζ_{CR} and χ/χ_0 parameters is reminiscent to that of the CO abundance. In particular, it is found that the antenna temperature of CO(1-0) is brighter than that of [C I](1-0) for generally low FUV intensities and for $\zeta_{CR} \sim 2 \times 10^{-15} \text{ s}^{-1}$, which surpasses the H I-to-H₂ transition as can be seen (see Appendix C). The [C II]/[C I](1-0) ratio illustrated in panel (s) shows that this non-star-forming distribution is in general bright in [C I](1-0) and becomes brighter in [C II]

when χ/χ_0 increases. This increase in [C II] is expected, since the FUV radiation ionizes carbon to form C II and also increases the gas temperature. Finally, the [C II]/CO(1-0) ratio pattern shown in panel (t) is also reminiscent to the one of CO abundance. As with the [C II]/[C I](1-0) ratio, the [C II] antenna temperature is higher than the CO(1-0) one as χ/χ_0 increases. Interestingly, all three ratios explored for CO(1-0), [C I](1-0) and [C II], have their ratio equal to 1 for $\chi/\chi_0 \sim 1$ regardless to the ζ_{CR} value.

Appendix D discusses the behaviour of the optical depths of [C II], [C I](1-0) and CO(1-0) for the non-star-forming ISM distribution. Figures F1-F3 of Appendix F show the corresponding results of abundances and line ratios for $Z = 0.1, 0.5$ and $2.0 Z_{\odot}$, respectively.

5.1.2 Carbon phases at different metallicities

Figure 9 shows which carbon phase dominates for all the ISM environmental parameters considered in this work. The top row shows the response of the abundances of C II (red), C I (green) and CO (blue) while the bottom row shows their corresponding antenna temperatures ([C II] 158 μ m, [C I](1-0), CO(1-0), respectively). In all panels, the black line shows the H I-to-H₂ transition. Each column corresponds to different metallicities, from $Z = 0.1 Z_{\odot}$ to $2 Z_{\odot}$ (left-to-right).

In regards to the abundances (top row of Fig. 9), for $Z = 0.1 Z_{\odot}$ the gas is purely atomic under all ISM conditions as shown in panel (a). Carbon is mainly found in C II form, since its abundance dominates for all ζ_{CR} -FUV intensity combinations. The non star-forming distribution appears to become molecular only for $Z > 0.5 Z_{\odot}$ (panel b) and for a combination of very low amounts of FUV radiation ($\chi/\chi_0 \lesssim 1$) and low ζ_{CR} ($\lesssim 10^{-16} \text{ s}^{-1}$). As metallicity increases to solar and

super-solar values (panels c-d), the distribution remains molecular for combinations of higher χ/χ_0 and ζ_{CR} . This is because FUV radiation is more strongly attenuated due to the increased dust shielding allowing H_2 molecules to form more efficiently at lower column densities. For all metallicity cases, the distribution never becomes CO-dominated but rather C I-dominated and only for low χ/χ_0 and ζ_{CR} . Otherwise it is always C II-dominated.

The maps of carbon cycle abundances are not always reflected in the corresponding line emission maps as can be seen in the bottom row of Fig. 9. For $Z = 0.1 Z_\odot$ (panel e) it is found that for $\chi/\chi_0 \lesssim 0.3$ and $\zeta_{\text{CR}} \lesssim 2 \times 10^{-16} \text{ s}^{-1}$, the distribution, although atomic, can be bright in CO(1-0) and also [C I](1-0). In particular, as can be seen also for $Z = 0.5$ and $1 Z_\odot$ (panels f-g), the atomic gas can be indeed bright in the aforementioned lines. There are two reasons that explain this feature: i) the $A_{\text{V,obs}}$ -PDF contains high column densities and although they have small probability, they can be bright in CO(1-0) and [C I](1-0) and ii) the suprathermal formation route of CO via CH^+ considered in these runs can increase the abundance of CO at low visual extinctions and thus the corresponding level populations, building a bright CO(1-0) antenna temperature at low A_{V} . The latter effect is further discussed in Appendix C.

It is further found that the molecular distribution can be [C I](1-0) as well as [C II] 158 μm bright (panels g-h). In general, it will become [C II] bright as the FUV intensity increases -and, in this $A_{\text{V,obs}}$ -PDF case- only when metallicities $Z \gtrsim 1 Z_\odot$. In addition, as the χ/χ_0 increases, the CO(1-0) brightness temperature will be followed by [C I](1-0) and then to [C II] 158 μm , although for moderate ζ_{CR} values the [C I](1-0) brightness temperature never dominates (the gas is either CO(1-0) or [C II] bright). For low χ/χ_0 and as ζ_{CR} increases, the aforementioned transition sequence of CO(1-0) to [C I](1-0) to [C II] is also repeated due to the CO destruction.

In panels G1a,c of Appendix G, it is shown how the above results for $Z = 1 Z_\odot$ would differ if a lower $A_{\text{V}}/N_{\text{H}}$ factor was adopted.

5.2 Star-forming ISM distribution

5.2.1 Abundances, gas temperatures and line ratios

Following the description of Fig. 8 for the non-star-forming case, Fig. 10 shows the results for the star-forming ISM distribution at $Z = 1 Z_\odot$. Here, both the lognormal (LN) and power-law (PL) components have been considered. As can be seen in panel (a), this distribution remains largely molecular for all combinations of ζ_{CR} and FUV intensities explored, except for very high cosmic-rays i.e. $\zeta_{\text{CR}} \gtrsim 5 \times 10^{-14} \text{ s}^{-1}$.

The carbon cycle illustrated in panels (b-d), has an interesting behaviour depending on the ζ_{CR} -FUV intensity combination. The C II abundance increases both when the FUV intensity increases as a result of atomic carbon photoionization and when the cosmic-ray ionization rate increases as a result of the destruction of CO by He^+ , peaking for high values of ζ_{CR} and/or χ/χ_0 . For $\chi/\chi_0 > 10$, the abundance of C I decreases and depends almost entirely on the value of FUV intensity. However, for $\chi/\chi_0 < 10$, it increases and peaks for moderate cosmic-rays e.g. $10^{-16} < \zeta_{\text{CR}} < 3 \times 10^{-15} \text{ s}^{-1}$, as a result of the cosmic-ray induced destruction of CO (Bisbas, Papadopoulos, & Viti 2015; Bisbas et al. 2017b). In this effect cosmic-rays create a surplus of He^+ which reacts very effectively with CO creating C II. In moderate ζ_{CR} , C II recombines quickly creating large amounts of C I; hence the C I abundance peak seen in the corresponding panel. At high ζ_{CR} , this recombination is not so effective and thus carbon remains in the form of C II. The aforementioned sequence is also reflected in the CO abundance panel which shows a strong dependence on

ζ_{CR} rather than on χ/χ_0 . During all the above carbon cycle phase changes, the gas remains always molecular.

The average, density-weighted gas temperature illustrated in panel (e), shows a dependence on both ζ_{CR} and χ/χ_0 . Like in the non star-forming distribution, the gas temperature is found to be in the range of $10 \lesssim T_{\text{gas}} \lesssim 60 \text{ K}$. For a constant ζ_{CR} , the gas temperature increases as a result of the increase of photoelectric heating. For a constant χ/χ_0 , the gas temperature increases as result of the increase of cosmic-ray, chemical and H_2 formation heating mechanisms (Bisbas et al. 2017b). The particular chemical heating is a result of contributions by photoelectrons, turbulence dissipation, exothermic reactions due to HCO^+ , H_3^+ and H_3O^+ recombination as well as ion-neutral reactions between H_2^+ and He^+ .

Panel (f) shows the response of OH abundance. For low ζ_{CR} (i.e. $\lesssim 10^{-16} \text{ s}^{-1}$) and high FUV intensities ($\chi/\chi_0 > 10$), the abundance of OH is reduced, whereas for all other cases and especially for high ζ_{CR} or when χ/χ_0 is very low, it is increased, as a result of the H_3O^+ dissociative recombination. Furthermore, as can be seen, the abundance of OH strongly depends on ζ_{CR} particularly when $\zeta_{\text{CR}} \gtrsim 10^{-15} \text{ s}^{-1}$. Similarly, both OH^+ and H_2O^+ species (panels g,h) depend strongly on cosmic-rays and weakly on χ/χ_0 . The abundance of the latter two ions is high for a combination of high ζ_{CR} and high χ/χ_0 . On the other hand the abundance of CH, as seen in panel (i), peaks for low FUV intensities ($\chi/\chi_0 < 1$) and for $\zeta_{\text{CR}} \approx 10^{-16} \text{ s}^{-1}$ as a result of the $\text{CH}_2 + \text{H}$ reaction and CH_3^+ recombination. It is reduced when χ/χ_0 and/or ζ_{CR} increase. In panel (j), the abundance of HCO^+ is illustrated which shows a strong dependence on the value of ζ_{CR} while having a negligible dependence on the value of FUV intensity.

The [C I](2-1)/[C I](1-0) line ratio illustrated in panel (k), indicates that in systems with column density distributions reminiscent to the star-forming ISM modelled here, it may be used to constrain the value of ζ_{CR} . As can be seen, this line ratio depends on ζ_{CR} particularly when $\zeta_{\text{CR}} \gtrsim 10^{-15} \text{ s}^{-1}$, a value that may be met in starburst galaxies and systems with high star-formation rates (Bisbas et al. 2021). For cosmic-rays with $\zeta_{\text{CR}} \lesssim 10^{-15} \text{ s}^{-1}$, this ratio depends almost entirely on χ/χ_0 and thus can be used to constrain the FUV intensity.

The two-dimensional CO SLED shown in panels (l-o), indicate that the $(J \rightarrow J-1)/(1-0)$ CO ratio shows a strong dependence on cosmic-rays for $\zeta_{\text{CR}} \gtrsim 10^{-15} \text{ s}^{-1}$. As described above, this is due to the fact that high cosmic-ray energy densities heat up the gas at high column densities, thus making mid- J and high- J CO transitions very bright (see §4.2). Note that the particular CO(2-1)/CO(1-0) is > 1 for $\zeta_{\text{CR}} \gtrsim 10^{-14} \text{ s}^{-1}$. Such a case is also observed in the CO(3-2)/CO(1-0) ratio for even higher ζ_{CR} , at which point however the distribution may become more atomic-dominated.

In the bottom row, the [C I](2-1)/CO(7-6) ratio is illustrated in panel (p). As with the non-star-forming ISM distribution (§5.1.1), [C I](2-1) is brighter than CO(7-6). In particular [C I](2-1) is $\sim 500 - 1000$ times brighter for $\chi/\chi_0 \lesssim 50$ and $\zeta_{\text{CR}} \lesssim 2 \times 10^{-16} \text{ s}^{-1}$ whereas it is just a few tens brighter otherwise. The [C I](1-0)/CO(4-3) ratio shown in panel (q)⁷, peaks for moderate ζ_{CR} ($\sim 10^{-15} \text{ s}^{-1}$) for low

⁷ Note on the instabilities of panel (q) for $\zeta_{\text{CR}} \sim 10^{-15} - 10^{-14} \text{ s}^{-1}$: numerical instabilities arise from the non-linear nature of the ordinary differential equations that are solved to achieve equilibrium in PDRs. Early work of Le Bourlot et al. (1993) demonstrated the existence of bi-stability in such solutions in dark molecular gas. Subsequent papers (e.g. Viti et al. 2001; Roueff & Le Bourlot 2020; Dufour & Charnley 2021) have also addressed and examined further bi-stability, especially in the oxygen chemistry. The instabilities seen in panel (q) (and elsewhere) is the result of the above.

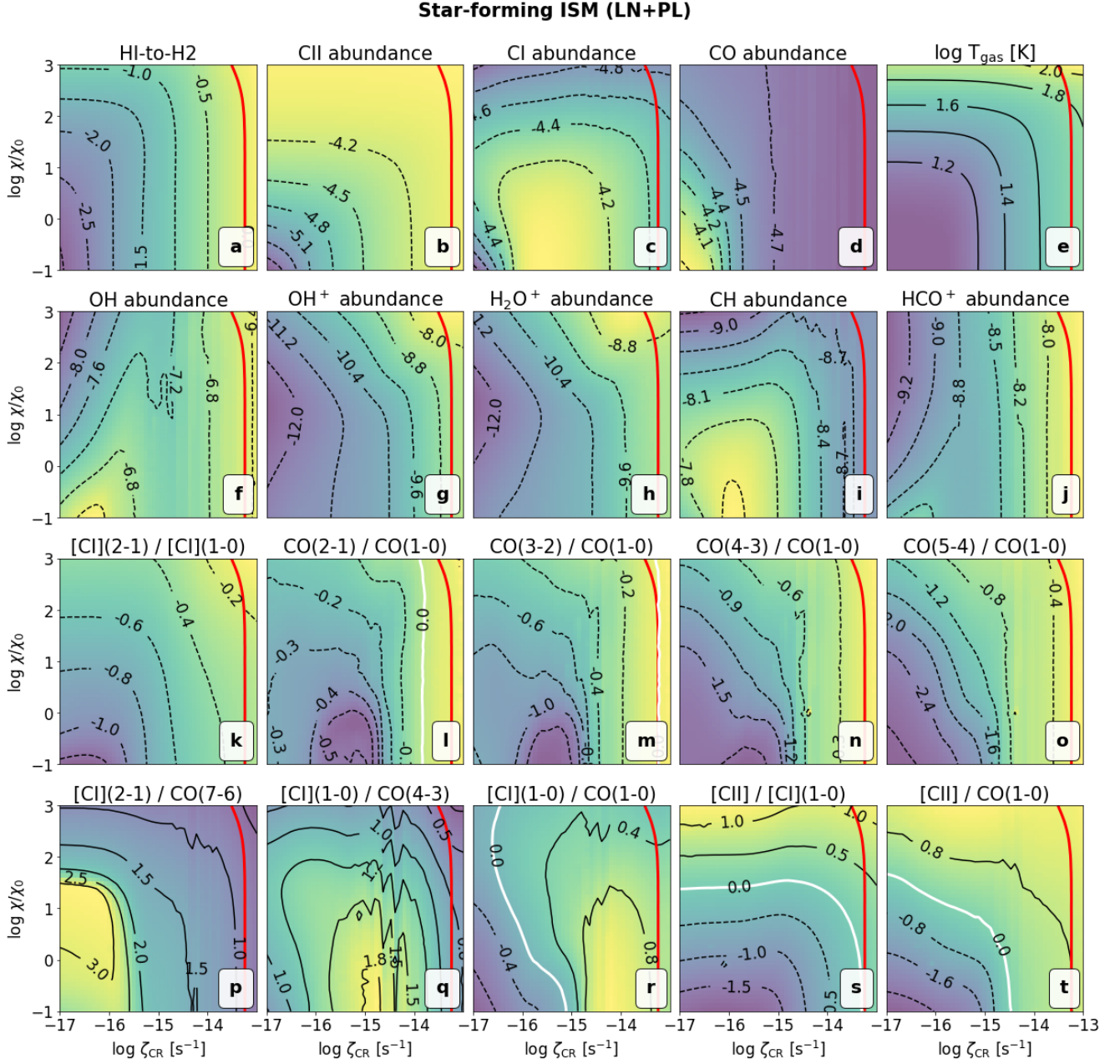


Figure 10. As in Fig. 8 but for the $A_{V,obs}$ -PDF of the star-forming ISM at solar metallicity, including both LN and PL components.

FUV intensities with $[C\text{I}](1-0)$ to be ~ 30 times brighter than $\text{CO}(4-3)$. Both aforementioned line ratios show a stronger correlation with ζ_{CR} than with χ/χ_0 .

Finally, in panels (r-t), the $[C\text{I}](1-0)/\text{CO}(1-0)$, $[C\text{II}]/[C\text{I}](1-0)$ and $[C\text{II}]/\text{CO}(1-0)$ are shown, respectively. The first ratio shows a stronger correlation with ζ_{CR} than the other two which are more sensitive on the FUV intensity. The antenna temperature of $[C\text{I}](1-0)$ is approximately equal to the $\text{CO}(1-0)$ for $3 \times 10^{-17} \lesssim \zeta_{\text{CR}} \lesssim 10^{-15} \text{ s}^{-1}$ depending on χ/χ_0 ; the lower the FUV intensity, the higher the cosmic-ray ionization rate needs to be to satisfy the equality of the $[C\text{I}](1-0)$ and $\text{CO}(1-0)$ antenna temperatures. For smaller ζ_{CR} , $\text{CO}(1-0)$ becomes brighter. Evidently, in systems containing high column densities and high cosmic-ray energy densities, $[C\text{I}](1-0)$ can be 4–6 times brighter than $\text{CO}(1-0)$ as indicated in the middle panel. In re-

gards to the $[C\text{II}]/[C\text{I}](1-0)$ ratio, it appears to be more sensitive to the χ/χ_0 value than the ζ_{CR} one. For $\chi/\chi_0 \lesssim 20$, this star-forming ISM distribution is brighter in $[C\text{I}](1-0)$ than $[C\text{II}]$. Similarly, as can be seen in the last panel, $\text{CO}(1-0)$ is brighter than $[C\text{II}]$ for any combination satisfying $\chi/\chi_0 \lesssim 10$ and $\zeta_{\text{CR}} \lesssim 2 \times 10^{-15} \text{ s}^{-1}$. In all other cases, the molecular gas may be primarily $[C\text{II}]$ -bright.

Appendix E discusses the behaviour of the optical depths for the star-forming ISM distribution. Figures F4–F6 show the corresponding results for $Z = 0.1, 0.5$ and $2.0 Z_{\odot}$, respectively.

5.2.2 Carbon phases at different metallicities

Figure 11 shows which carbon phase dominates for all ISM environmental parameters explored. The coloured results along with the

Star-forming ISM

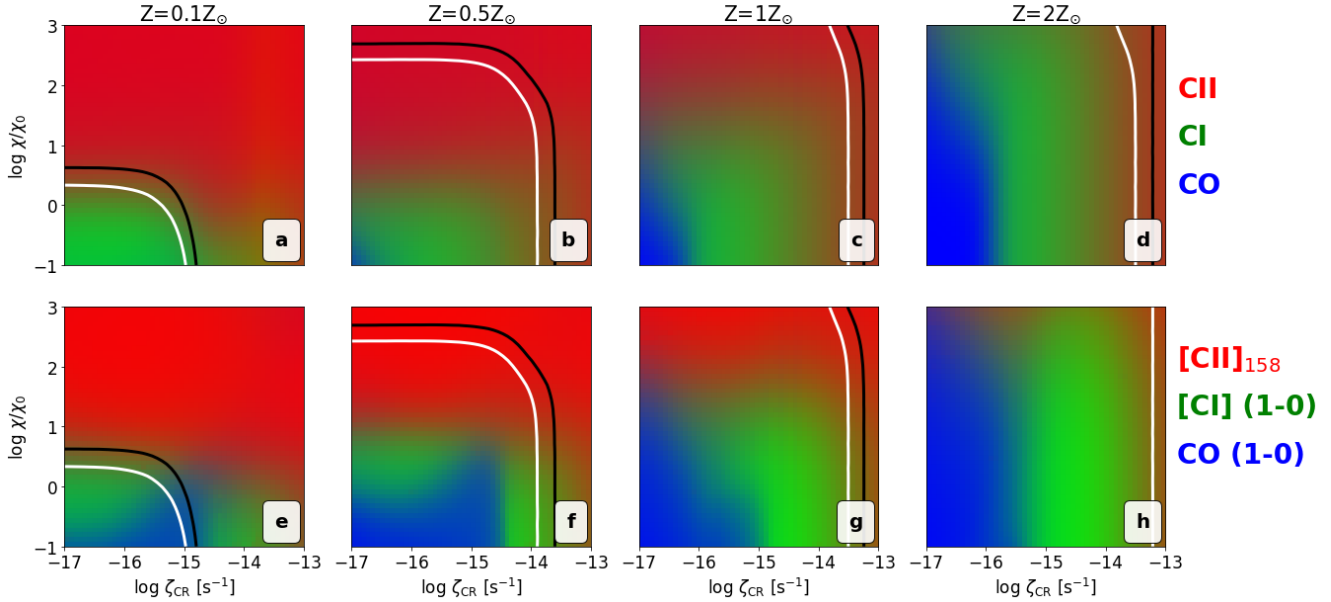


Figure 11. As in Fig. 9 for the star-forming ISM. The coloured results and the black solid line of the H_I-to-H₂ transition are for the LN+PL case. The white solid line corresponds to the results for the LN only case. For the carbon cycle abundances and emission, there are no appreciable differences between the LN+PL and LN cases.

black solid line of the H_I-to-H₂ transition correspond to the case where the power-law tail is included (LN+PL). The white solid line corresponds to the results where only the log-normal component is included (see §5.2.3 for the latter).

In regards to the abundances (top row), the H_I-to-H₂ transition changes with metallicity (see also §5.1.2), however this star-forming distribution remains molecular even at very low ($0.1 Z_{\odot}$) metallicities (panel a). Here, carbon is mostly found in the form of C_I in the molecular phase and C_{II} otherwise. For $Z = 0.5 Z_{\odot}$ (panel b) the molecular phase is mostly C_I dominated for $\chi/\chi_0 \lesssim 1$ (except for a negligible intensity of FUV radiation and for very low ζ_{CR} in which it is CO-dominated) but transitions to C_{II} for $\zeta_{\text{CR}} \gtrsim 10^{-14} \text{ s}^{-1}$. For $\chi/\chi_0 \gtrsim 1$ it is already C_{II}-dominated. At $Z = 1 Z_{\odot}$ (panel c), the C_I-dominated phase holds for $\chi/\chi_0 \approx 10$ but for $\zeta_{\text{CR}} \lesssim 10^{-16} \text{ s}^{-1}$, the majority of carbon is found in CO form. Interestingly, for $\zeta_{\text{CR}} \approx 10^{-17} \text{ s}^{-1}$, the carbon phase may switch from CO directly to C_{II} as χ/χ_0 increases, without a C_I-dominated phase (see also ‘Case-2’ of Paper I). Finally, when $Z = 2 Z_{\odot}$ (panel d), the star-forming distribution is found to remain molecular under all ISM conditions considered. The CO-dominated phase can exist for much higher FUV intensities, but it always transitions to C_I and then to C_{II} as ζ_{CR} increases to $\gtrsim 1 - 3 \times 10^{-16} \text{ s}^{-1}$ due to the cosmic-ray induced CO destruction effect. Notably, the C_I-dominated phase exists for a wide range of FUV intensities and metallicities but always transitions to C_{II} when $\zeta_{\text{CR}} \gtrsim 10^{-14} \text{ s}^{-1}$.

In regards to the brightness temperatures of the carbon cycle species (bottom row), for $Z = 0.1 Z_{\odot}$ (panel e) the molecular phase is in general bright in [C_I](1-0). For very low FUV intensities it is the antenna temperature of CO(1-0) that dominates depending on ζ_{CR} , even though it is rich in C_I abundance as seen in the top left panel. Interestingly, for $\chi/\chi_0 \lesssim 1$ the distribution remains [C_I](1-0) bright even for ζ_{CR} values for which the gas is in atomic form. At $Z = 0.5 Z_{\odot}$ (panel f), the molecular phase is bright in [C_I](1-0) for $\chi/\chi_0 \lesssim 5$, except when $\chi/\chi_0 \lesssim 1$ and $\zeta_{\text{CR}} \lesssim 3 \times 10^{-15} \text{ s}^{-1}$ in

which case it is bright in CO(1-0). For any stronger FUV intensity, the molecular gas is mainly [C_{II}]-bright. As with the $Z = 0.1 Z_{\odot}$ case, the medium is almost nowhere rich in CO abundance, although its line emission in the $J = 1 - 0$ transition can be strong.

At $Z = 1 Z_{\odot}$ (panel g), the gas is [C_{II}]-bright for $\chi/\chi_0 \gtrsim 20$, regardless to the ζ_{CR} value, since the gas is rich in C_{II} abundance due to photodissociation of CO. For lower FUV intensities, the gas is CO(1-0) bright for $\zeta_{\text{CR}} \lesssim 10^{-16} \text{ s}^{-1}$ on average. Note that for $\zeta_{\text{CR}} \sim 10^{-17} \text{ s}^{-1}$, the gas transitions from CO(1-0)-bright to [C_{II}]-bright, as well, directly when the FUV intensity exceeds approximately $20\chi_0$. As ζ_{CR} increases and for this low FUV intensity regime, this ISM distribution remains [C_I](1-0) even for very high cosmic-rays. Finally, for $Z = 2 Z_{\odot}$ (panel h), the gas is in practice either CO(1-0)-bright (for $\zeta_{\text{CR}} \lesssim 3 \times 10^{-16} \text{ s}^{-1}$) or [C_I](1-0)-bright otherwise. It may become [C_{II}] only for very extreme ISM environmental parameters. Note that for the latter two metallicity cases, the abundances (top third and fourth panels) and the line emission (bottom third and fourth panels) patterns agree well with each other.

5.2.3 Contribution of the power-law tail to the PDR results

As can be seen from Fig. 11, the power-law tail increases the contribution of the high column density material to the total one and, as such, it increases the total molecular gas mass content. This can be seen from the combination of the ISM conditions that are required for the H_I-to-H₂ transition to occur; in the LN case (white solid line) it occurs for somehow lower ζ_{CR} and lower χ/χ_0 when compared to the LN+PL case (black solid line). Overall, we find that the PL tail retains molecular conditions for twice the FUV intensity and twice the cosmic-ray ionization rate than the LN-only case.

We find that both the abundances and the line emissions of the carbon cycle remain in general very similar for the two cases. However, the PL tail slightly increases the CO abundance for higher χ/χ_0 (not plotted; see also Paper I).

In panels G1b,d of Appendix G, it is shown how the above results for $Z = 1 Z_{\odot}$ would differ if a lower A_V/N_H factor was adopted.

6 DISCUSSION

PDF_{CHEM} provides a fast calculation of key abundances and emission line ratios that are most commonly used, for large-scale (tens-to-hundreds of pc) inhomogeneous clouds characterized by an $A_{V,obs}$ -PDF. As described earlier, while many such distributions have been obtained for regions in the Milky Way, the limited resolution for extragalactic systems does not allow to determine such PDFs at high-redshift e.g. in the crucial $z \sim 2-3$ range for the cosmic star-formation theory (Madau & Dickinson 2014). In terms of spatial resolution, the ISM at $z \sim 2-3$ is observed at a sub-kpc resolution (see Hodge & da Cunha 2020, for a review with ALMA), unless gravitational lensing effects occur which may reveal scales of $\sim 100-200$ pc (e.g. Rybak et al. 2020; Solimano et al. 2021). It would be therefore interesting to use PDF_{CHEM} and input educated guesses of $A_{V,obs}$ distributions to explore the trends we may expect when studying extragalactic objects, particularly high-redshift galaxies.

Currently, such aforementioned educated guesses can arise from hydrodynamical models. For instance, simulations of the turbulent, star-forming ISM have explored the development of column density PDFs (e.g. Klessen, Heitsch, & Mac Low 2000; Federrath & Klessen 2013; Burkhardt & Mocz 2019). Particular attention has been paid on the transition of lognormal to power-law component, with the models suggesting that the power-law tail is a product of free-fall collapse forming filaments and dense clumps (Kritsuk, Norman, & Wagner 2011; Girichidis et al. 2014) including contribution from magnetic fields (Auddy, Basu, & Kudoh 2018). Overall, the majority of literature focuses on the description of $A_{V,obs}$ -PDFs resulting from GMC-scale models. Having shown in this work that such PDFs are valuable tools for a quick examination of the atomic/molecular content and their corresponding line emissions, we encourage the modelling community to enrich the current literature with more results and analyses on $A_{V,obs}$ -PDFs especially from galaxy-sized simulations.

6.1 Tracing molecular gas under different conditions

As discussed previously, the lower panels of Figs. 9 and 11 illustrate how the dominant carbon phase emitter –under molecular conditions– changes as a function of the ISM environmental parameters. The carbon cycle transitions are found to be more strongly correlated with the ISM conditions, than the H_I-to-H₂ transition is. Consequently, the ISM parameters affect the methodology of tracing the H₂ gas as well as the corresponding conversion factors.

In this work, we introduce the quantity $X_* \equiv \langle N(H_2) \rangle / \langle T_* \rangle$ representing the ratio of the PDF-averaged H₂ column density and the PDF-averaged antenna temperature of the emitter. This ratio has units of [cm⁻² K⁻¹] and it differs from the standard ‘X-factor’ by the linewidth. X is used here to illustrate the expected behaviour of the commonly used conversion factors (e.g. the CO- or the CI-to-H₂) under the different ISM conditions. The reader should be aware that the presented results are further prone to the choice of the inputted column density PDF and they should, thus, only be considered to demonstrate qualitatively (rather than quantitatively) the trends of X-factors. Figure 12 shows a collective map of how X changes as a function of the ISM environmental parameter explored. The star-forming $A_{V,obs}$ -PDF was adopted for these calculations, to best represent a dense molecular region. The top row of Fig. 12 shows the $X_{[CII]}$ ratio while the middle and bottom rows the $X_{[CI](1-0)}$

and $X_{CO(1-0)}$, respectively. Each column corresponds to different metallicity.

The use of [CII] as an H₂ tracer is frequently adopted for high- z galaxies (e.g. Zanella et al. 2018; Madden et al. 2020; Vizgan et al. 2022), thanks to ALMA’s ability to observe this line in the very distant Universe. Using [CII] for such estimations is, however, not straightforward since significant fraction of the total [CII] luminosity can originate from the non-molecular ISM, such as HII regions and the warm neutral medium (e.g. Accurso et al. 2017a; Bisbas et al. 2022). For the [CII] emission to correlate with $N(H_2)$ for high columns of H₂, a heating mechanism is needed capable of exciting this line –such as cosmic-rays (see B21)– given its high excitation temperature of $h\nu/k \sim 91.2$ K. Panels (a)-(d) indicate a decreasing trend of $X_{[CII]}$ with increasing χ/χ_0 and ζ_{CR} . For metallicities of $\geq 0.5 Z_{\odot}$ it can vary up to two orders of magnitude depending on the combination of the ISM conditions. For high metallicities (e.g. $Z \sim 2 Z_{\odot}$), [CII] shows a strong correlation for $\zeta_{CR} \gtrsim 10^{-15} \text{ s}^{-1}$. Such conditions are met in starburst galaxies in the high- z Universe as well as the Galactic Center (Giveon et al. 2002; Clark et al. 2013).

The debate between [CI](1-0) and CO(1-0) as ‘best of H₂ gas tracers’ is of great interest (e.g. Papadopoulos, Thi, & Viti 2004; Bolatto, Wolfire, & Leroy 2013a; Offner et al. 2014 and B21). From the [CI](1-0) results shown in panels (e)-(h), it is found that its corresponding ratio with $N(H_2)$ remains approximately constant under molecular conditions for $Z = 0.1 Z_{\odot}$. For similar ζ_{CR} and χ/χ_0 pairs (e.g. $\zeta_{CR} \lesssim 10^{-15} \text{ s}^{-1}$ and $\chi/\chi_0 < 5$) in all other metallicity cases, $X_{[CI](1-0)}$ also remains to within the same range, thus making it to weakly depend on Z . For $Z \gtrsim 0.5 Z_{\odot}$ and as ζ_{CR} increases, the latter ratio slightly decreases while for higher χ/χ_0 , it slightly increases.

Panels (i)-(l) illustrate the dependency of $X_{CO(1-0)}$ on the ISM parameters. There is a stronger correlation with metallicity in agreement with observations (e.g. Genzel et al. 2012; Shi et al. 2015, 2016; Amorín et al. 2016; Schrubba et al. 2017). In the $Z = 0.1$ and $0.5 Z_{\odot}$ cases, $X_{CO(1-0)}$ has a minimum for $\zeta_{CR} \sim 10^{-15} \text{ s}^{-1}$ and low χ/χ_0 . For higher metallicities (panels k, l), it depends predominantly on the value of ζ_{CR} . In particular, $X_{CO(1-0)}$ can vary up to one order of magnitude as ζ_{CR} increases. On the contrary, panels (f)-(h) show that for high ζ_{CR} , $X_{[CI](1-0)}$ is approximately constant making it an excellent alternative tracer in such environments (Bisbas, Papadopoulos, & Viti 2015; Bisbas et al. 2017b). Overall, the pattern of the dominant carbon emitter illustrated in the bottom row of Fig. 11 is reflected in the X_* ratios of Fig. 12; the ratio of the dominant emitter minimizes when its antenna temperature peaks.

6.2 The HCO⁺/CO abundance ratio as a cosmic-ray tracer

The abundance ratio of HCO⁺/CO has been used in the past to infer the cosmic-ray ionization rate (Wootten, Snell, & Glassgold 1979; Caselli et al. 1998; Vaupré et al. 2014). In particular, elevated HCO⁺/CO abundance ratios have been connected with increased cosmic-ray ionization rates. Gaches, Offner, & Bisbas (2019) obtain high HCO⁺/CO abundance ratios for models with high ζ_{CR} values and without embedded sources at high column densities (their HNI model), which can change the local chemistry and thus affect that ratio.

Figure 13 shows HCO⁺/CO abundance ratio maps for both $A_{V,obs}$ -PDF cases considered and how these compare with observations. Panels (a)-(c) illustrate the HCO⁺/CO ratio for the star-forming $A_{V,obs}$ -PDF for $Z = 1.0 Z_{\odot}$ (panels a, b) and for $Z = 2.0 Z_{\odot}$ (panel c). Panel (d) shows the non-star-forming PDF for $Z = 1.0 Z_{\odot}$. In all cases, the observed data are marked in blue shadow. As can be seen, the star-forming PDFs show a strong dependence of HCO⁺/CO

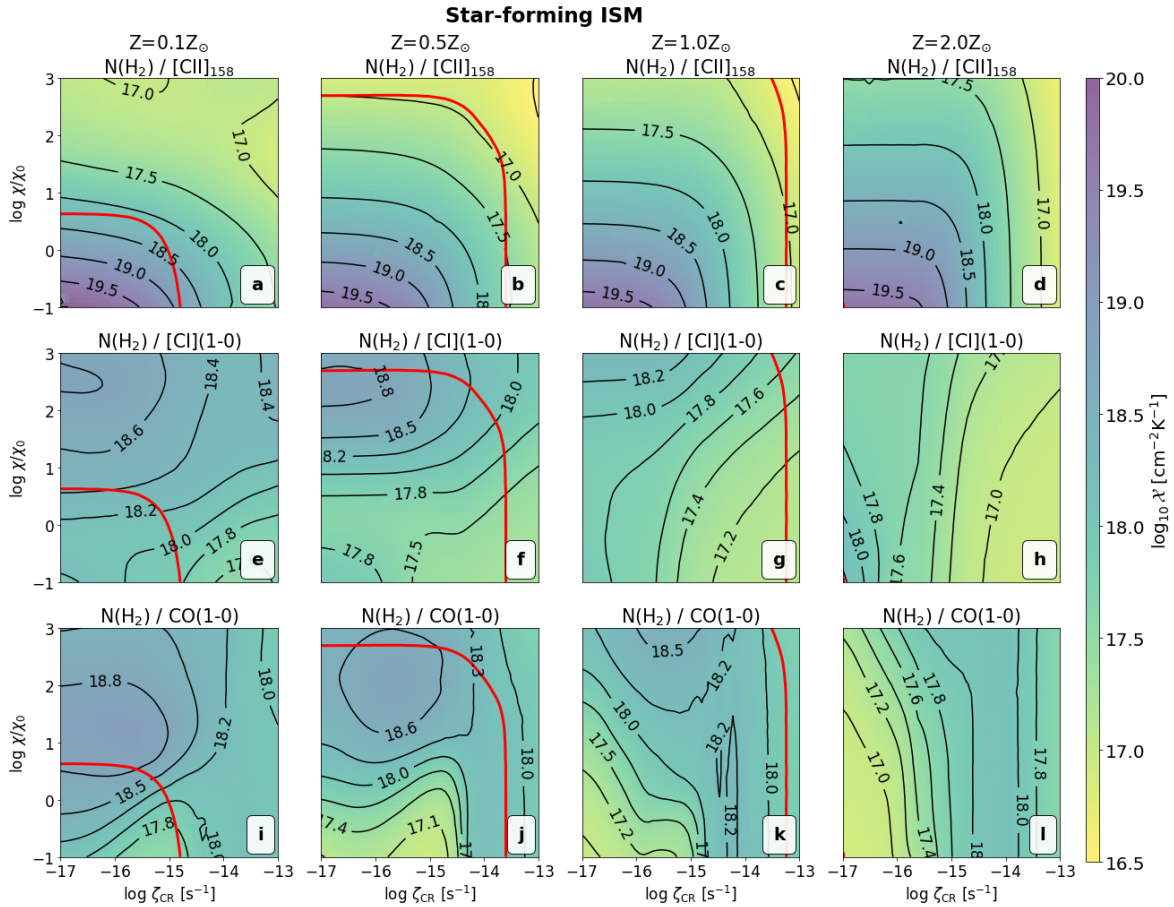


Figure 12. Logarithmic grid maps showing ratios of the PDF-averaged H_2 column density to the PDF-averaged antenna temperature of each tracer (units of $\text{cm}^{-2} \text{K}^{-1}$). Each column corresponds to a different metallicity (left-to-right: $Z = 0.1, 0.5, 1.0, 2.0 Z_\odot$) and each row to a different tracer (top-to-bottom: $[\text{C I}] 158\mu\text{m}$, $[\text{C I}](1-0)$, $\text{CO } J = 1 - 0$). The star-forming $A_{\text{V,obs}}$ -PDF has been used in all cases. The colour bar shows the logarithm of the X -factor.

ratio with ζ_{CR} . However, it is found that under molecular conditions and for the non-star-forming PDF, it depends more strongly on the value of χ/χ_0 rather the ζ_{CR} one.

Panel (a) highlights the observed HCO^+/CO abundance ratio in the supernova remnant W49B obtained by Zhou et al. (2022) who reported a ratio in the range of $\log_{10}(\text{HCO}^+/\text{CO}) = -3.52$ to -2.70 . They attributed it to the presence of high ζ_{CR} and suggested that it can well be more than two orders of magnitude higher than the average Galactic one. Indeed, this ratio fits for high ζ_{CR} in our models indicating a $\zeta_{\text{CR}} \gtrsim 3 \times 10^{-15} \text{ s}^{-1}$. While Zhou et al. (2022) do not report on the column density distribution, the selected $A_{\text{V,obs}}$ -PDF used here is to represent a dense clump.

Panel (b) shows the observations of Young et al. (2021) for the nucleus of NGC 7465 which is a low-redshift early-type galaxy (Cappellari et al. 2011). This panel has the same PDF and metallicity as panel (a). The observed metallicity of this system is approximately solar. Young et al. (2021) calculated the ^{12}CO and HCO^+ column densities for two representative temperatures (20 and 90 K) in the optically thin limit. These lead to a range of HCO^+/CO ratio of $\log_{10} \text{HCO}^+/\text{CO} = -3.75$ to -3.73 , for which PDFCHEM finds a $\zeta_{\text{CR}} \sim 3 - 4 \times 10^{-15} \text{ s}^{-1}$. These elevated ζ_{CR} values are reasonable to expect in an ISM region located in the center of galaxies such as NGC 7465.

Panel (c) shows the observed ratio for the central part in the NGC 253 galaxy (Krieger et al. 2020). This central part contains

several regions of proto-super star clusters and they are thus best represented with the star-forming $A_{\text{V,obs}}$ -PDF. NGC 253 is known to be a starburst galaxy of high star-forming activity (Bolatto et al. 2013b) and of super-solar metallicity (e.g. $Z \sim 2.19 Z_\odot$ Galliano, Dwek, & Chantal 2008). The shadowed region in panel (c) represents the mean and the 1σ standard deviation of the Krieger et al. (2020) reported values. These lead to a high ζ_{CR} of approximately 10^{-14} s^{-1} . Interestingly, such high values of cosmic-ray ionization rate have been independently reported (e.g. Holdship et al. 2021), confirming the PDFCHEM findings.

Finally, in panel (d) the resultant calculations for a region representing the diffuse ISM of Milky Way are shown. Here, the non-star-forming $A_{\text{V,obs}}$ -PDF has been used for a better comparison. The observed values were taken by Godard, Falgarone, & Pineau des Forêts (2014) and are shown in the aforementioned panel. Under molecular conditions, the reported ratio reveals an FUV intensity in the range of $\chi/\chi_0 \sim 1 - 5$, which matches with the average FUV intensity of Milky Way away from the Galactic Center. Under atomic conditions (which reveal a much higher pair of χ/χ_0 and ζ_{CR}), both lines are expected to be very weak and thus non-observable.

6.3 Line ratios as FUV and ζ_{CR} diagnostics

Many lines in the carbon cycle ($[\text{C II}]$, both $[\text{C I}]$ and high- J CO transitions) have been observed at a redshift of $\sim 2 - 3$ and beyond

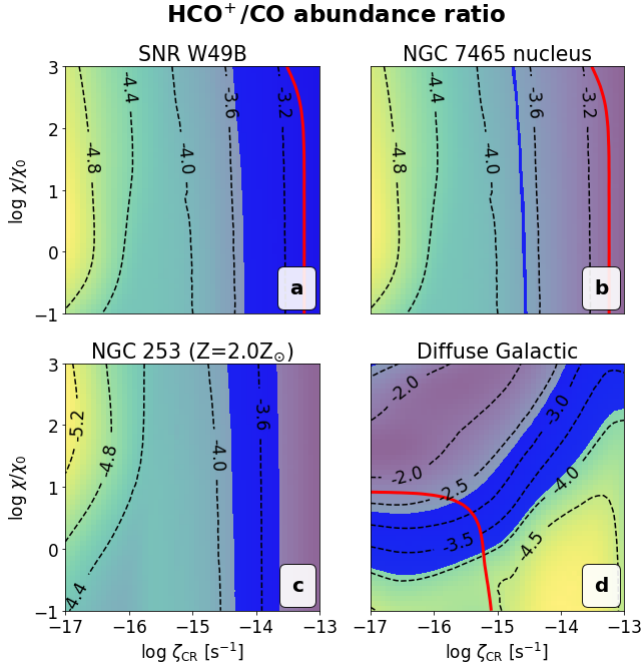


Figure 13. The HCO^+/CO abundance ratio. The blue-shadowed regions represent observations (see §6.2 for details). Panels (a)–(c) show this ratio for the star-forming $A_{V,\text{obs}}$ -PDF. Panels (a) and (b) are for $Z = 1.0 Z_\odot$ while panel (c) for $Z = 2.0 Z_\odot$. In these cases, the HCO^+/CO abundance ratio depends almost entirely from the ζ_{CR} value. Panel (d) shows the ratio for the non-star-forming $A_{V,\text{obs}}$ -PDF for $Z = 1.0 Z_\odot$. In this case and under molecular conditions, the abundance ratio does not depend strongly on ζ_{CR} but rather on the χ/χ_0 value.

(see relevant works in the reviews of [Hodge & da Cunha 2020](#); [Wolfire, Vallini, & Chevance 2022](#)), their combinations of which can constrain the ISM environmental parameters using PDF_{CHEM}, thus offering a deeper understanding on the conditions leading to star-formation. While such observations have revealed the cosmic history of star-formation, they have yet to quantify the connection between the ISM environmental parameters and the SFR. The latter quantity is generally traced with the $[\text{CII}]$ emission at high redshifts, since the $[\text{CII}]$ -SFR relation has been extensively explored with observations (e.g. [Stacey et al. 1991, 2010](#); [Boselli et al. 2002](#); [De Looze et al. 2011](#); [Herrera-Camus et al. 2015](#)) and simulations (e.g. [Olsen et al. 2015](#); [Lupi & Bovino 2020](#); [Bisbas et al. 2022](#)). It is reasonable to expect that high SFRs imply high ζ_{CR} and possibly also high χ/χ_0 intensities, since both should be enhanced due to the expected higher rate of supernova explosions. In general, high SFRs are found in mergers, starbursts, ULIRGs and submillimeter galaxies (e.g. [Smail, Ivison, & Blain 1997](#); [Hughes et al. 1998](#); [Daddi et al. 2010, 2015](#)).

The $[\text{CII}]/[\text{CI}](1-0)$ ratio explored in this work, shows that it may well be used to diagnose FUV intensities since its dependence on ζ_{CR} is weak (for $\lesssim 10^{-14} \text{ s}^{-1}$) regardless to the choice of A_V -PDF (see also [Bothwell et al. 2017](#), for an analysis with uniform density slabs). This remains valid even for different metallicities as can be seen in panel (s) of Figs. F1–F5. Interestingly, for $Z = 2 Z_\odot$ (panel F6s) the above ratio shows a stronger dependence on ζ_{CR} for $\zeta_{\text{CR}} \gtrsim 10^{-15} \text{ s}^{-1}$. [Bothwell et al. \(2017\)](#) report a $[\text{CII}]/[\text{CI}](1-0)$ ratio in the (logarithmic) range of $\sim 0.9 - 1.6$ for ten high-redshift ($z \sim 4$) dusty star-forming galaxies and they further perform PDR modelling assuming an average $A_{V,\text{obs}} \sim 7 \text{ mag}$. This matches with our star-

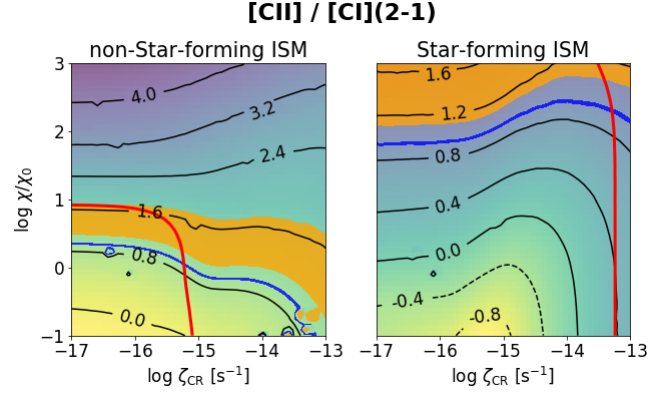


Figure 14. The average brightness temperature of $[\text{CII}]/[\text{CI}](2-1)$ for the non-star-forming ISM (left panel) and the star-forming ISM (right panel). The blue thick line and the orange shaded region correspond to the [Venemans et al. \(2017\)](#) and [Pensabene et al. \(2021\)](#) observations, respectively.

forming PDF and from panel (s) of Fig. 10 it is found that the above ratio predicts an FUV intensity of $\log_{10} \chi/\chi_0 > 2.5$. Interestingly, these high intensities calculated with PDF_{CHEM} are matching those estimated by [Bothwell et al. \(2017\)](#).

Due to the weak dependence on CRs, the $[\text{CII}]/[\text{CI}](2-1)$ line ratio has been considered as a tracer for the presence of X-rays in the ISM. This ratio is illustrated in Fig. 14, which shows a strong dependence on the FUV intensity, like the $[\text{CII}]/[\text{CI}](1-0)$ explored above. Earlier models of [Meijerink, Spaans, & Israel \(2007\)](#) showed that this ratio depends strongly on the intensity of X-ray flux; it is increasing with increasing X-ray fluxes. This led [Venemans et al. \(2017\)](#) who studied the ISM of a very distant ($z \sim 7.1$) quasar J1120+0641 to conclude that the aforementioned (lower limit) ratio of $\log_{10}([\text{CII}]/[\text{CI}](2-1)) = 0.94$ originates from existing PDRs that are a result of the FUV radiation from hot stars, rather than hard X-rays from the accreting central black hole. This observed ratio is marked with blue line in Fig. 14. PDF_{CHEM} predicts an $\log \chi/\chi_0 \sim 0.5 - 2$ depending on the PDF distribution (for $Z = 1.0 Z_\odot$). In addition, [Pensabene et al. \(2021\)](#) used the $[\text{CII}]/[\text{CI}](2-1)$ ratios of $\log_{10}([\text{CII}]/[\text{CI}](2-1)) \sim 1.11 - 1.72$ to identify PDRs in the galaxies PJ231-20 ($z = 6.23$) and PJ308-21 ($z = 6.59$) which are two quasar host galaxies. The orange shadowed region of Fig. 14 marks these observations and as with the last finding, they may correspond to high FUV intensities for high- $A_{V,\text{obs}}$ PDF distributions.

[Boogaard et al. \(2020\)](#) studied the $\text{CO}(2-1)/\text{CO}(1-0)$ and $\text{CO}(3-2)/\text{CO}(1-0)$ ratios in a sample of 22 star-forming galaxies in $0.46 < z < 3.60$ as part of the ASPECS⁸ survey. They found a $\text{CO}(2-1)/\text{CO}(1-0)$ ratio of ~ 0.75 for $z < 2$ and a $\text{CO}(3-2)/\text{CO}(1-0)$ ratio of ~ 0.77 for $z \geq 2$, arguing that the higher excitation of the latter ratio is a result of the Σ_{SFR} increase with redshift. Interestingly, the $\text{CO}(2-1)/\text{CO}(1-0)$ ratio fits our results for the star-forming $A_{V,\text{obs}}$ -PDF for a ζ_{CR} of a few $\times 10^{-15} \text{ s}^{-1}$ (panel 10l), regardless to the FUV intensity, while for the $\text{CO}(3-2)/\text{CO}(1-0)$ ratio we find a ζ_{CR} of a few $\times 10^{-14} \text{ s}^{-1}$ (panel 10m). The higher ζ_{CR} reflects the global picture in which we expect to find higher cosmic-ray energy densities in star-forming galaxies, particularly at $z \sim 2 - 3$.

The pattern of $\text{CO}(5-4)/\text{CO}(1-0)$ ratio illustrated in the panel (10o), shows that high- J CO lines depend very weakly on the FUV inten-

⁸ ALMA Spectroscopic Survey in the Hubble Ultra Deep Field

sity and thus can be used to constrain heating processes that operate at high column densities, other than stellar photons. In this regard, a combination of CO SLEDs with dust continuum spectral energy distributions (e.g. [Harrington et al. 2021](#)) can reveal these heating processes as to whether or not they are photon-dominated, by estimating the so-called Y -factor ($Y = \Gamma_{\text{PE}}/\Lambda_{\text{tot}}$, the ratio of photoelectric heating to the total cooling, see [Papadopoulos et al. 2014](#)). The advent of ALMA has made possible to observe high- J CO lines in the distant Universe which points to the existence of warm and dense medium. For instance, the $J = 10 - 9$ transition requires a gas temperature of $T_{\text{gas}} \gtrsim 300$ K to be excited and has a critical density of $n_{\text{crit}} \sim 10^6 \text{ cm}^{-3}$. In addition, the NOEMA detection of very high- J CO lines ($J = 17 - 16$) in very distant ($z > 6$) galaxies ([Gallerani et al. 2014](#)) makes it possible to investigate the ISM and constrain its parameters even in the Early Universe. In these galaxies, it is not only cosmic-rays that may cause an elevated SLED. X-rays (e.g. [Vallini et al. 2018, 2019](#); [Pensabene et al. 2021](#)), shock heating (e.g. [Li et al. 2020](#); [Riechers et al. 2021](#)) and/or turbulence ([Harrington et al. 2021](#)) can also play a significant role. Exploring high- J transitions with the presented version of PDFCHEM can help the investigation of these heating processes, primarily by disentangling the contribution due to FUV photons. Future versions of PDFCHEM will be able to provide a further constrain on the heating processes.

In general, for applications of PDFCHEM in high-redshift galaxies in which the $A_{\text{V,obs}}$ -PDFs remain largely unknown, we recommend the use of distributions corresponding to a diffuse or a dense medium according to local observations (e.g. [Spilker, Kainulainen, & Orkisz 2021](#); [Ma et al. 2022](#)) or inspired from simulations (e.g. see recent works of [Veltchev et al. 2019](#); [Seifried et al. 2020b](#); [Olsen et al. 2021](#); [Appel et al. 2022](#)). These can make possible to obtain an insight of the PDR trends and to provide a probable range of environmental parameters which, using additional forward modelling, may identify the ISM conditions.

7 CONCLUSIONS

In this paper we present the PDFCHEM algorithm, which continues the approach of [Paper I](#) in determining the atomic and molecular mass content of the ISM using probability distributions of physical parameters. For the purposes of PDR simulations, we consider a variable density distribution resulting from the $A_{\text{V,eff}} - n_{\text{H}}$ relationship which replaces the grid of uniform density slabs used in [Paper I](#). We have performed radiative transfer calculations to determine ratios between emissions of the most commonly used lines of the carbon cycle. The grid of PDR simulations consists of 6,400 one-dimensional runs covering a wide range of cosmic-ray ionization rates, FUV intensities and metallicities. We applied PDFCHEM to two hypothetical $A_{\text{V,obs}}$ -PDFs representing a non-star-forming and a star-forming ISM distributions. Our results can be summarized as follows:

- (i) The demanding inhomogeneous PDR calculations in advanced three-dimensional hydrodynamical simulations can be reproduced by a simple one-dimensional density distribution (the ‘variable density slab’) and which results from the empirical $A_{\text{V,eff}} - n_{\text{H}}$ relation of Eqn. 3. We distinguish between the effective (local) and the observed visual extinctions, $A_{\text{V,eff}}$ and $A_{\text{V,obs}}$ respectively, and we show that for a better interpretation of the observed PDR data, a conversion relation between these two quantities must be considered (Eqn. 6).
- (ii) The non-star-forming distribution remains molecular for a combination of low FUV intensities and low ζ_{CR} . In the extreme

case of $Z = 0.1 Z_{\odot}$ it is always atomic, whereas in the case of $Z = 2 Z_{\odot}$ it remains molecular for higher combinations of χ/χ_0 and ζ_{CR} . Its molecular phase is almost always CII-dominated in terms of the abundance, and it is [CII]-bright for $\chi/\chi_0 > 1$. For lower FUV intensities it is either CO(1-0) or [CI](1-0) bright depending on ζ_{CR} . This distribution remains in general optically thin in [CII] and [CI](1-0), but can become quickly CO(1-0) optically thick.

(iii) The star-forming distribution remains molecular for almost any combination of $\chi/\chi_0 - \zeta_{\text{CR}}$ explored, except when $Z = 0.1 Z_{\odot}$ for which it is atomic for $\chi/\chi_0 > 5$ and $\zeta_{\text{CR}} > 10^{-15} \text{ s}^{-1}$. In terms of the abundance, the molecular phase is dominated either by CII, CI or CO depending on the ISM conditions. Similarly, it can be either [CII], [CI](1-0) or CO(1-0) bright when it comes to line emission. In general, the power-law tail does not significantly affect the results of the log-normal component, but we do observe a change in the conditions leading to the H_I-to-H₂ transition. This distribution remains in principle optically thin in [CII]. It is also optically thin in [CI](1-0) for sub-solar metallicities only. As with the non-star-forming distribution, it is almost always optically thick in CO(1-0).

(iv) We find that the CO-to-H₂ conversion factor depends more strongly on the ISM environmental parameters than the CI-to-H₂ does. The latter is found to depend weakly on metallicity and remains approximately constant for $\zeta_{\text{CR}} \gtrsim 10^{-15} \text{ s}^{-1}$, making it a powerful alternative tracer to CO in such environments. As an H₂ tracer, [CII] is found to remain remarkably independent of metallicity. It decreases when both the FUV intensity and metallicity increase and for high cosmic-ray energy densities, it depends almost entirely on ζ_{CR} .

(v) We identify the HCO⁺/CO abundance ratio as a tool to constrain the ζ_{CR} value. Contrary to the non-star-forming distribution, we find that for the star-forming $A_{\text{V,obs}}$ -PDF, it remains largely independent of the value of the FUV intensity. We also identify the [CII]/[CI](1-0) and [CII]/[CI](2-1) line ratios as useful tools to constrain the FUV intensity, as they both depend weakly on the ζ_{CR} value.

The significant advantage of PDFCHEM over 3D-hydro+radiative transfer codes to solve for the PDR properties in a negligible computational time, allows the exploration of various combinations of PDFs and to understand the ISM properties of large-scale systems including local clouds and high-redshift galaxies.

DATA AVAILABILITY

The data underlying this article will be shared on reasonable request to the corresponding author.

ACKNOWLEDGEMENTS

The authors thank the anonymous referee for useful comments which improved the clarity of this work. The authors thank Pierre Nürnberg for improving the quality of Figures 9 and 11 and Kei Tanaka for the discussions. TGB acknowledges support from Deutsche Forschungsgemeinschaft (DFG) grant No. 424563772. EvD is supported by the European Research Council (ERC) under the European Union’s Horizon 2020 research and innovation program (grant agreement No. 101019751 MOLDISK). CYH acknowledges support from the DFG via German-Israel Project Cooperation grant STE1869/2-1 GE625/17-1.

REFERENCES

- Abreu-Vicente J., Kainulainen J., Stutz A., Henning T., Beuther H., 2015, *A&A*, 581, A74.
- Accurso G., Saintonge A., Bisbas T. G., Viti S., 2017a, *MNRAS*, 464, 3315.
- Accurso G., Saintonge A., Catinella B., Cortese L., Davé R., Dunsheath S. H., Genzel R., et al., 2017b, *MNRAS*, 470, 4750.
- Allen R. J., Hogg D. E., Engelke P. D., 2015, *AJ*, 149, 123.
- Amorín R., Muñoz-Tuñón C., Aguerri J. A. L., Planesas P., 2016, *A&A*, 588, A23.
- Appel S. M., Burkhard B., Semenov V. A., Federrath C., Rosen A. L., 2022, *ApJ*, 927, 75.
- Asplund M., Grevesse N., Sauval A. J., Scott P., 2009, *ARA&A*, 47, 481.
- Auddy S., Basu S., Kudoh T., 2018, *MNRAS*, 474, 400.
- Bellocchi E., Martín-Pintado J., Güsten R., Requena-Torres M. A., Harris A., van der Werf P. P., Israel F. P., et al., 2020, *A&A*, 642, A166.
- Bergin E. A., Hartmann L. W., Raymond J. C., Ballesteros-Paredes J., 2004, *ApJ*, 612, 921.
- Beuther H., Ragan S. E., Ossenkopf V., Glover S., Henning T., Linz H., Nielbock M., et al., 2014, *A&A*, 571, A53.
- Bialy S., Sternberg A., 2015, *MNRAS*, 450, 4424.
- Bialy S., Neufeld D., Wolfire M., Sternberg A., Burkhard B., 2019, *ApJ*, 885, 109.
- Bialy S., 2020, *ApJ*, 903, 62.
- Bigiel F., de Looze I., Krabbe A., Cormier D., Barnes A. T., Fischer C., Bolatto A. D., et al., 2020, *ApJ*, 903, 30.
- Bisbas T. G., Bell T. A., Viti S., Yates J., Barlow M. J., 2012, *MNRAS*, 427, 2100.
- Bisbas T. G., Papadopoulos P. P., Viti S., 2015, *ApJ*, 803, 37.
- Bisbas T. G., van Dishoeck E. F., Papadopoulos P. P., Szűcs L., Bialy S., Zhang Z.-Y., 2017a, *ApJ*, 839, 90.
- Bisbas T. G., Tanaka K. E. I., Tan J. C., Wu B., Nakamura F., 2017b, *ApJ*, 850, 23.
- Bisbas T. G., Schruha A., van Dishoeck E. F., 2019, *MNRAS*, 485, 3097. (Paper I)
- Bisbas T. G., Tan J. C., Tanaka K. E. I., 2021, *MNRAS*, 502, 2701. (B21)
- Bisbas T. G., Walch S., Naab T., Lahén N., Herrera-Camus R., Steinwandell U. P., Fotopoulou C. M., et al., 2022, *arXiv*, arXiv:2205.08905
- Black J. H., Dalgarno A., 1973, *ApL*, 15, 79
- Bohlin R. C., Savage B. D., Drake J. F., 1978, *ApJ*, 224, 132.
- Bolatto A. D., Wolfire M., Leroy A. K., 2013a, *ARA&A*, 51, 207.
- Bolatto A. D., Warren S. R., Leroy A. K., Walter F., Veilleux S., Ostriker E. C., Ott J., et al., 2013b, *Nature*, 499, 450.
- Boogaard L. A., van der Werf P., Weiss A., Popping G., Decarli R., Walter F., Aravena M., et al., 2020, *ApJ*, 902, 109
- Boselli A., Gavazzi G., Lequeux J., Pierini D., 2002, *A&A*, 385, 454.
- Bothwell M. S., Aguirre J. E., Aravena M., Bethermin M., Bisbas T. G., Chapman S. C., De Breuck C., et al., 2017, *MNRAS*, 466, 2825.
- Bradford C. M., Nikola T., Stacey G. J., Bolatto A. D., Jackson J. M., Savage M. L., Davidson J. A., et al., 2003, *ApJ*, 586, 891.
- Burkhard B., Mocz P., 2019, *ApJ*, 879, 129.
- Cappellari M., Emsellem E., Krajnović D., McDermid R. M., Scott N., Verdoes Kleijn G. A., Young L. M., et al., 2011, *MNRAS*, 413, 813.
- Cardelli J. A., Meyer D. M., Jura M., Savage B. D., 1996, *ApJ*, 467, 334.
- Cartledge S. I. B., Lauroesch J. T., Meyer D. M., Sofia U. J., 2004, *ApJ*, 613, 1037.
- Caselli P., Walmsley C. M., Terzieva R., Herbst E., 1998, *ApJ*, 499, 234.
- Clark P. C., Glover S. C. O., Ragan S. E., Shetty R., Klessen R. S., 2013, *ApJL*, 768, L34.
- Clark P. C., Glover S. C. O., 2014, *MNRAS*, 444, 2396.
- Daddi E., Bournaud F., Walter F., Dannerbauer H., Carilli C. L., Dickinson M., Elbaz D., et al., 2010, *ApJ*, 713, 686.
- Daddi E., Dannerbauer H., Liu D., Aravena M., Bournaud F., Walter F., Riechers D., et al., 2015, *A&A*, 577, A46.
- De Looze I., Baes M., Bendo G. J., Cortese L., Fritz J., 2011, *MNRAS*, 416, 2712.
- Draine B. T., 1978, *ApJS*, 36, 595.
- Dufour G., Charnley S. B., 2021, *ApJ*, 909, 171.
- Dullemond, C. P., Juhasz, A., Pohl, A., et al. 2012, *Astrophysics Source Code Library*.
- Esposito F., Vallini L., Pozzi F., Casasola V., Mingozi M., Vignali C., Grupcioni C., et al., 2022, *MNRAS*, 512, 686.
- Federman S. R., Rawlings J. M. C., Taylor S. D., Williams D. A., 1996, *MNRAS*, 279, L41.
- Federrath C., Klessen R. S., 2013, *ApJ*, 763, 51.
- Feldmann R., Gnedin N. Y., Kravtsov A. V., 2012, *ApJ*, 747, 124.
- Ferland G. J., Korista K. T., Verner D. A., Ferguson J. W., Kingdon J. B., Verner E. M., 1998, *PASP*, 110, 761.
- Ferland G. J., Chatzikos M., Guzmán F., Lykins M. L., van Hoof P. A. M., Williams R. J. R., Abel N. P., et al., 2017, *RMxAA*, 53, 385
- Flannery B. P., Roberge W., Rybicki G. B., 1980, *ApJ*, 236, 598.
- Froebrich D., Rowles J., 2010, *MNRAS*, 406, 1350.
- Gaches B. A. L., Offner S. S. R., Bisbas T. G., 2019, *ApJ*, 878, 105.
- Gaches B. A. L., Bisbas T. G., Bialy S., 2022, *A&A*, 658, A151.
- Galametz M., Schruha A., De Breuck C., Immer K., Chevance M., Galliano F., Gusdorf A., et al., 2020, *A&A*, 643, A63.
- Gallerani S., Ferrara A., Neri R., Maiolino R., 2014, *MNRAS*, 445, 2848.
- Galliano F., Dwek E., Charnley P., 2008, *ApJ*, 672, 214.
- Garratt T. K., Coppin K. E. K., Geach J. E., Almaini O., Hartley W. G., Maltby D. T., Simpson C. J., et al., 2021, *arXiv*, arXiv:2103.08613
- Genzel R., Tacconi L. J., Gracia-Carpio J., Sternberg A., Cooper M. C., Shapiro K., Bolatto A., et al., 2010, *MNRAS*, 407, 2091.
- Genzel R., Tacconi L. J., Combes F., Bolatto A., Neri R., Sternberg A., Cooper M. C., et al., 2012, *ApJ*, 746, 69.
- Gerin M., Neufeld D. A., Goicoechea J. R., 2016, *ARA&A*, 54, 181.
- Girichidis P., Konstantin L., Whitworth A. P., Klessen R. S., 2014, *ApJ*, 781, 91.
- Girichidis P., Walch S., Naab T., Gatto A., Wunsch R., Glover S. C. O., Klessen R. S., et al., 2016a, *MNRAS*, 456, 3432.
- Girichidis P., Naab T., Walch S., Hanzs M., Mac Low M.-M., Ostriker J. P., Gatto A., et al., 2016b, *ApJL*, 816, L19.
- Giveon U., Sternberg A., Lutz D., Feuchtgruber H., Pauldrach A. W. A., 2002, *ApJ*, 566, 880.
- Glover S. C. O., Federrath C., Mac Low M.-M., Klessen R. S., 2010, *MNRAS*, 404, 2.
- Glover S. C. O., Clark P. C., 2012, *MNRAS*, 421, 116.
- Godard B., Falgarone E., Pineau des Forêts G., 2014, *A&A*, 570, A27
- Goicoechea J. R., Le Bourlot J., 2007, *A&A*, 467, 1
- Goodman A. A., Pineda J. E., Schnee S. L., 2009, *ApJ*, 692, 91.
- Gong M., Ostriker E. C., Wolfire M. G., 2017, *ApJ*, 843, 38.
- Gong M., Ostriker E. C., Kim C.-G., 2018, *ApJ*, 858, 16.
- Gong M., Ostriker E. C., Kim C.-G., Kim J.-G., 2020, *ApJ*, 903, 142.
- Górski K. M., Hivon E., Banday A. J., Wandelt B. D., Hansen F. K., Reinecke M., Bartelmann M., 2005, *ApJ*, 622, 759.
- Grassi T., Bovino S., Schleicher D. R. G., Prieto J., Seifried D., Simoncini E., Gianturco F. A., 2014, *MNRAS*, 439, 2386.
- Gredel R., van Dishoeck E. F., Black J. H., 1993, *A&A*, 269, 477
- Hailey-Dunsheath S., Nikola T., Stacey G. J., Oberst T. E., Parshley S. C., Benford D. J., Staguhn J. G., et al., 2010, *ApJL*, 714, L162.
- Harrington K. C., Weiss A., Yun M. S., Magnelli B., Sharon C. E., Leung T. K. D., Vishwas A., et al., 2021, *ApJ*, 908, 95.
- Haworth T. J., Glover S. C. O., Koepfer C. M., Bisbas T. G., Dale J. E., 2018, *NewAR*, 82, 1.
- Helder E. A., Broos P. S., Dewey D., Dwek E., McCray R., Park S., Racusin J. L., et al., 2013, *ApJ*, 764, 11.
- Henríquez-Brocal K., Herrera-Camus R., Tacconi L., Genzel R., Bolatto A., Bovino S., Demarco R., et al., 2022, *A&A*, 657, L15.
- Herrera-Camus R., Fisher D. B., Bolatto A. D., Leroy A. K., Walter F., Gordon K. D., Roman-Duval J., et al., 2012, *ApJ*, 752, 112.
- Herrera-Camus R., Bolatto A. D., Wolfire M. G., Smith J. D., Croxall K. V., Kennicutt R. C., Calzetti D., et al., 2015, *ApJ*, 800, 1.
- Herrera-Camus R., Sturm E., Graciá-Carpio J., Lutz D., Contursi A., Veilleux S., Fischer J., et al., 2018, *ApJ*, 861, 94.
- Hodge J. A., da Cunha E., 2020, *RSOS*, 7, 200556.
- Holdship J., Viti S., Martín S., Harada N., Mangum J., Sakamoto K., Muller S., et al., 2021, *A&A*, 654, A55.

- Holdship J., Viti S., 2022, *A&A*, 658, A103.
- Hollenbach D. J., Tielens A. G. G. M., 1999, *RvMP*, 71, 173.
- Hollenbach D., Kaufman M. J., Neufeld D., Wolfire M., Goicoechea J. R., 2012, *ApJ*, 754, 105.
- Hopkins P. F., Wetzel A., Kereš D., Faucher-Giguère C.-A., Quataert E., Boylan-Kolchin M., Murray N., et al., 2018, *MNRAS*, 480, 800.
- Hu C.-Y., Naab T., Walch S., Glover S. C. O., Clark P. C., 2016, *MNRAS*, 458, 3528.
- Hu C.-Y., Naab T., Glover S. C. O., Walch S., Clark P. C., 2017, *MNRAS*, 471, 2151.
- Hu C.-Y., Sternberg A., van Dishoeck E. F., 2021, *ApJ*, 920, 44.
- Hughes A., Meidt S. E., Schinnerer E., Colombo D., Pety J., Leroy A. K., Dobbs C. L., et al., 2013, *ApJ*, 779, 44.
- Hughes D. H., Serjeant S., Dunlop J., Rowan-Robinson M., Blain A., Mann R. G., Ivison R., et al., 1998, *Natur*, 394, 241.
- Indriolo N., Neufeld D. A., Gerin M., Schilke P., Benz A. O., Winkel B., Menten K. M., et al., 2015, *ApJ*, 800, 40.
- James T. A., Viti S., Holdship J., Jiménez-Serra I., 2020, *A&A*, 634, A17.
- Jenkins E. B., Tripp T. M., 2011, *ApJ*, 734, 65.
- Kainulainen J., Beuther H., Henning T., Plume R., 2009, *A&A*, 508, L35.
- Kennicutt R. C., Evans N. J., 2012, *ARA&A*, 50, 531.
- Kim C.-G., Ostriker E. C., 2017, *ApJ*, 846, 133.
- Klessen R. S., Heitsch F., Mac Low M.-M., 2000, *ApJ*, 535, 887.
- Knudsen K. K., Walter F., Weiss A., Bolatto A., Riechers D. A., Menten K., 2007, *ApJ*, 666, 156.
- Krieger N., Bolatto A. D., Leroy A. K., Levy R. C., Mills E. A. C., Meier D. S., Ott J., et al., 2020, *ApJ*, 897, 176.
- Kritsuk A. G., Norman M. L., Wagner R., 2011, *ApJL*, 727, L20.
- Krumholz M. R., McKee C. F., Bland-Hawthorn J., 2019, *ARA&A*, 57, 227.
- Le Bourlot J., Pineau des Forets G., Roueff E., Schilke P., 1993, *ApJL*, 416, L87.
- Le Petit F., Nehmé C., Le Bourlot J., Roueff E., 2006, *ApJS*, 164, 506.
- Leroy A. K., Bolatto A., Gordon K., Sandstrom K., Gratier P., Rosolowsky E., Engelbracht C. W., et al., 2011, *ApJ*, 737, 12.
- Leroy A. K., Hughes A., Schrubba A., Rosolowsky E., Blanc G. A., Bolatto A. D., Colombo D., et al., 2016, *ApJ*, 831, 16.
- Li Q., Tan J. C., Christie D., Bisbas T. G., Wu B., 2018, *PASJ*, 70, S56.
- Li D., Tang N., Nguyen H., Dawson J. R., Heiles C., Xu D., Pan Z., et al., 2018, *ApJS*, 235, 1.
- Li J., Wang R., Riechers D., Walter F., Decarli R., Venamans B. P., Neri R., et al., 2020, *ApJ*, 889, 162.
- Lo N., Cunningham M. R., Jones P. A., Bronfman L., Cortes P. C., Simon R., Lowe V., et al., 2014, *ApJL*, 797, L17.
- Lupi A., Bovino S., 2020, *MNRAS*, 492, 2818.
- Ma Y., Wang H., Zhang M., Wang C., Zhang S., Liu Y., Li C., et al., 2022, *arXiv*, arXiv:2206.03963
- Mackey J., Walch S., Seifried D., Glover S. C. O., Wunsch R., Aharonian F., 2019, *MNRAS*, 486, 1094.
- Madau P., Dickinson M., 2014, *ARA&A*, 52, 415.
- Madden S. C., Cormier D., Hony S., Lebouteiller V., Abel N., Galametz M., De Looze I., et al., 2020, *A&A*, 643, A141.
- Maloney P. R., Hollenbach D. J., Tielens A. G. G. M., 1996, *ApJ*, 466, 561.
- Mashian N., Sturm E., Sternberg A., Janssen A., Hailey-Dunsheath S., Fischer J., Contursi A., et al., 2015, *ApJ*, 802, 81.
- McElroy D., Walsh C., Markwick A. J., Cordiner M. A., Smith K., Millar T. J., 2013, *A&A*, 550, A36.
- Meijerink R., Spaans M., 2005, *A&A*, 436, 397.
- Meijerink R., Spaans M., Israel F. P., 2007, *A&A*, 461, 793.
- Meijerink R., Spaans M., Loenen A. F., van der Werf P. P., 2011, *A&A*, 525, A119.
- Meijerink R., Kristensen L. E., Weiß A., van der Werf P. P., Walter F., Spaans M., Loenen A. F., et al., 2013, *ApJL*, 762, L16.
- Morlino G., Caprioli D., 2012, *AIPC*, 1505, 241.
- Narayanan D., Krumholz M. R., 2014, *MNRAS*, 442, 1411.
- Nelson R. P., Langer W. D., 1997, *ApJ*, 482, 796.
- Nelson R. P., Langer W. D., 1999, *ApJ*, 524, 923.
- Neufeld D. A., Wolfire M. G., 2017, *ApJ*, 845, 163.
- Offner S. S. R., Bisbas T. G., Viti S., Bell T. A., 2013, *ApJ*, 770, 49.
- Offner S. S. R., Bisbas T. G., Bell T. A., Viti S., 2014, *MNRAS*, 440, L81.
- Olivier G. M., Lopez L. A., Rosen A. L., Nayak O., Reiter M., Krumholz M. R., Bolatto A. D., 2021, *ApJ*, 908, 68.
- Olsen K. P., Greve T. R., Narayanan D., Thompson R., Toft S., Brinch C., 2015, *ApJ*, 814, 76.
- Olsen K. P., Burkhart B., Mac Low M.-M., Treß R. G., Greve T. R., Vizgan D., Motka J., et al., 2021, *ApJ*, 922, 88.
- Padovani M., Galli D., Glassgold A. E., 2009, *A&A*, 501, 619.
- Padovani M., Ivlev A. V., Galli D., Caselli P., 2018, *A&A*, 614, A111.
- Papadopoulos P. P., Thi W.-F., Viti S., 2004, *MNRAS*, 351, 147.
- Papadopoulos P. P., 2010, *ApJ*, 720, 226.
- Papadopoulos P. P., van der Werf P., Isaak K., Xilouris E. M., 2010b, *ApJ*, 715, 775.
- Papadopoulos P. P., van der Werf P. P., Xilouris E. M., Isaak K. G., Gao Y., Mühle S., 2012, *MNRAS*, 426, 2601.
- Papadopoulos P. P., Zhang Z.-Y., Xilouris E. M., Weiss A., van der Werf P., Israel F. P., Greve T. R., et al., 2014, *ApJ*, 788, 153.
- Papadopoulos P., Dunne L., Maddox S., 2022, *MNRAS*, 510, 725.
- Pensabene A., Decarli R., Bañados E., Venemans B., Walter F., Bertoldi F., Fan X., et al., 2021, *A&A*, 652, A66.
- Ploetckinger S., Schaye J., 2020, *MNRAS*, 497, 4857.
- Rachford B. L., Snow T. P., Tumlinson J., Shull J. M., Blair W. P., Ferlet R., Friedman S. D., et al., 2002, *ApJ*, 577, 221.
- Rachford B. L., Snow T. P., Destree J. D., Ross T. L., Ferlet R., Friedman S. D., Gry C., et al., 2009, *ApJS*, 180, 125.
- Rangwala N., Maloney P. R., Glenn J., Wilson C. D., Kamenetzky J., Schirm M. R. P., Spinoglio L., et al., 2014, *ApJ*, 788, 147.
- Richings A. J., Schaye J., 2016, *MNRAS*, 458, 270.
- Riechers D. A., Cooray A., Pérez-Fournon I., Neri R., 2021, *ApJ*, 913, 141.
- Roueff E., Le Bourlot J., 2020, *A&A*, 643, A121
- Röllig M., Abel N. P., Bell T., Bensch F., Black J., Ferland G. J., Jonkheid B., et al., 2007, *A&A*, 467, 187.
- Röllig M., Szczerba R., Ossenkopf V., Glück C., 2013, *A&A*, 549, A85.
- Röllig M., Ossenkopf-Okada V., 2022, *A&A*, 664, A67.
- Rosen A. L., Offner S. S. R., Sadavoy S. I., Bhandare A., Vázquez-Semadeni E., Ginsburg A., 2020, *SSRv*, 216, 62.
- Rosenberg M. J. F., van der Werf P. P., Aalto S., Armus L., Charmandaris V., Díaz-Santos T., Evans A. S., et al., 2015, *ApJ*, 801, 72.
- Rybak M., Hodge J. A., Vegetti S., van der Werf P., Andreani P., Graziani L., McKean J. P., 2020, *MNRAS*, 494, 5542.
- Sawada T., Koda J., Hasegawa T., 2018, *ApJ*, 867, 166.
- Stacey G. J., Geis N., Genzel R., Lugten J. B., Poglitsch A., Sternberg A., Townes C. H., 1991, *ApJ*, 373, 423.
- Stacey G. J., Hailey-Dunsheath S., Ferkinhoff C., Nikola T., Parshley S. C., Benford D. J., Staguhn J. G., et al., 2010, *ApJ*, 724, 957.
- Safraneck-Shrader C., Krumholz M. R., Kim C.-G., Ostriker E. C., Klein R. I., Li S., McKee C. F., et al., 2017, *MNRAS*, 465, 885.
- Seifried D., Walch S., Girichidis P., Naab T., Wunsch R., Klessen R. S., Glover S. C. O., et al., 2017, *MNRAS*, 472, 4797.
- Seifried D., Haid S., Walch S., Borchert E. M. A., Bisbas T. G., 2020a, *MNRAS*, 492, 1465.
- Seifried D., Walch S., Weis M., Reissl S., Soler J. D., Klessen R. S., Joshi P. R., 2020b, *MNRAS*, 497, 4196.
- Schlickeiser R., Caglar M., Lazarian A., 2016, *ApJ*, 824, 89.
- Schneider N., Simon R., Kramer C., Kraemer K., Stutzki J., Mookerjee B., 2003, *A&A*, 406, 915.
- Schneider N., Bontemps S., Motte F., Ossenkopf V., Klessen R. S., Simon R., Fechtenbaum S., et al., 2016, *A&A*, 587, A74.
- Schruba A., Leroy A. K., Kruijssen J. M. D., Bigiel F., Bolatto A. D., de Blok W. J. G., Tacconi L., et al., 2017, *ApJ*, 835, 278.
- Sheffer Y., Rogers M., Federman S. R., Abel N. P., Gredel R., Lambert D. L., Shaw G., 2008, *ApJ*, 687, 1075.
- Shi Y., Wang J., Zhang Z.-Y., Gao Y., Armus L., Helou G., Gu Q., et al., 2015, *ApJL*, 804, L11.
- Shi Y., Wang J., Zhang Z.-Y., Gao Y., Hao C.-N., Xia X.-Y., Gu Q., 2016, *NatCo*, 7, 13789.
- Shimajiri Y., André P., Braine J., Könyves V., Schneider N., Bontemps S., Ladjelate B., et al., 2017, *A&A*, 604, A74.

Smail I., Ivison R. J., Blain A. W., 1997, *ApJ*, 490, L5.
 Smith R. J., Treß R. G., Sormani M. C., Glover S. C. O., Klessen R. S., Clark P. C., Izquierdo A. F., et al., 2020, *MNRAS*, 492, 1594.
 Sobolev V. V., 1960, *mes..book*.
 Solimano M., González-López J., Barrientos L. F., Aravena M., López S., Tejos N., Sharon K., et al., 2021, *A&A*, 655, A42.
 Spilker A., Kainulainen J., Orkisz J., 2021, *A&A*, 653, A63.
 Stacey G. J., Geis N., Genzel R., Lugten J. B., Poglitsch A., Sternberg A., Townes C. H., 1991, *ApJ*, 373, 423.
 Stacey G. J., Hailey-Dunsheath S., Ferkinhoff C., Nikola T., Parshley S. C., Benford D. J., Staguhn J. G., et al., 2010, *ApJ*, 724, 957.
 Störzer H., Stutzki J., Sternberg A., 1996, *A&A*, 310, 592.
 Stutzki J., Graf U. U., Haas S., Honingh C. E., Hottgenroth D., Jacobs K., Schieder R., et al., 1997, *ApJL*, 477, L33.
 Sun J., Du F., 2022, *arXiv*, arXiv:2204.13928.
 Tacconi L. J., Genzel R., Sternberg A., 2020, *ARA&A*, 58, 157.
 Tang N., Li D., Yue N., Zuo P., Liu T., Luo G., Chen L., et al., 2021, *ApJS*, 252, 1.
 Tielens A. G. G. M., Hollenbach D., 1985, *ApJ*, 291, 722.
 Valentino F., Magdis G. E., Daddi E., Liu D., Aravena M., Bournaud F., Cortzen I., et al., 2020, *ApJ*, 890, 24.
 Vallini L., Pallottini A., Ferrara A., Gallerani S., Sobacchi E., Behrens C., 2018, *MNRAS*, 473, 271.
 Vallini L., Tielens A. G. G. M., Pallottini A., Gallerani S., Gruppioni C., Carniani S., Pozzi F., et al., 2019, *MNRAS*, 490, 4502.
 van Dishoeck E. F., 1992, *IAUS*, 150, 143.
 van Dishoeck E. F., Jonkheid B., van Hemert M. C., 2006, *FaDi*, 133, 231.
 van der Tak F. F. S., Black J. H., Schöier F. L., Jansen D. J., van Dishoeck E. F., 2007, *A&A*, 468, 627.
 van Dishoeck E. F., Dalgarno A., 1984, *ApJ*, 277, 576.
 Van Loo S., Butler M. J., Tan J. C., 2013, *ApJ*, 764, 36.
 Vaupré S., Hily-Blant P., Ceccarelli C., Dubus G., Gabici S., Montmerle T., 2014, *A&A*, 568, A50.
 Velchev T. V., Girichidis P., Donkov S., Schneider N., Stanchev O., Marinkova L., Seifried D., et al., 2019, *MNRAS*, 489, 788.
 Venemans B. P., Walter F., Decarli R., Bañados E., Hodge J., Hewett P., McMahon R. G., et al., 2017, *ApJ*, 837, 146.
 Visser R., van Dishoeck E. F., Black J. H., 2009, *A&A*, 503, 323.
 Viti S., Roueff E., Hartquist T. W., Pineau des Forêts G., Williams D. A., 2001, *A&A*, 370, 557.
 Vizgan D., Greve T. R., Olsen K. P., Zanella A., Narayanan D., Davè R., Magdis G. E., et al., 2022, *arXiv*, arXiv:2203.05316.
 Walch S., Girichidis P., Naab T., Gatto A., Glover S. C. O., Wünsch R., Klessen R. S., et al., 2015, *MNRAS*, 454, 238.
 Weingartner J. C., Draine B. T., 2001, *ApJ*, 548, 296.
 Weiß A., Henkel C., Downes D., Walter F., 2003, *A&A*, 409, L41.
 Wolfire M. G., McKee C. F., Hollenbach D., Tielens A. G. G. M., 2003, *ApJ*, 587, 278.
 Wolfire M. G., Vallini L., Chevance M., 2022, *arXiv*, arXiv:2202.05867.
 Wootten A., Snell R., Glassgold A. E., 1979, *ApJ*, 234, 876.
 Wu B., Tan J. C., Nakamura F., Van Loo S., Christie D., Collins D., 2017, *ApJ*, 835, 137.
 Xie T., Allen M., Langer W. D., 1995, *ApJ*, 440, 674.
 Young L. M., Meier D. S., Bureau M., Crocker A., Davis T. A., Topal S., 2021, *ApJ*, 909, 98.
 Zanella A., Daddi E., Magdis G., Diaz Santos T., Cormier D., Liu D., Cibinel A., et al., 2018, *MNRAS*, 481, 1976.
 Zhang Z.-Y., Gao Y., Henkel C., Zhao Y., Wang J., Menten K. M., Güsten R., 2014, *ApJL*, 784, L31.
 Zhou P., Zhang G.-Y., Zhou X., Arias M., Koo B.-C., Vink J., Zhang Z.-Y., et al., 2022, *arXiv*, arXiv:2203.13111.

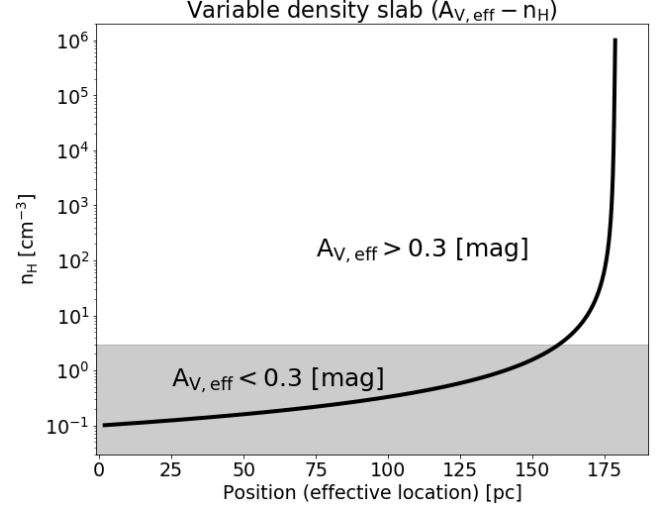


Figure A1. Density profile of the variable density slab resulting from the $A_{V,\text{eff}} - n_{\text{H}}$ relation. The position (x -axis) describes the effective location of each n_{H} in the three-dimensional space and does not represent the size of the cloud. The shadowed region has $A_{V,\text{eff}} < 0.3$ mag and it is atomic for average (Milky-Way) ISM environmental conditions.

APPENDIX A: CONSTRUCTION OF THE VARIABLE DENSITY SLAB

To construct the variable density distribution described in §3.3, we consider a minimum density of $n_{\text{min}} = 0.1 \text{ cm}^{-3}$ and a maximum density of $n_{\text{max}} = 10^6 \text{ cm}^{-3}$. The resolution is taken to be 30 points logarithmic spaced per n dex, thus a total of 210 points. The difference between two consecutive densities corresponds to a Δx displacement satisfying the relation

$$\Delta x(n_i) = \frac{0.05 \left(e^{1.6n_i^{0.12}} - e^{1.6n_{i-1}^{0.12}} \right)}{A_{V,0}n_i}, \quad i \geq 1. \quad (\text{A1})$$

In the above, $A_{V,0} = 6.3 \times 10^{-22} \text{ mag cm}^2$ and n_i is in units of cm^{-3} , thus Δx is in units of cm. The special case of $i = 0$ defines the edge of the cloud in which $\Delta x(n_0) = 0$ for $n_0 \equiv n_{\text{min}}$. Thus, the effective length of the cloud is $L = \sum_i \Delta x(n_i) \approx 178.56 \text{ pc}$. This length represents the effective location of each n_{H} in the three-dimensional space and shall not be considered as the size of the cloud. Figure A1 shows the resultant density profile in black solid line. Note that the slope of the function becomes very steep for $L \gtrsim 175 \text{ pc}$ corresponding to $n_{\text{H}} \gtrsim 10^2 \text{ cm}^{-3}$.

APPENDIX B: COMPARISON WITH RADEX

We perform a benchmarking test to compare our radiative transfer algorithm presented in §3.6 and used in PDF_{CHEM}, with the widely used RADEX algorithm⁹ (van der Tak et al. 2007). For this test we perform a 3D-PDR calculation of an one-dimensional uniform density cloud with $n_{\text{H}} = 10^3 \text{ cm}^{-3}$ H-nucleus number density and a constant temperature of $T_{\text{gas}} = 40 \text{ K}$ everywhere in the cloud (isothermal). The cloud has an $A_V = 10^2 \text{ mag}$ visual extinction. In the PDR calculations, we neglect the FUV radiation field by setting $\chi/\chi_0 = 0$ and

⁹ <https://home.strw.leidenuniv.nl/~moldata/radex.html>

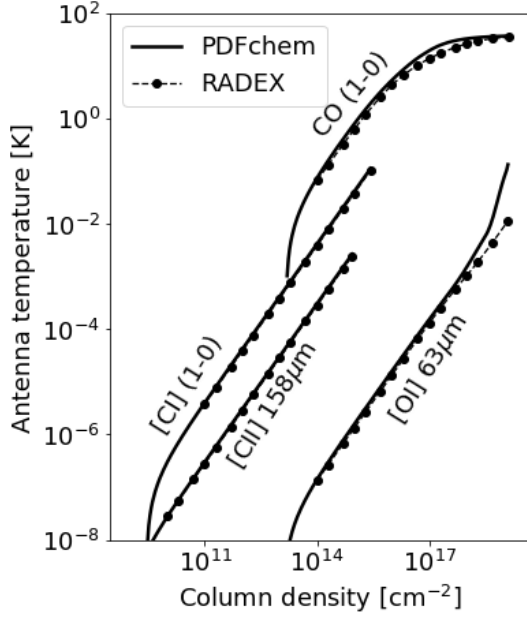


Figure B1. Antenna temperatures versus column density for CO (1-0), [C I] (1-0), [C II] 158 μm , [O I] 63 μm . Solid lines are the results of the §3.6 radiative-transfer scheme used in PDFCHEM, and dashed-thick dotted line are RADEX results. There is an excellent agreement between the two algorithms.

we adopt a microturbulent velocity of $v_{\text{turb}} = 1 \text{ km s}^{-1}$. The latter corresponds to a RADEX linewidth equal to

$$\text{Linewidth} = 2\sqrt{2\ln(2)}\sqrt{\frac{k_B T_{\text{gas}}}{m_{\text{mol}}} + \frac{v_{\text{turb}}^2}{2}} \approx 1.7 \text{ km s}^{-1}, \quad (\text{B1})$$

where k_B is Boltzmann's constant and m_{mol} is the molecular mass of each coolant.

We solve the radiative transfer equation and obtain the radiation temperatures, T_r , of [C II] 158 μm , [C I] (1-0), CO (1-0) and [O I] 63 μm . Figure B1 shows the comparison between the radiative transfer scheme ("PDFCHEM") and RADEX. As can be seen the results obtained by both codes are in broad agreement. Similar behaviour is observed also with the rest of cooling lines we consider.

APPENDIX C: EFFECT OF THE SUPRATHERMAL SWITCH

As described in §3.2, the PDR calculations used for the above results include the switch of CO formation path via CH^+ . It is interesting to explore the effect it has compared to the classical PDR approach (e.g. Röllig et al. 2007) which excludes it. For this, we have re-run the grid of models for $Z = 1 Z_\odot$ and have applied our method to the non star-forming $A_{V,\text{obs}}$ -PDF case. We compare the H_I-to-H₂ transition and explore the pairs of $(\zeta_{\text{CR}}, \chi/\chi_0)$ that make the antenna temperature of CO $J = 1 - 0$ the dominant one amongst all carbon phases.

Figure C1 shows this comparison when the suprathermal switch is enabled ('SUP ON'; black lines and gray region) and disabled ('SUP OFF'; red lines and region). Once the suprathermal switch is disabled, the H_I-to-H₂ is found to occur for higher pairs of χ/χ_0 and ζ_{CR} , which means that the transition occurs at higher depths into the cloud. This is due to the destruction of H₂ by C^+ in addition to photodissociation (see also Appendix A of Paper I). The gray

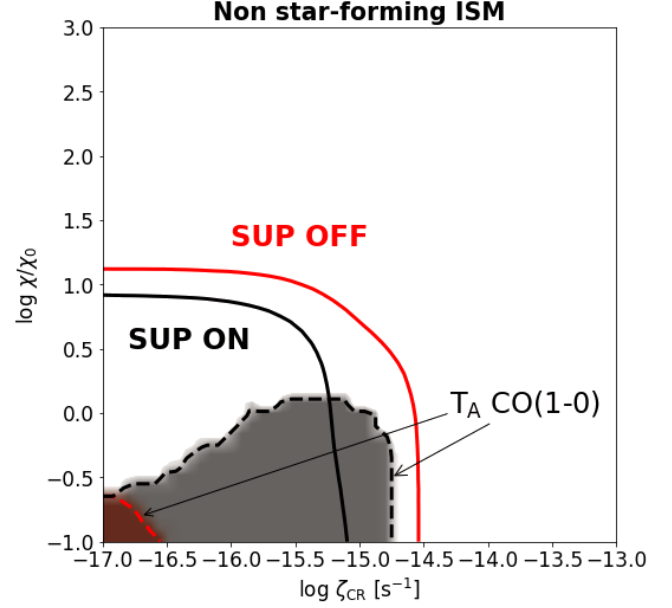


Figure C1. The H_I-to-H₂ transition and the antenna temperature of CO $J = 1 - 0$ at solar metallicity for the non star-forming ISM distribution, when the suprathermal switch is enabled ('SUP ON', black lines) and disabled ('SUP OFF', red lines). The H_I-to-H₂ transition (solid lines) occurs at higher visual extinctions due to the destruction of H₂ by C^+ . The shaded regions indicate when the antenna temperature of CO $J = 1 - 0$ dominates over that of other species in the carbon cycle (gray coloured for 'SUP ON', red coloured for 'SUP OFF').

shadowed region, showing the range in which $T_A(\text{CO } 1-0)$ dominates, is much more extended in the 'ON' case than in the 'OFF' case, the latter marked in red shadow. In particular it is found that $T_A(\text{CO } 1-0)$ dominates in the 'OFF' case only for a very small range of ISM parameters with $\zeta_{\text{CR}} \lesssim 2 \times 10^{-16} \text{ s}^{-1}$ and $\chi/\chi_0 \lesssim 0.3$ as opposed in the 'ON' case where $\zeta_{\text{CR}} \lesssim 2 \times 10^{-15} \text{ s}^{-1}$ and, in general, $\chi/\chi_0 \lesssim 1$.

As a result, the suprathermal formation of CO via CH^+ can affect both the H_I-to-H₂ transition but most importantly it can make an ISM distribution to be bright in CO(1-0) for a much wider range of ISM environmental parameters.

APPENDIX D: OPTICAL DEPTHS FOR THE NON-STAR FORMING DISTRIBUTION

Figure D1 shows optical depth (τ) maps of the [C II] 158 μm , [C I](1-0) and CO(1-0) for all ISM environmental parameters. As with Fig. 8, the red solid line represent the H_I-to-H₂ transition. We also mark with white dotted lines the condition at which $\tau = 0.5$ and with white solid lines the $\tau = 1$ condition. These conditions show when optical depth effects start to be important and when the line has become optically thick, respectively.

As discussed in §5.1.2, for $Z = 0.1 Z_\odot$ the distribution is largely atomic and [C II] 158 μm bright, thus [C I](1-0) and CO(1-0) are expected to be quite faint. Nevertheless, it is found that all aforementioned lines are very optically thin under all combinations of ζ_{CR} and χ/χ_0 (panels a-c). For $Z = 0.5 Z_\odot$, the molecular phase of the distribution is also optically thin in [C II] and [C I](1-0) (panels d-e), but becomes optically thick in the CO(1-0) line as ζ_{CR} approaches $\sim 10^{-16} \text{ s}^{-1}$ (panel f).

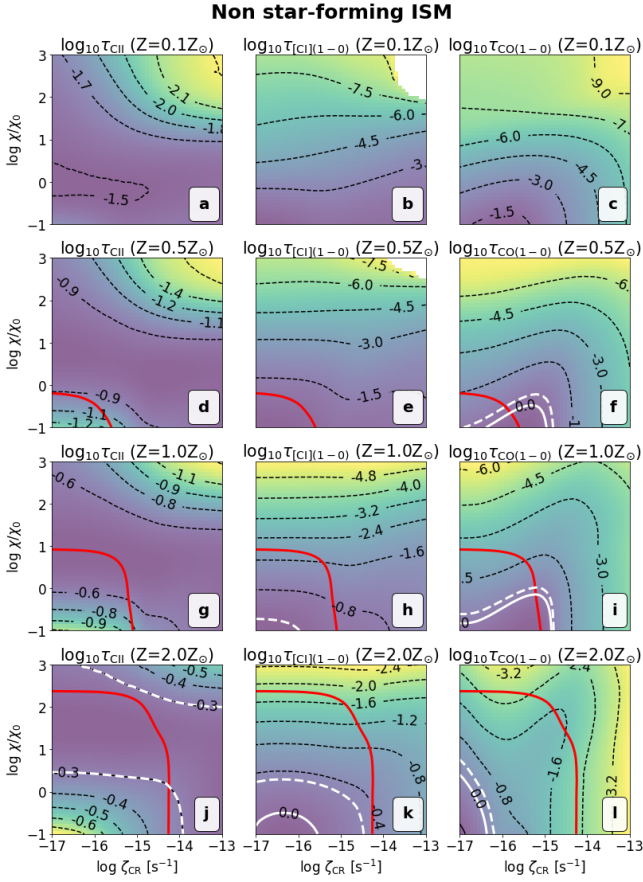


Figure D1. Optical depths of [CII] 158 μ m (left column), [CI](1-0) (middle column) and CO(1-0) (right column) for $Z = 0.1, 0.5, 1.0$ and $2.0Z_{\odot}$ (top-to-bottom), for the non-star-forming distribution. The red solid line marks the H I-to-H₂ transition. The white dashed and the white solid lines correspond to $\tau = 0.5$, i.e. when optical depth effects start to become important, and $\tau = 1$, i.e. when the line has become optically thick, respectively.

For $Z = 1Z_{\odot}$, it is found that both [CII] and [CI](1-0) remain optically thin (panels g-h) with the latter to have $\tau \approx 0.5$ for only a combination of very low ζ_{CR} and χ/χ_0 . On the other hand, CO(1-0) (panel i) becomes optically thick for $\chi/\chi_0 \lesssim 0.5$ when $\zeta_{CR} \lesssim 10^{-16} \text{ s}^{-1}$. Notably, for moderate cosmic-rays ($\zeta_{CR} \sim 7 \times 10^{-16} \text{ s}^{-1}$) it remains optically thick for FUV intensities up to $\chi/\chi_0 \approx 1$.

For $Z = 2Z_{\odot}$, $\tau_{CII} \gtrsim 0.5$ for $\chi/\chi_0 \gtrsim 5$ regardless of the ζ_{CR} parameter for molecular conditions (panel j). We, therefore, find that this line may experience optical depth effects especially at higher FUV intensities. The [CI](1-0) line becomes optically thick, with $\tau_{CI} \sim 1$ for $\chi/\chi_0 < 0.5$ and for $\zeta_{CR} \lesssim 10^{-16} \text{ s}^{-1}$ (panel k). Interestingly, CO(1-0) is optically thick for conditions similar to those for the [CI](1-0) (panel l). Looking at the response of τ_{CO} for $Z = 0.5$ and $1.0Z_{\odot}$ (panels f & i), one would expect to find a distribution that would be much more optically thick in CO(1-0) for $Z = 2.0Z_{\odot}$. However, because higher metallicity implies higher visual extinction, the suprathermal switch plays a minor role here and ceases to be important at lower A_V than in the above cases. Consequently, CO does not form as quickly at low A_V as for $Z \lesssim 1Z_{\odot}$ and given that the non-star-forming ISM is a low column density distribution, reduces the optical depth of CO(1-0). It is further noted that should the $Z = 0.1 - 1Z_{\odot}$ models not include the suprathermal CO formation path, it would result in optically thin CO(1-0).

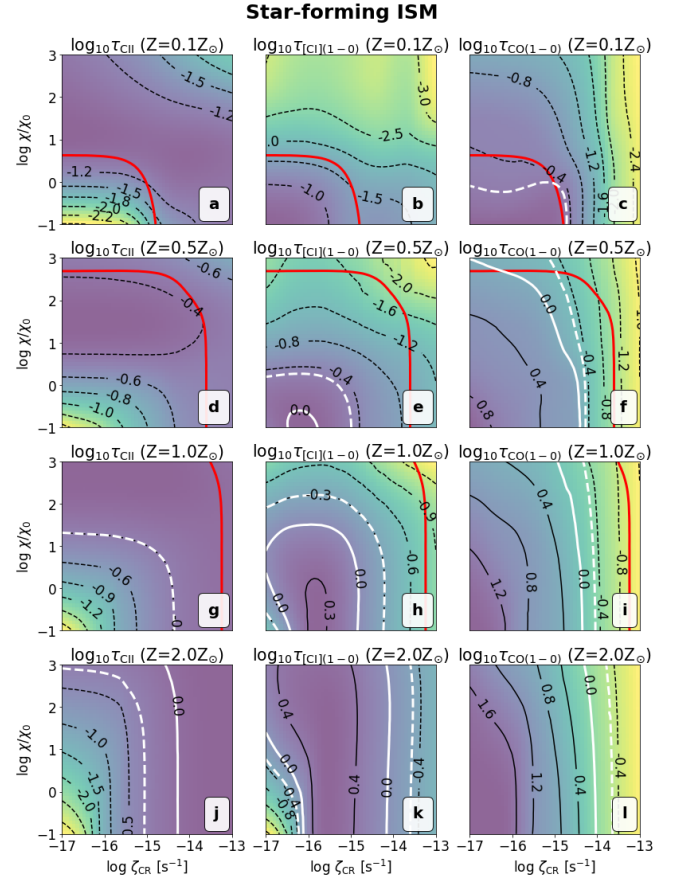


Figure E1. As in Fig. D1 for the star-forming ISM.

APPENDIX E: OPTICAL DEPTHS FOR THE STAR-FORMING DISTRIBUTION

Figure E1 shows the optical depths of the basic carbon cycle emission lines. For $Z = 0.1Z_{\odot}$, both [CII] and [CI](1-0) remain optically thin (panels a,b), while CO(1-0) has $\tau_{CO} \sim 0.5$ for molecular conditions and for $\chi/\chi_0 \lesssim 1$ (panel c). For $Z = 0.5Z_{\odot}$, [CII] remains optically thin (panel d) but [CI](1-0) experiences optical depth effects for low FUV intensities and low ζ_{CR} values (panel e). On the other hand, CO(1-0) (panel f) becomes quickly optically thick for $\zeta_{CR} \lesssim 10^{-15} \text{ s}^{-1}$ and, interestingly, τ_{CO} depends primarily on the value of the cosmic-ray ionization rate.

For $Z = 1Z_{\odot}$, [CII] experiences optical depth effects for $\zeta_{CR} \lesssim 8 \times 10^{-15} \text{ s}^{-1}$ and $\chi/\chi_0 \gtrsim 20$, as well as for $\zeta_{CR} \gtrsim 8 \times 10^{-15} \text{ s}^{-1}$ regardless to the FUV intensity (panel g). For moderate ζ_{CR} and for $\chi/\chi_0 \lesssim 10$, [CI](1-0) becomes optically thick (panel h). As in the $Z = 0.5Z_{\odot}$ case, CO(1-0) becomes optically thick for $\zeta_{CR} \lesssim 8 \times 10^{-15} \text{ s}^{-1}$ (panel i). Finally, for $Z = 2Z_{\odot}$, [CII] is optically thick for $\zeta_{CR} \gtrsim 10^{-14} \text{ s}^{-1}$, and both [CI](1-0) and CO(1-0) (panels k,l) are also very optically thick for almost all combinations of ζ_{CR} -FUV intensities.

As a result, for such an $A_{V,obs}$ -PDF, CO(1-0) is optically thick for almost all conditions explored while [CI](1-0) and [CII] become optically thick for metallicities of $Z \gtrsim 1.0Z_{\odot}$.

APPENDIX F: ABUNDANCES AND LINE RATIOS FOR DIFFERENT METALLICITIES

Figures F1-F3 show the results for the non-star-forming ISM distribution for metallicities of $Z = 0.1, 0.5$ and $2.0 Z_{\odot}$. Figures F4-F6 show the corresponding results for the star-forming ISM distribution.

APPENDIX G: USING A DIFFERENT A_V/N_H CONSTANT

As mentioned in the Introduction, in this work the conversion $A_V = N_H \cdot 6.3 \times 10^{-22}$ mag is used (Röllig et al. 2007) for a more accurate comparison with Paper I and B21. However, the conversion $A_V = N_H \cdot 5.3 \times 10^{-22}$ mag (Bohlin, Savage, & Drake 1978) is frequently used by other groups in PDR studies. Here, the grid of models for $Z = 1 Z_{\odot}$ is repeated using the aforementioned constant, for both the non star-forming and the star-forming ISM distributions. Figure G1 illustrates the results. The $A_V/N_H = 5.3 \times 10^{-22}$ mag cm² constant lowers the range of $\chi/\chi_0 - \zeta_{CR}$ pairs for which the non star-forming distribution remains molecular, whereas it does not affect the H_I-to-H₂ transition in the star-forming distribution. The carbon cycle has no appreciable differences for either ISM distributions, both in terms of abundances and of antenna temperatures. It is, therefore, found that the slightly different A_V/N_H ratio used does not alter the results in the present paper.

This paper has been typeset from a \LaTeX file prepared by the author.

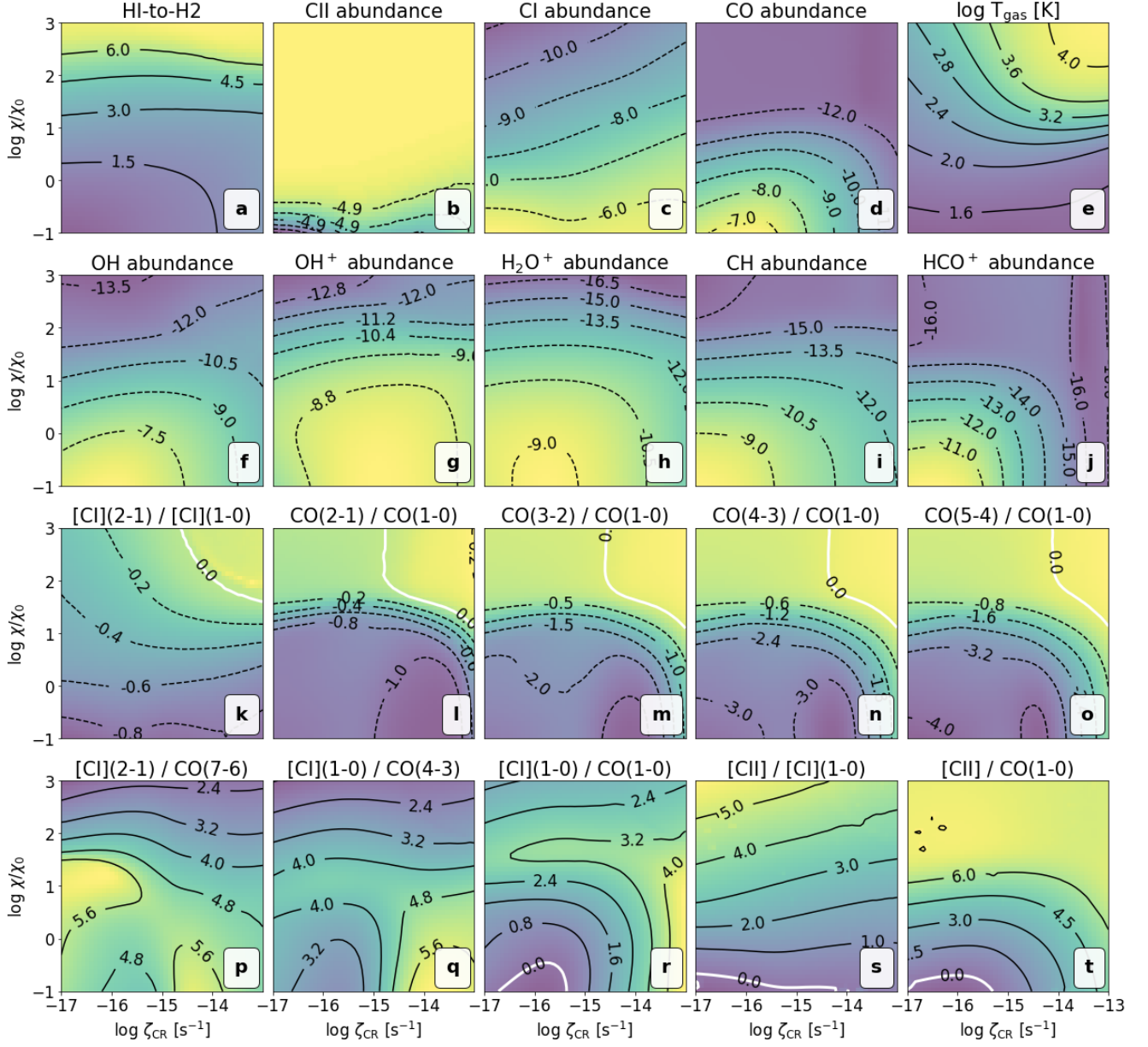
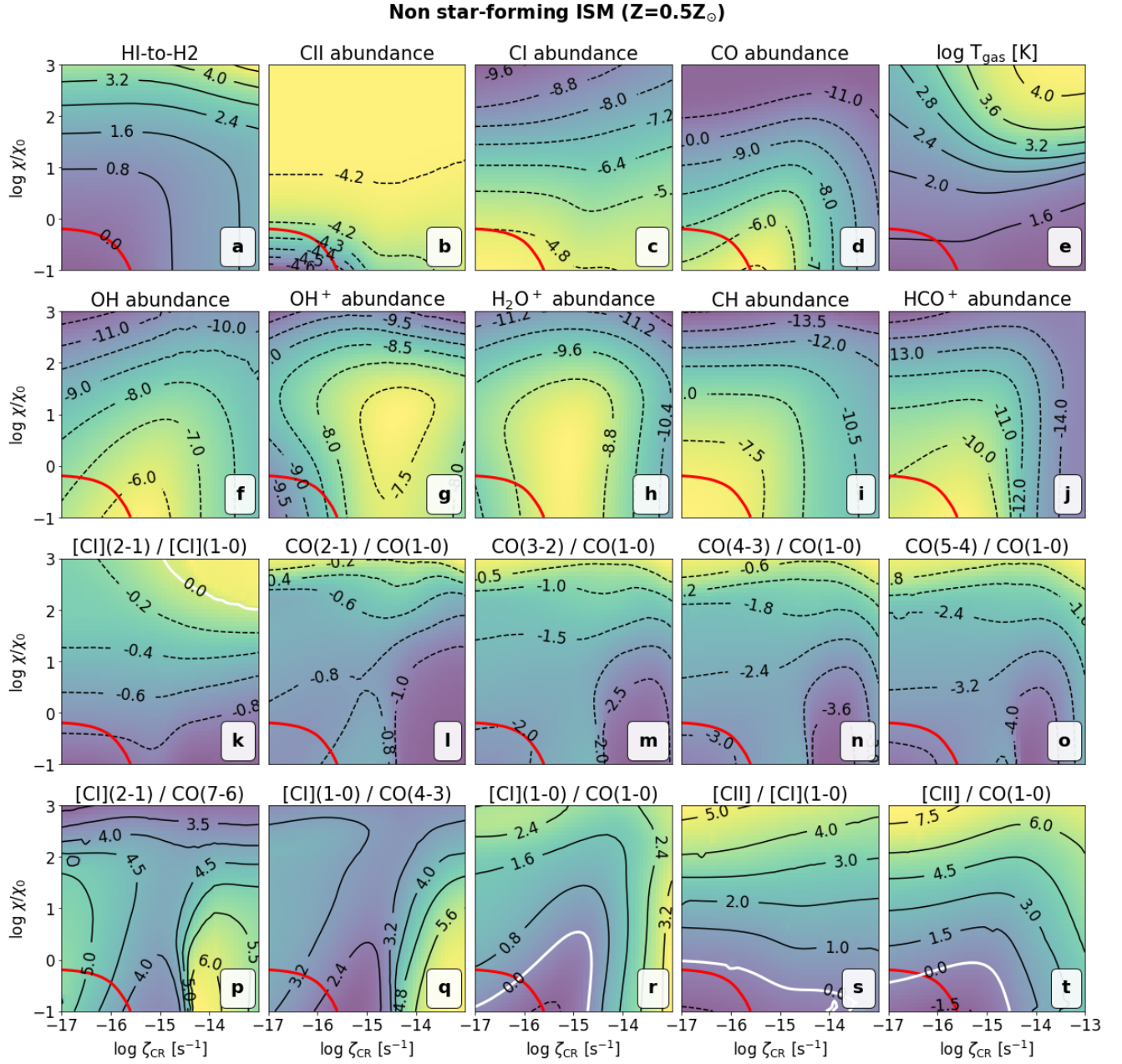
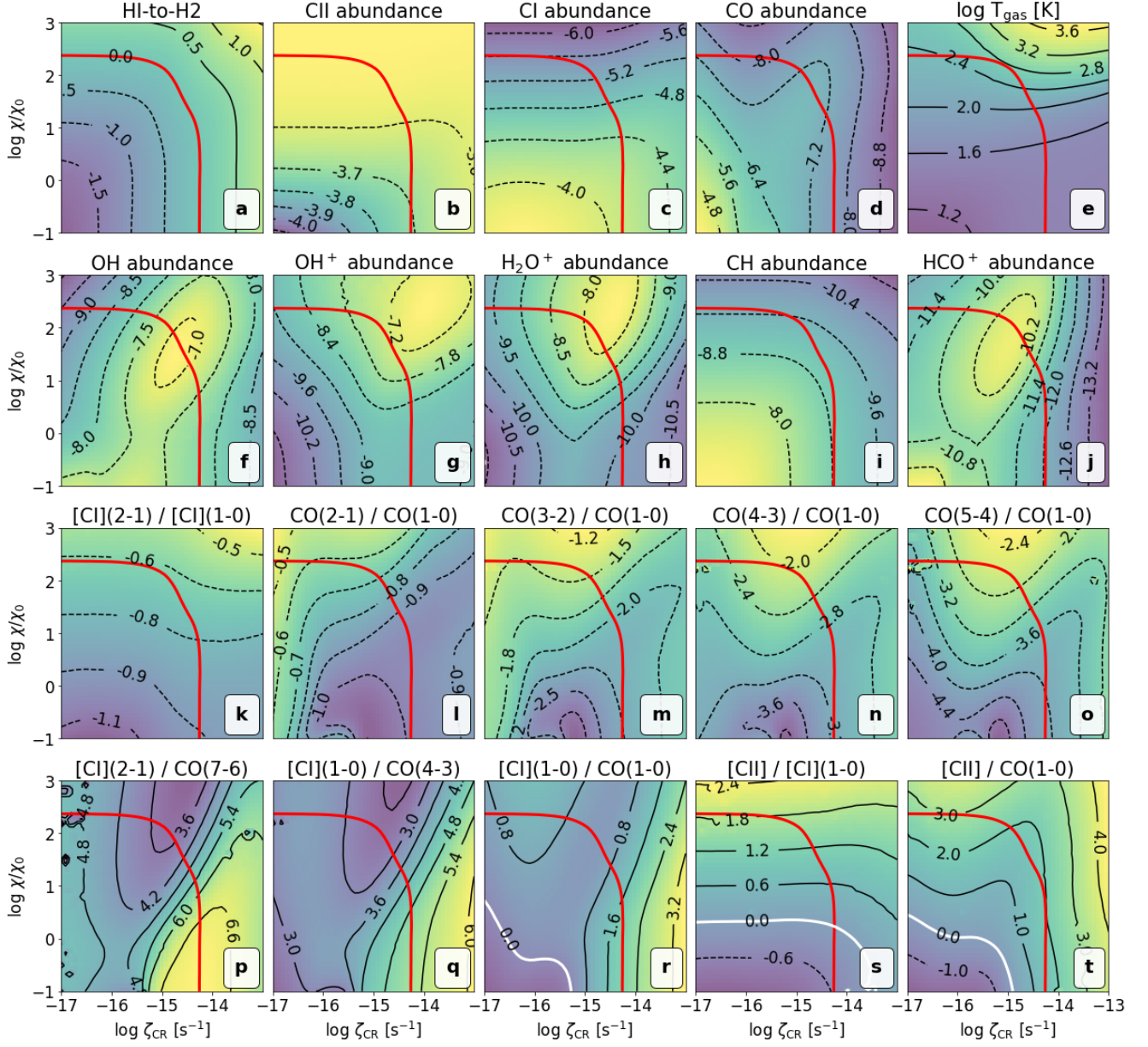
Non star-forming ISM ($Z=0.1Z_{\odot}$)


Figure F1. As Fig.8 for $Z = 0.1 Z_{\odot}$. Note that the medium is atomic in all cases.

**Figure F2.** As Fig.8 for $Z = 0.5Z_{\odot}$.

Non star-forming ISM ($Z=2.0Z_{\odot}$)

 Figure F3. As Fig.8 for $Z = 2.0Z_{\odot}$.

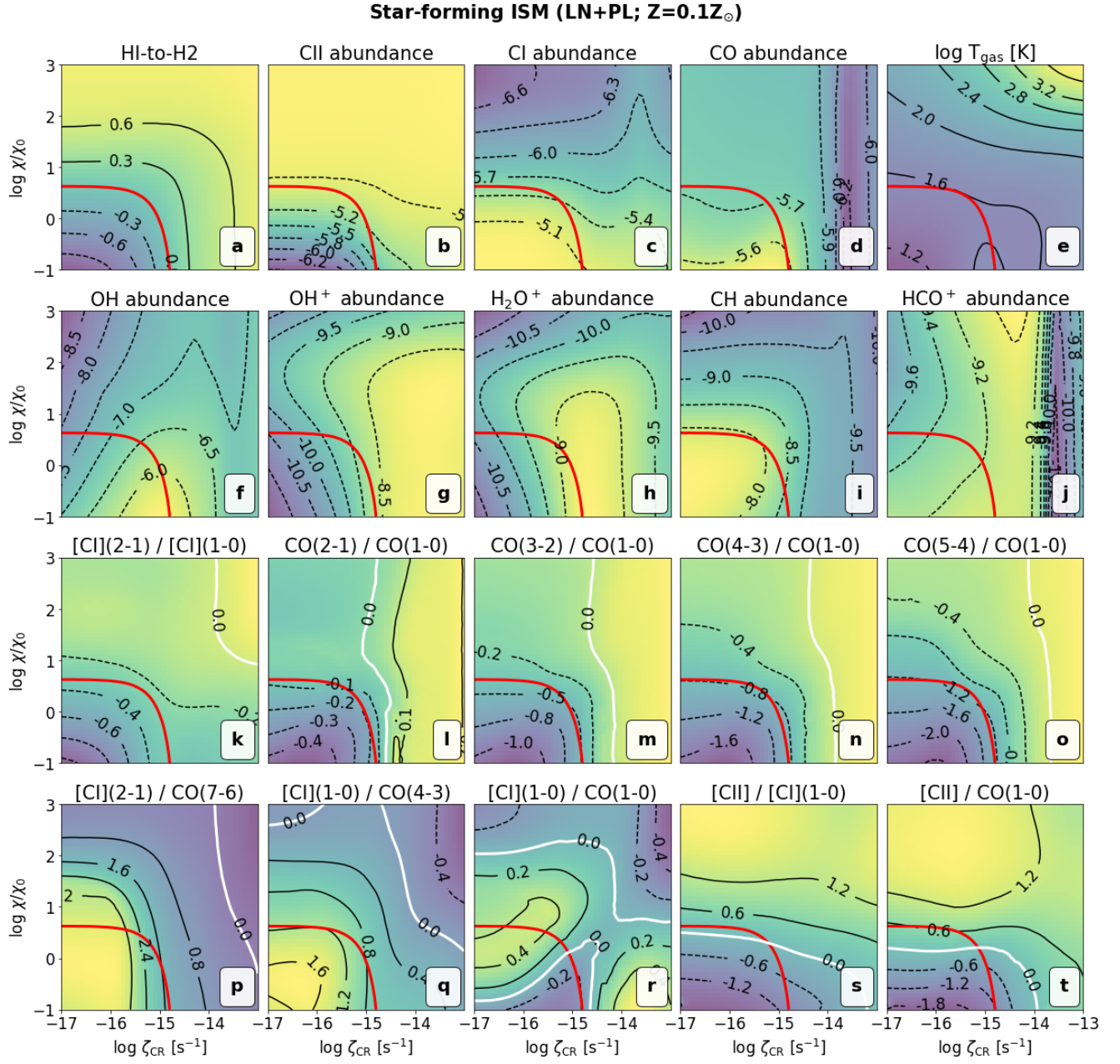
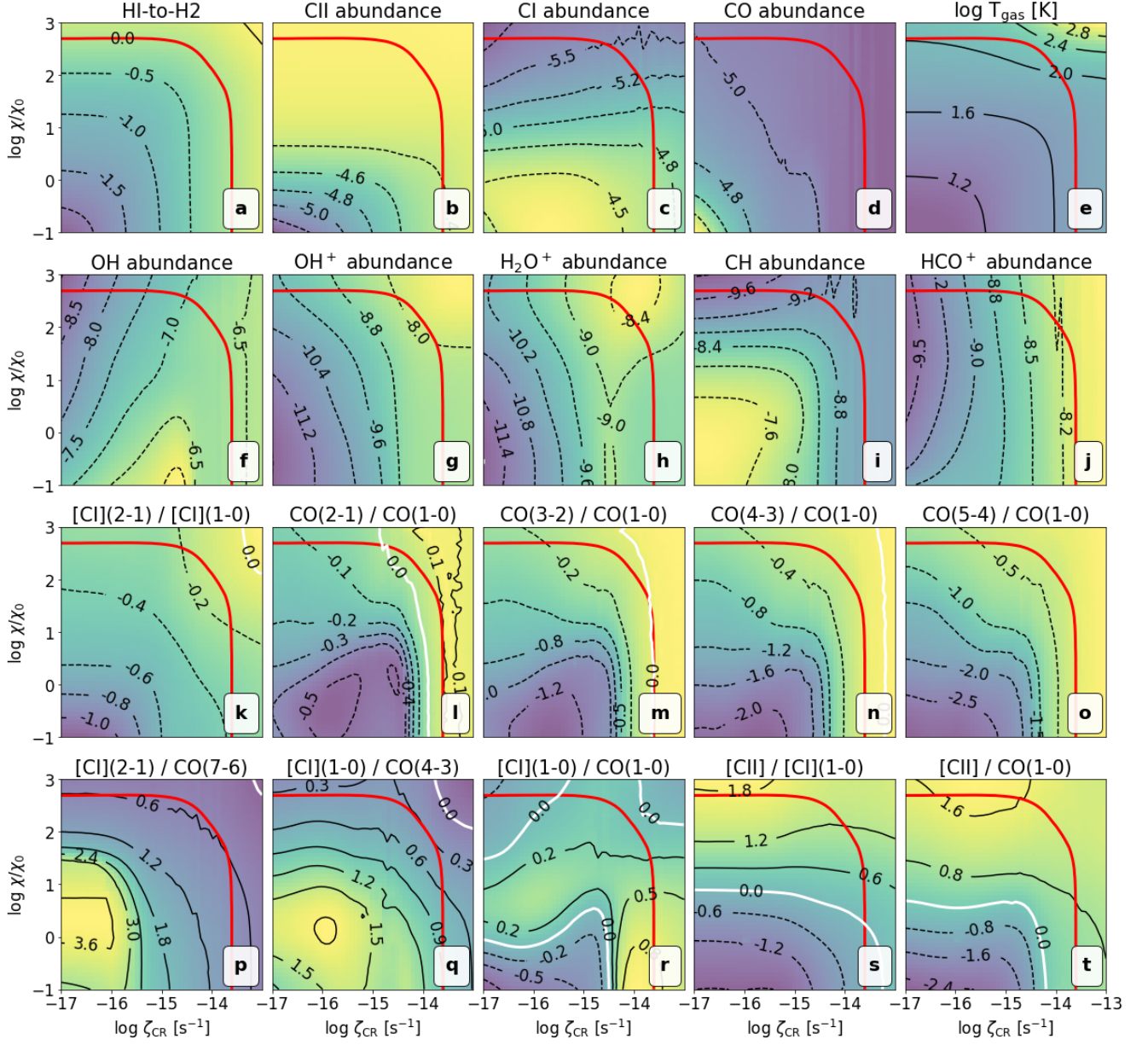


Figure F4. As Fig.10 for $Z = 0.1 Z_{\odot}$.

Star-forming ISM (LN+PL; $Z=0.5Z_{\odot}$)

 Figure F5. As Fig.10 for $Z = 0.5 Z_{\odot}$.

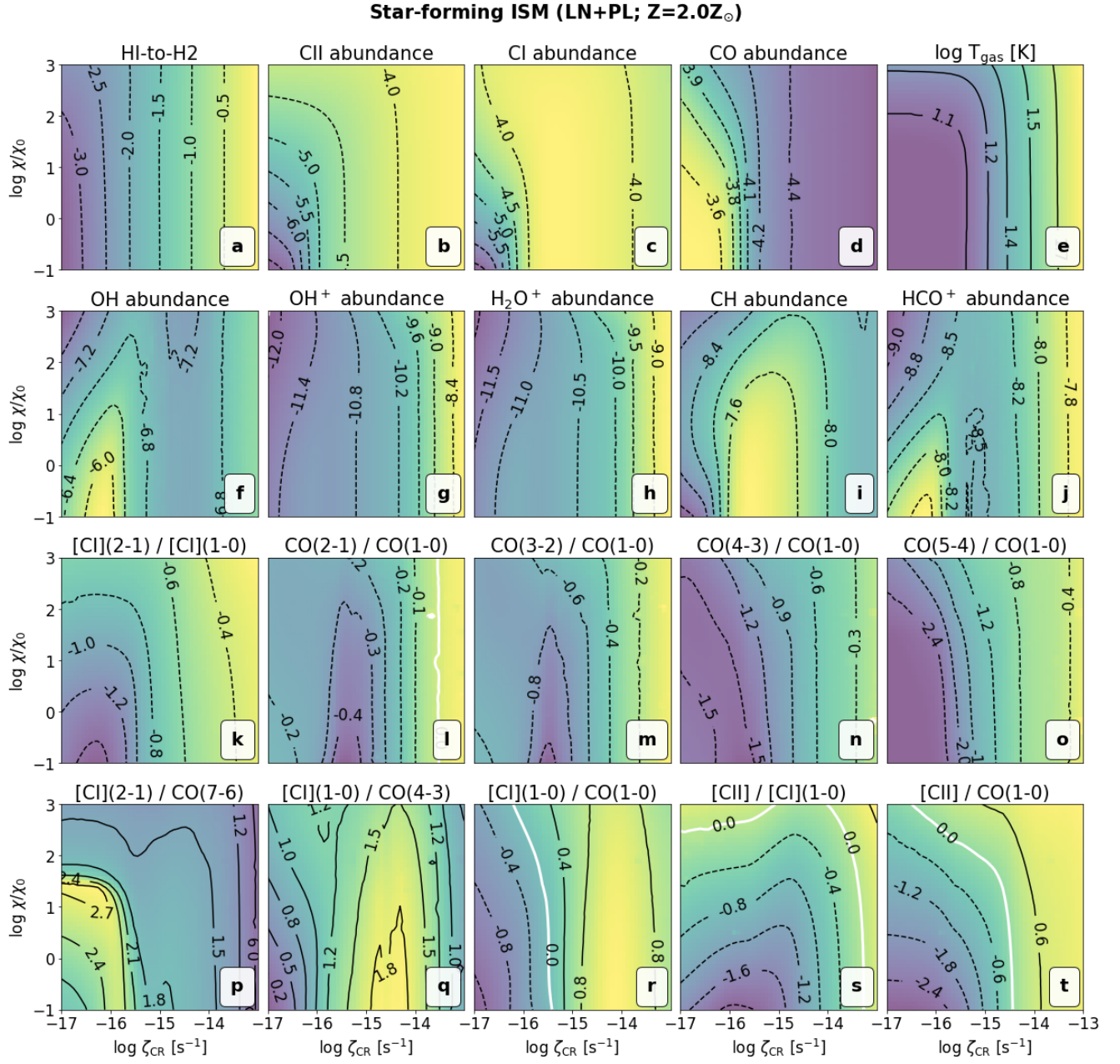


Figure F6. As Fig. 10 for $Z = 2.0Z_{\odot}$. Note that the medium is molecular in all cases.

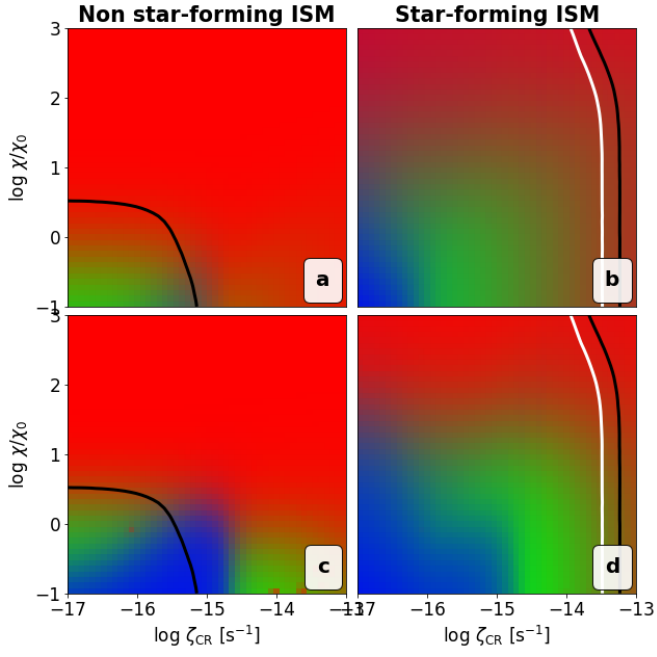


Figure G1. Carbon phases and H_I-to-H₂ transitions as discussed in Figs. 9 and 11 for $A_V/N_H = 5.3 \times 10^{-22} \text{ mag cm}^2$. As can be seen, there are no appreciable differences in the results when adopting the lower A_V/N_H that is frequently used in other similar PDR studies. In panels (b) and (d), the white line corresponds to the LN-only distribution.